A Szilikátipari Tudományos Egyesület lapja

építőanyag

Journal of Silicate Based and Composite Materials

A TARTALOMBÓL:

2014/3

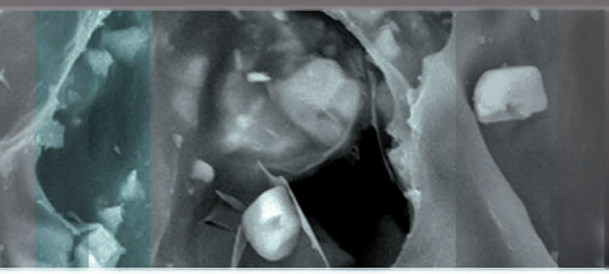

ic-rmm2

2nd INTERNATIONAL CONFERENCE ON RHEOLOGY AND MODELING OF MATERIALS

in Miskolc-Lillafüred, Hungary, 5-10 October, 2015.

Welcome to ic-rmm2

We are pleased to announce the organization of the 2nd **INTERNATIONAL CONFERENCE ON RHEOLOGY AND MODELING OF MATERIALS** to be held near city **Miskolc** in mountain **Bükk** in one of the most beautiful places of **Hungary** in **Hunguest Hotel Palota Lillafüred, October 5-10, 2015.**

The idea to organize in **Hungary** the **2nd International Conference on Rheology and Modeling of Materials** we have received from prospective scientists, physicists, chemists, mathematicians and engineers from **Asia, Europe, North and South America** including China, India, Japan, Korea, Russia, Turkey, Estonia, France, Italy, United Kingdom, Chile, Mexico, USA. As organizers we hope that you will attend on **ic-rmm2** and we are looking forward to welcome you on this international conference in **Miskolc-Lillafüred, Hungary**. Event **ic-rmm2** is sponsored by several universities, scientific journals, societies and organizations around the World.

The objectives

The **aims** of the **2nd International Conference on Rheology and Modeling of Materials** are the fostering of interdisciplinary collaboration and interaction among scientists, researchers, PhD students as well as product and technology developer engineers. The international conference **ic-rmm2** provides a platform among leading international scientists, physicists, chemists, mathematicians, researchers, PhD students and engineers for discussing recent achievements in measurement, modeling and application of rheology in materials technology and materials science of liquids, melts, solids, powders, crystals and amorphous structures.

Among the major fields of interest are the influences of temperature, mechanical stresses, deformation speeds and times on rheological properties, material structures and phase transformation of foams, emulsions, suspensions, liquids, powders, crystals, foods, cosmetics, polymers, plastics, petrochemicals, melted metals, glass and competitive materials like nanomaterials, pharmaceuticals, medical- and biomaterials, ceramics, films and coatings, advanced metal alloys, composites, hetero-modulus, hetero-plastic and hetero-viscous complex material systems, hybrid materials, ... etc.

Multidisciplinary applications of rheology as well as mechanical and rheological modeling in material science and technology encountered in sectors like food, bio- and medical materials, ceramics, glass, thin films, polymers, clays, construction materials, energy, aerospace, automotive and marine industry. Rheology in physics, chemistry, medicine, biosciences, cosmetics, environmental and earth sciences and in engineering and industries are of particular interests.

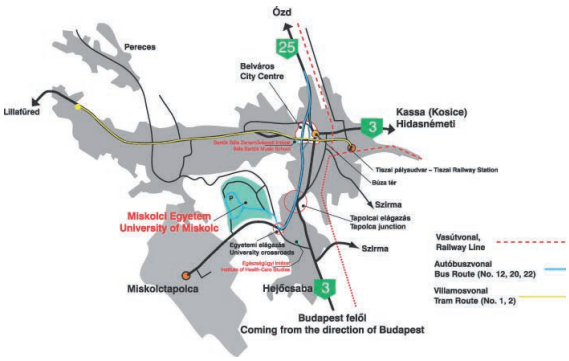

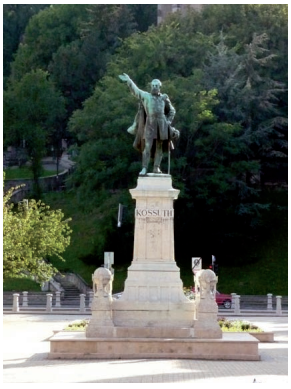

Further information can be obtained from Prof. Dr. László A. Gömze by e-mail **femgomze@uni-miskolc.hu**

építőanyag

Journal of Silicate Based and Composite Materials

2014/3

TARTALOM

CONTENT

A finomkerámia-, üveg-, cement-, mész-, beton-, tégla- és cserép-, kő- és kavics-, tűzállóanyag-, szigetelőanyag-iparágak szakmai lapja
Scientific journal of ceramics, glass, cement, concrete, clay products, stone and gravel, insulating and fireproof materials and composites

A folyóiratot referálja:
Cambridge Scientific Abstracts
ProQuest

A folyóiratban lektorált cikkek jelennek meg.
Kiadja a Szilikátipari Tudományos Egyesület
1034 Budapest, Bécsi út 122–124.
Telefon és fax: +36-1/201-9360
E-mail: epitoanyag@szte.org.hu
Felelős kiadó: ASZTALOS István SZTE elnök
Tördelő szerkesztő: NÉMETH Hajnalka

Címlapfotó/Cover photo by KÓSA Luca Kornélia

Belföldi terjesztés: SZTE
Külföldi terjesztés: Batthyany Kultur-Press Kft.

WWW.EPITOANYAG.ORG.HU

Online ISSN: 2064-4477 ▪ Print ISSN: 0013-970x
INDEX: 2 52 50 ▪ 66 (2014) 57–92

66. évf. 3. szám

Development of AlN ceramic composites for multilayer ceramic devices

Iryna V. BRODNIKOVSKA ▪ Frantsevich Institute for Problems of Materials Science of NASU, Krzhizhanivsky str. 3, 03680, Kyiv, Ukraine
Andriy I. DERIY ▪ Frantsevich Institute for Problems of Materials Science of NASU, Krzhizhanivsky str. 3, 03680, Kyiv, Ukraine
Vitaly Ya. PETROVSKY ▪ Frantsevich Institute for Problems of Materials Science of NASU, Krzhizhanivsky str. 3, 03680, Kyiv, Ukraine

Received: 31. 03. 2014. ▪ Érkezett: 2014. 03. 31. ▪ http://dx.doi.org/10.14382/epitoanyag-jsbcm.2014.12

Abstract
Mechanical and electrical properties of AlN ceramics are dependent of phase composition and sintering temperature. TiO_2 and TiH_2 additives were chosen as the structure and properties modifiers and HfC – as conductive phase. AlN ceramics was considered as dielectric and conductive layers of functionally graded materials. Our investigations showed that AlN-1.5-2%TiO_2 ceramic composites is a prominent dielectric with required properties and in combination with 11–17% HfC it serves as effective ceramic heater.
Broadband dielectric spectroscopy was used for the nondestructive testing of microstructure: dispersion frequency gives information about the effective thickness of a conductive channel; the slope of σ(ω) dependence gives distinction between "lattice" and "carrier" responses corresponding to "intrinsic", which is irreducible, and "extrinsic" processes due to some impurities or injected carriers.
Keywords: aluminum nitride, hot pressing, dielectric response, ceramic substrates, functionally graded materials.

Iryna Brodnikovska
PhD, Department of High-Temperature Dielectric and Resistive Materials, Frantsevich Institute for Problems of Materials Science of National Academy of Sciences of Ukraine. Engineer of electronics (MSc), PhD, Research Associate at Department of High-Temperature Dielectric and Resistive Materials, Frantsevich Institute for Problems of Materials Science of NASU. Main fields of interest: non-destructive monitoring of microstructure, functional ceramics.

Andriy Deriy
Powder metallurgist at Department of High-Temperature Dielectric and Resistive Materials, Frantsevich Institute for Problems of Materials Science of National Academy of Sciences of Ukraine. Engineer of powder metallurgy (MSc), Research Associate at Department of High-Temperature Dielectric and Resistive Materials, Frantsevich Institute for Problems of Materials Science of NASU. Main fields of interest are powder metallurgy, functional ceramics and monitoring of microstructure.

Vitaly Petrovsky
DSci. Department of High-Temperature Dielectric and Resistive Materials, Frantsevich Institute for Problems of Materials Science of National Academy of Sciences of Ukraine. Engineer of electronics (MSc), PhD, DSci. Head of Department of High-Temperature Dielectric and Resistive Materials, Frantsevich Institute for Problems of Materials Science of NASU. Associate Professor at Micro- and Nanoelectronics Department of National Technical University of Ukraine "KPI". Main fields of interest: ceramic matrix composites, insulator-metal composites, microelectronic devices.

1. Introduction

Microminiaturization of electro technical devices leads to the development of the functionally graded materials (multilayer ceramic devices) - monolithic ceramic bodies with conductive and dielectric layers made by appropriate tapes and sintered together in one step [1]. They can serve as Multi-Chip Modules (MCM-C) (especially HTCC) or composite heating systems (Gradient, Ukraine [2], *Fig. 1*, KYOCERA Corporation, Japan [3],). Al_2O_3 [4 - 7] and Si_3N_4 [8, 9] are the most commonly produced materials for high temperature dielectric matrix, as well as AlN [10, 11, 12, 13], which has higher thermal conductivity (320 W/m·K vs. 40 W/m·K for Al_2O_3 and 125 W/m·K for β- Si_3N_4).

To improve mechanical and electrical properties of AlN dielectric substrates large cations doping may be applied [14] (*Fig. 2*). For example, titanium cations may be added in the form of TiO_2, TiH_2, etc. Titanium oxide increases relative density, reduces dielectric permittivity and losses [15]. Under dissociation of TiO_2 O^{2-} ions lead to the grain elongation and formation of plate-like morphology (i.e. the formation of polytypes in AlN). Thus they increase toughness of the material [16]. Titanium hydride also reveals a beneficial effect on mechanical and thermal properties of AlN: as TiH_2 dissociates at 600-800°C [17], H^+ cations toughen the structure due to its refinement and formation of solid solution of hydrogen in aluminium nitride [18]. Ti^{2-} ions may increase thermal conductivity of composites [19]. But the effect of such toughening additives on electrical properties of aluminium nitride ceramics was not observed or observed only fragmentary.

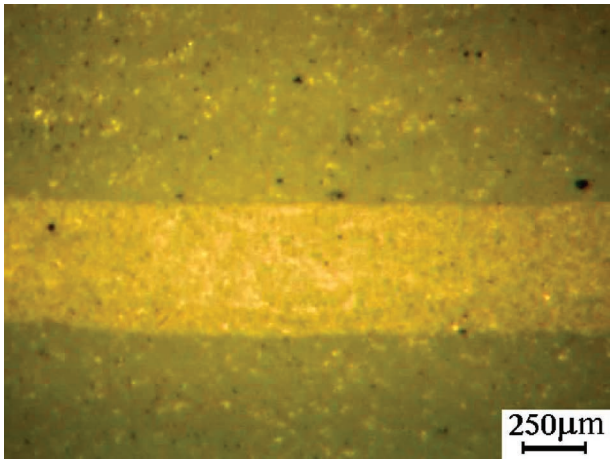

Fig. 1. Microstructure of functionally graded material which consists of dielectric (Si_3N_4-based) (dark) and conductive (Si_3N_4-13.5 vol.% ZrC) (light) layers obtained by one step hot-pressing [1]
1. ábra Egylépcsős melegsajtolással előállított dielektromos (Si_3N_4-bázisú, az ábrán sötétebb tónusú) és vezetőréteget tartalmazó (Si_3N_4-13,5 vol% ZrC, az ábrán világosabb tónusú) funkcionális gradiens anyag mikro szerkezete

For active resistive layer formation different refractory compounds are chosen: TiN [20], $MoSi_2$ [21], TaN [22], Mo [23], Ni [5]. HfC [24] is a promising additive for high temperature operation. If dielectric matrix of the material is an active element it can produce thermal energy up to 10-30% more. Properties of resistive layer under the influence of various technological factors can vary both in a positive and

in a negative way. Commercially viable thermoelectric heaters should possess a set of optimal parameters of resistive layer, such as: the sign and value of the resistance temperature coefficient, resistance reproducibility, maximal surface temperature at minimal surface density of the heat load.

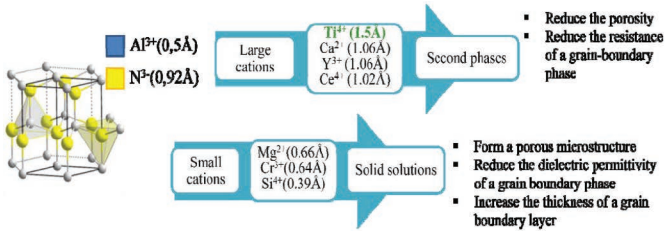

Fig. 2. Effect of dopants on the complex impedance and dielectric properties of aluminium nitride according to [14]
2. ábra A dopoló anyag hatása az alumínium-nitrid komplex impedanciájára és dielektromos tulajdonságaira [14] szerint

The aim of present work is the complex investigation of electrical properties of AlN ceramics with addition of modifying (TiO_2, TiH_2) and conductive phases (HfC) for the application as substrate material for MCM and functionally graded materials for ceramic heaters.

2. Materials and methods

Technically pure AlN powder (95 vol.%) was used for preparation of the pure AlN ceramics (samples AlN) and AlN composites (AlN with various additives: 0.5-4 vol.% TiO_2 (samples 0.5/2/3/4TO), 0.5-3 vol.% TiH_2 (0.5/1/1.5/2/3TH)) (sources: AlN, HfC – Chemical reagents factory *Donetsk-Reagent*, Ukraine; TiO_2, TiH_2 – *Nikolaev* alumina refinery, Ukraine). The powder was ground to 1 μm particle size in a planetary mill for 3 h.

The samples were prepressed in the form of pellets with diameter of 18 mm and thickness of 1 mm. Hot pressing was done by applying pressure of 30 MPa, for 20 min at temperatures between 1700°C and 1900°C increased with 50°C steps.

Active resistive composites were obtained from AlN-2 vol.% TiO_2 dielectric matrix with the addition of 11-17 vol.% HfC (samples 2TO-11/13/15/17HC). Samples were hot pressed at 1970 °C for 25 min under 18 MPa. Resulting dimensions of the samples were 50×8×6 mm.

Relative density was determined as the ratio of bulk and theoretical density. The first one was obtained by Archimedes method, the second was estimated using mixtures rule.

Electrical resistance of the insulator was measured by teraohmmeter. For conductive samples voltmeter-ammeter method was used. Electric properties of dielectric samples were measured at indirect heating from 20°C up to 350°C with the rate of 4±1°C placing the measurement cell into a furnace. Heating of conductive samples was made at direct conditions.

For a.c. measurements of dielectric samples the bridge method was used in low-frequency range (10^2 – 10^5 Hz). Capacitance and loss tangent values were obtained by direct observation. Real and imaginary parts of dielectric permittivity as well as real part of a.c. conductivity were calculated. In radio-frequency region (10^4 – 10^7 Hz) the resonance method was used.

Concentration dependence of electrical conductivity was approximated using effective medium equation (McLachlan's equation) [25]:

$$\theta_i \frac{\sigma_i^{1/s} - \sigma_m^{1/s}}{\sigma_i^{1/s} + \left(\frac{1}{\theta_{crit}} - 1\right)\sigma_m^{1/s}} + \theta_c \frac{\sigma_c^{1/t} - \sigma_m^{1/t}}{\sigma_c^{1/t} + \left(\frac{1}{\theta_{crit}} - 1\right)\sigma_m^{1/t}} = 0, \qquad (1)$$

where σ_i, θ_i, σ_c, θ_c - conductivity and volume content of insulator and conductive phases respectively; θ_{crit} - critical volume content of conductive phase at which charge carriers can freely move from contact to contact (percolation threshold); *t*, *s* –parameters which characterize morphology of inclusion particles, the "shape" factor [26]. A set of *s* and *t* values was given in [25].

3. Results and discussion

3.1 Dielectric composites

The highest density was achieved in AlN samples at 1800°C (99.9%). Addition of titanium oxide increased the temperature of maximal densification on 50°C.

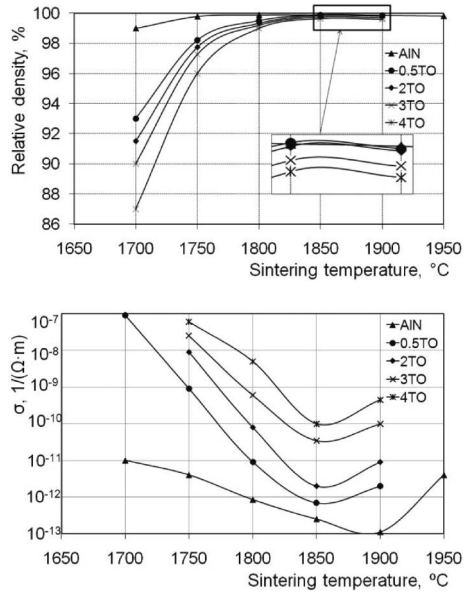

Fig. 3. Effect of sintering temperature and TiO_2 addition on relative density (a) and conductivity (20°C) (b) of AlN ceramics [27]
3. ábra A szinterelő hőmérséklet és a TiO_2 adagolás hatása az AlN kerámiák látszólagos sűrűségére (a) és vezetőképességére (20°C) [27]

Fig. 3 shows that the presence of TiO_2 lowers the density of AlN-TiO_2 composites at sintering temperatures below 1800°C. At the same time, at sintering temperatures of 1850-1900°C relative density of AlN-0.5-2 vol.% TiO_2 composites was equal to that of pure AlN (99.9 %) and decreased with increasing the additive percentage in composites with more than 3 vol.% of TiO_2 (< 99.7 %) (*Fig. 3.a*).

It can be assumed that maximum density of the low doped samples is explained by the formation of fusible eutectic α-Al_2O_3·TiO_2+Al_2O_3 with a melting point of 1840±10 °C which is confirmed by the results of Kume [15]. The presense of aluminium oxide is attributed to the interaction between aluminium nitride and water under milling.

Minimal d.c. conductivity for AlN samples without additives was observed at T_{sint} = 1900°C (*Fig. 3.b*). TiO_2 addition lowers the temperature of minimal conductivity on 50 °C despite of the additive percentage. Increase of TiO_2 amount from 0.5 to 4 vol.% increased conductivity of the composites from $7 \cdot 10^{-13}$ up to $1 \cdot 10^{-10}$ 1/Ω·m due to TiN formation in AlN ceramics as a result of the reaction between TiO_2 and AlN at temperatures >1600°C.

It can be noticed that despite of Kume's results [12] (*Fig. 4*), addition of TiO_2 in amount of >1.5 vol.% increases dielectric loss tangent. Thus, it can be assumed that at first addition of titanium oxide improves *tan δ* due to the low loss tangent of TiO_2 (< 10^{-3}) but then after in-situ formation of TiN complexes an opposite effect can be observed.

Dielectric permittivity of AlN composites with TiO_2 and TiH_2 addition decreases with the temperature (up to optimal sintering temperature) and increases at increasing of amount of the additive (*Fig. 5*).

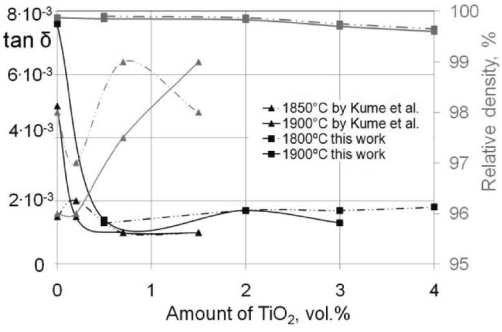

Fig. 4. Effect of TiO_2 addition on loss tangent and relative density of AlN ceramics [27]
4. ábra A TiO_2 adagolás hatása az AlN kerámiák tangens veszteségére és relatív sűrűségére [27]

Fig. 5 indicates that *ε′* and *tan δ* decreased over all frequency range. A threshold decline of permittivity and maximum of loss tangent at 10^5-10^6 Hz were observed. Frequency dispersion of *ε′* and *tan δ* respond to space-charge polarization (at low frequencies) and hopping polarization (at radio frequencies). The first one usually "turns off" at lower frequencies (10^{-3}-10^3 Hz at 300 K). But in the case of the present studies this disabling was observed at higher frequency ($f_d = 2.5 \cdot 10^5$ Hz).

Ceramics and polycrystalline materials are usually multiphase systems. The difference of the concentration of the charge carriers of these phases causes polarization at the boundaries which is usually considered as Maxwell-Wagner's (M-W). The model of it can be described by a conductive layer with constant value of electric conductivity *σ*. In this case the system is characterized by uniform electric field so all the charges are located only on the interfaces and space charge is neglected. According to Trukhan [28] who described such system to be uniform (heterogeneous) dielectric without leakage currents (but with losses), both flat conductive layers and conductive spherical particles surrounded by dielectric medium, *ε′* (*ε′* = *ε*) decreases monotonically with frequency and *ε″* has its maximum at the dispersion region. Dispersion frequency can increase with increasing the dielectric contribution (geometrical enlargement or decrease of permittivity). It asymptotically approaches to Maxwell-Wagner's dispesion frequency when concentration of charge carriers rises. As the variation of conductor parameters in heterogeneous systems almost always exists, dispersion is less sharp than it follows from the theory of Maxwell-Wagner.

If the heterogeneous system is assumed as flat conductive layers (with a width of *d*) surrounded by a dielectric medium with low charge concentration, then the effective thickness of conducting channel *d* can be estimated on the basis of the equation for frequency dispersion [34]:

$$\omega_d = 2\pi f_d = \frac{12D}{d^2} \tag{2}$$

where *D* is the diffusion coefficient for the electron in the medium considered, which can be calculated from Einstein's equation:

$$De = \mu kT \tag{3}$$

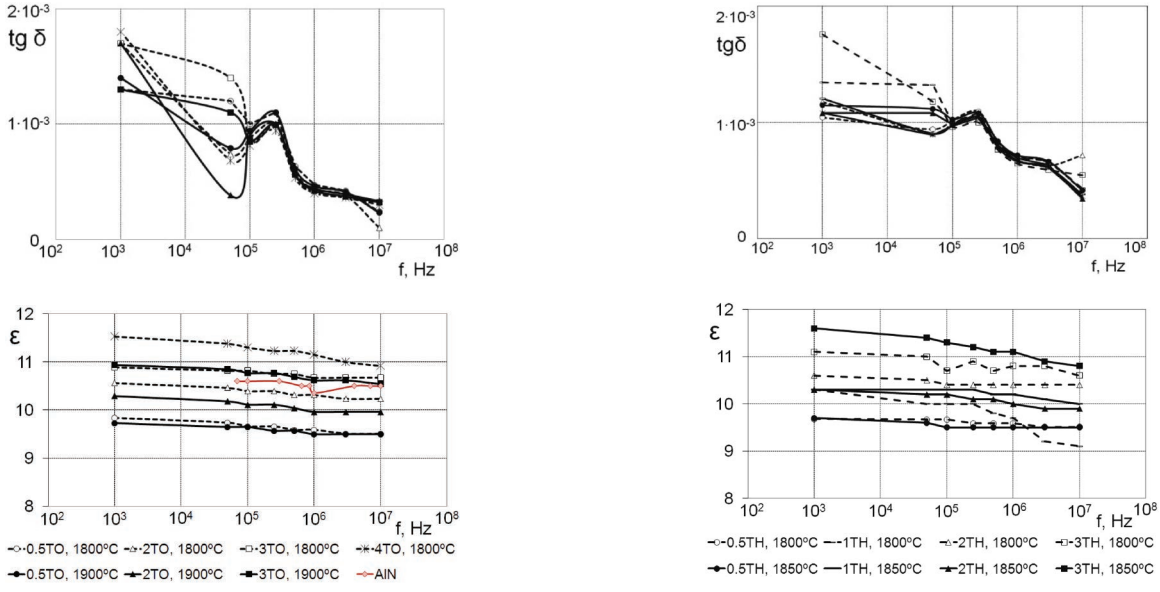

Fig. 5. Frequency dependences of dielectric permittivity and loss tangent of pure AlN, AlN-TiO_2 (a) [27] and AlN-TiH_2 (b) ceramics obtained with different additives and sintering temperatures
5. ábra Az adalékok hatása AlN kerámiák dielektromos állandójának és tangens veszteségének frekvencia-függőségére: (a) AlN és AlN-TiO_2 [27]; (b) AlN-TiH_2

If charge mobility μ in AlN is assumed to be equal to 14 cm^2/V·sec (at 290 K), it gives the value of D = 0.35 cm^2/sec.

Thus from (2) the value of d = 16 μm can be obtained. All the samples regardless of the amount and type of the additives had the same frequency of dispersion and subsequently an effective thickness of conductive channel. In the authors opinion, it is a typical situation for the materials below the percolation threshold.

The mechanism of charge transfer in amorphous materials is primarily hopping. Subsequently a.c. conductivity is the sum of leakage and bias conductivity: $\sigma(\omega) = \sigma_0 + \omega\varepsilon\varepsilon_0 tg\delta$, where σ_0 – d.c. conductivity, ω – angular frequency, ε – relative permittivity of the material, ε_0 – the electric constant, $\varepsilon_0 = 8.85 \cdot 10^{-12}$ F/m, $tg\delta$ – loss tangent. This equation can be expressed as $\sigma(\omega)\omega^n$. In all the previous works [29, 30] where a number of n values was given it was believed that $n \leq 1$.

Although in contrast to electrons, ions move much smaller, nearest-neighbor distances, neither the magnitude of a.c. conductivity, its activation energy nor its frequency dependence can be taken as guides to the nature of the dominant carrier responsible for polarization [29]. However, it is known that aluminum nitride has a wurtzite structure and the covalence bond degree ≈ 60%.

So the frequency dependence of a.c. conductivity can be considered within Jonscher's universal power law. The slope of it in logarithm coordinates results an exponent which values can be found in the range $0.5 < n < 0.9$ are closely associated with hopping electrons, $n \approx 1$ are to be associated with the "lattice" response. The distinction between "lattice" and "carrier" responses corresponding to "intrinsic", that is irreducible, and "extrinsic" processes due to some impurities or injected carriers, may prove to be useful tools in the assessment of dielectric materials [29].

Four plots with different slopes can be distinguished on the frequency dependence of active part of admittance: at low- (10^3–10^5 Hz, 10^5 Hz) and radio-frequencies (10^6 Hz, $3 \cdot 10^6$-10^7 Hz). The second and the third plots have the same slope regardless of the type or amount of the additive and sintering temperature: ≈ 1.1 (for the second) and 0.8 (with TiO_2) - 0.9 (other additives) (for the third one) which reveal dielectric response of AlN grain.

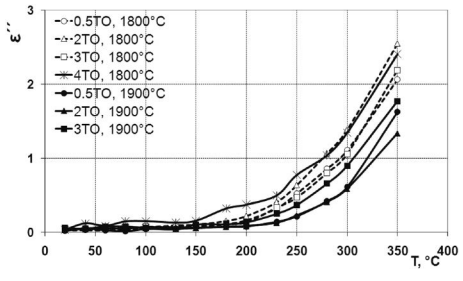

Fig. 6. Temperature dependence of dielectric loss factor of AlN-TiO_2 ceramics obtained at different sintering temperatures

6. ábra Az eltérő hőmérsékleten szinterelt AlN-TiO_2 kerámiák dielektromos vesztesége a hőmérséklet függvényében

In radio-frequency range the value of n of AlN-TiO_2 composites increases from 0.5 to 0.8-0.9 at increase of TiO_2 concentration regardless of sintering temperature. In AlN-TiH_2 composites increase of TiH_2 amount increases n from 0.5 to 0.9-1. At higher sintering temperatures (1850-1950 °C) n = 0.4-0.5 irrespective of titanium hydrate concentration.

The present studies have demonstrated that n could be higher than unity in contrast to the most common opinion that it is always less than 1. Thus obtained results require further more deeply theoretical understanding.

Dielectric loss factor did not change with the temperature below 150°C and increased with it above (*Fig. 6*) which indicates conduction losses. Deviation from optimal sintering temperature increases ε'' that is associated with the formation of structure defects.

3.2 Active resistive composites

All AlN-TiO_2-HfC composites had high density, 97.5–99.5%.

As it can be seen from the percolation curve (*Fig. 7*), resistivity of the composites decreases with increasing concentration of conductive additive HfC. At the lowest HfC content (11%) the resistivity is equal to 0.15 Ω·cm. Such low value shows that all the studied concentrations are beyond the percolation threshold.

Metallographic analysis of composites showed (*Fig. 7*) that conductive clusters are formed in a shape of longitudinally elongated structure under the influence of magnetic field.

Modeling of percolation curve gives the values of percolation threshold θ_{crit} = 9.9% and coefficient t = 1.35. Besides, SIAMS analysis showed that the ratio of conductive phase was ≈ 7.9% (for 2TO-11HC samples).

According to [25] t characterizes the shape of inclusion particles and it is associated with "demagnetization or depolarization" coefficients L_c and L_i of conductive and insulator phase via equation:

$$t = \frac{1}{1 - L_c - L_i} \tag{4}$$

Assuming $L_c = L_i$ one can obtain L_c = 0.13 which according to [25] indicate the formation of disk-shaped particles. Comparing these results with *Fig. 7* authors believe that 3D morphology of conductive particles is elongated in the third direction. The fact that actual ratio of conductive phase is lower than expected confirms authors' assumption.

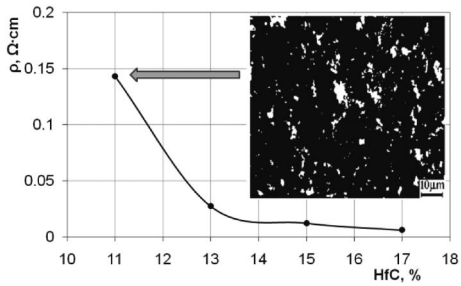

Fig. 7. Concentration dependence of resistivity of AlN-TiO_2-HfC composites and microstructure of 2TO-11HC samples

7. ábra AlN-TiO_2-HfC kompozitok elektromos ellenállásának koncentráció-függősége és a 2TO-11HC minták mikro-szerkezete

Temperature dependence of electric resistivity is linear (*Fig. 8*). Steady positive temperature coefficient of resistance (*Fig. 8*) for all the studied concentrations of HfC in a wide temperature range makes AlN-HfC ceramic heaters the contenders to the

analogues used today [3]. Besides, ceramic gradient materials provide higher thermal shock and crack resistance because of similarity of thermal expansion coefficient of the components (5.6 10^{-6} and 4.6 10^{-6} K^{-1} for HfC and AlN respectively).

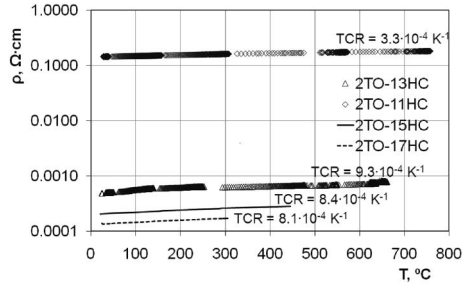

Fig. 8. Temperature dependence of electric resistivity and temperature coefficient of resistance of AlN-TiO_2-HfC composites
8. ábra AlN-TiO_2-HfC kompozitok elektromos ellenállásának hőmérséklet-függősége és az ellenállás hőmérséklet koefficiense

Dependence of the surface temperature on the applied power density (*Fig. 9*) showed that all the composites beyond percolation threshold have the same characteristics despite of the conductive phase content.

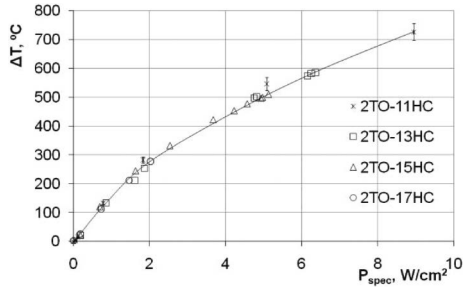

Fig. 9. Dependence of the temperature (the difference between surface temperature and the temperature of environment) on the applied power density of AlN-TiO_2-HfC composites
9. ábra AlN-TiO_2-HfC kompozitok relatív hőmérséklet-függősége (a környezeti és a felületi hőmérséklet különbsége) az alkalmazott energiasűrűség függvényében

4. Conclusions

AlN-1.5-2%TiO_2 ceramics showed good electrical properties (low porosity (0.1%), dielectric permeability (9.7) and dielectric loss tangent ($1.3 \cdot 10^{-3}$)) and can serve as ceramic dielectric substrates and dielectric matrix for functionally graded materials. Addition of 11-17% HfC allows obtaining heating elements with required characteristics.

It was shown that addition of small amount of TiO_2 (up to 1.5-2%) increases density and reduces dielectric loss of the composites. But further increase of the additive content has the opposite effect. Deviation from the optimal sintering temperature leads to the formation of structure defects and increases dielectric loss.

Broadband dielectric spectroscopy was used for the nondestructive testing of microstructure: dispersion frequency gives information about the effective thickness of a conductive channel; the slope of $\sigma(\omega)$ dependence gives distinction between "lattice" and "carrier" responses corresponding to "intrinsic", which is irreducible, and "extrinsic" processes due to some impurities or injected carriers.

References

[1] Brodnikovska, I. V. – Soltis, M. V. – Kirilenko, K. V. – Zvorskii, I. V. – Petrovskii, V. Ya.: Effect of the particle size of conductive inclusions on the structurization and resistivity of Si_3N_4–ZrC ceramics, *Powder Metall. Met. Ceram.*, Vol. 51 (2012) 307-315. http://dx.doi.org/10.1007/s11106-012-9433-2

[2] Petrovsky, V.: Electrical response on microstructure evolution of multicomponent ceramic matrix materials, *J. Mater. Sci. Eng.*, Vol. 4, № 2 (2010) 39-51.

[3] http://americas.kyocera.com/kicc/pdf/Kyocera%20Ceramic%20Heaters.pdf

[4] Isobe, T. – Daimon, K. – Sato, T. – Matsubara, T. – Hikichi, Y. – Ota, T.: Spark plasma sintering technique for reaction sintering of Al_2O_3/Ni nanocomposite and its mechanical properties, *Ceram. Int.*, 34 (2008) 213–217. http://dx.doi.org/10.1016/j.ceramint.2006.08.017

[5] Mclachlan, D. S. – Cai, Kefeng – Sauti, G.: AC and dc conductivity-based microstructural characterization, *Int. J. Refract. Met. H.*, 19 (2001) 437-445. http://dx.doi.org/10.1016/S0263-4368(01)00024-5

[6] Yang, H. – Shang, F. – Gao, L.: Microstructure and mechanical properties of gas pressure sintered Al_2O_3/TiCN composite, *Ceram. Int.*, 33 (2007) 1521–1524. http://dx.doi.org/10.1016/j.ceramint.2006.07.001

[7] Chinelatto, A. S. A. – Contardi, O. A. – Pallone, E. M. S. A. – Tomasi, R.: Production of Alumina Matrix Nanocomposites with Inclusions of TiC and TiB_2 via Reactive Milling, *Key Eng. Mater.*, Vols. 189-191 (2001) 208-215. http://dx.doi.org/10.4028/www.scientific.net/KEM.189-191.208

[8] Yokoyama, H. – Obata, S. – Kato, N. – Hotta, T. – Abe, H. – Naito, M. – Hirano, S.: Preparation of Three Dimentionally Electroconductive Pattern of Si_3N_4-TiN system by Ink Jet Printing, *J. Ceram. Soc. Jpn*, Suppl. 112-1, PacRim 5 Special Issue, 112 [5] (2004) 144-S148. https://www.jstage.jst.go.jp/article/jcersjsuppl/112/0/112_0_S144/_pdf

[9] Zivkovic, L. – Nikolic, Z. – Boskovic, S. – Miljkovic, M.: Microstructural characterization and computer simulation of conductivity in Si_3N_4–TiN composites, *J. Alloys Compd.*, 373 (2004) 231–236. http://dx.doi.org/10.1016/j.jallcom.2003.10.036

[10] Krnel, K. – Sciti, D. – Landi, E. – Bellosi, A.: Surface modification and oxidation kinetics of hot-pressed AlN–SiC–$MoSi_2$ electroconductive ceramic composite, *Appl. Surf. Sci.*, 210 (2003) 274–285. http://dx.doi.org/10.1016/S0169-4332(03)00155-7

[11] Kai, A. – Hirata, H. – Miki, T.: Effects of TiH_2 Coating and Insertion of Ti and Cu Foils, *J. Ceram. Soc. Jpn*, Suppl. 112-1, PacRim5 Specials Issue, 112 [5] (2004) 117-118. https://www.jstage.jst.go.jp/article/jcersjsuppl/112/0/112_0_S117/_pdf

[12] Kume, S. – Yasuoka, M. – Omura, N. – Watari, K.: Effect of Additives on Dielectric Loss of AlN Ceramics, *Key Eng. Mater.*, Vols. 317-318 (2006) 845-848. http://dx.doi.org/10.4028/www.scientific.net/KEM.317-318.845

[13] Kume, S. – Yasuoka, M. – Watari, K.: Effect of Lanthanum Oxide Addition on Dielectric Loss and Microstructure of AlN Ceramics, *Key Eng. Mater.*, Vol. 320 (2006) 197-200. http://dx.doi.org/10.4028/www.scientific.net/KEM.320.197

[14] Jang, S. A. – Choi, G. M.: Effect of Dopants on the Complex Impedance and Dielectric Properties of Aluminium Nitride, *J. Am. Ceram. Soc.*, 75 [11] (1992) 3145-3148. http://dx.doi.org/10.1111/j.1151-2916.1992.tb04402.x

[15] Kume, S. – Yasuoka, M. – Omura, N. – Watari, K.: Effect of Additives on Dielectric Loss of AlN Ceramics, *Key Eng. Mater.*, 317-318 (2006) 845-848. http://dx.doi.org/10.4028/www.scientific.net/KEM.317-318.845

[16] Fesenko, I. P. – Kuzenkova, M. O. – Oleynik, G. S.: Reinforced n-AlN-ceramics, *Functional Gradient Materials and Surface Layers Prepared by Fine Particles Technology*, *Science Series II. Mathematics, Physics and Chemistry*, Kluwer Academic Publishers, Dordrecht/Boston/London, 16 (2001) 257–264.

[17] Freedman, M. R. – Kiser, J. D. – Herbell, T. P.: Factors influencing the ball milling of Si_3N_4 in water, *Ceram. Eng. Sci. Proc.*, 6 [7/8] (1985) 1124–1134.

[18] Tkachenko, Y. G. – Morozova, R. A. – Yurchenko, D. Z. – Shevchenko, O. A. – Morozov, I. A. – Satanin, S. V.: Effects of chemicothermal treatment of aluminum nitride powders on the structure and properties of the resulting

hot-pressed ceramics, *Powder Metall. Met. Ceram.,* 34 (1995) 69-73. http://dx.doi.org/10.1007/BF00559854
[19] Brodnikovska, I. V. – Vorona, Yu. V. – Petrovskyi, V. Ya.: Receiving of high-temperature dielectrics and heat-spreading substrates on the basis of silicon nitride, *Ceramics: science and life*, 3 (17) (2012) 14-29 (in Russian).
[20] Monteverde, F. – Medri, V. – Bellosi, A.: Microstructure of hot-pressed Ti(C,N)-based cermets, *J. Eur. Ceram. Soc.*, 22 (2002) 2587–2593. http://dx.doi.org/10.1016/S0955-2219(02)00120-6
[21] Köbel, S. – Plüschke, J. – Vogt, U. – Graule, T. J.: $MoSi_2$–Al_2O_3 electroconductive ceramic composites, *Ceram. Int.*, 30 (2004) 2105–2110. http://dx.doi.org/10.1016/j.ceramint.2003.11.015
[22] Petrovsky, V. Ya. – Rak, Z. S.: Densification, microstructure and properties of electroconductive Si_3N_4–TaN composites. Part II: Electrical and mechanical properties, *J. Eur. Ceram. Soc.*, Vol. 21, Is. 2 (2001) 237-244. http://dx.doi.org/10.1016/S0955-2219(00)00198-9
[23] Yang, J. Z. – Huang, Z. H. – Fang, M. H. – Liu, Y. G. – Huang, J. T. – Hu, J. H.: Preparation and mechanical properties of Fe/Mo–Sialon ceramic composites, *Scripta Mater.,* Vol. 61, Is. 6, (2009) 632-635. http://dx.doi.org/10.1016/j.scriptamat.2009.05.042
[24] Savino, R. – De Stefano Fumo, M. – Silvestroni, L. – Sciti, D.: Arc-jet testing on HfB_2 and HfC-based ultra-high temperature ceramic materials, J. Eur. Ceram. Soc., 28 (2008) 1899–1907. http://dx.doi.org/10.1016/j.jeurceramsoc.2007.11.021
[25] McLachlan, D. S. – Blaszkiewicz, M. – Newnham, R. E.: Electrical resistivity of composites, *J. Am. Ceram. Soc.*, Vol. 73, Is. 8 (1990) 2187-2203. http://dx.doi.org/10.1111/j.1151-2916.1990.tb07576.x
[26] Runyan, J. – Gerhardt, R. A.: Electrical properties of boron nitride matrix composites: I. Analysis of Mclachlan equation and modeling of the conductivity of boron nitride-boron carbide and boron nitride-silicon carbide composites, *J. Am. Ceram. Soc.*, Vol. 84, Is. 7 (2001) 1490-1496. http://dx.doi.org/10.1111/j.1151-2916.2001.tb00866.x
[28] Trukhan, E. M.: Dispersion of dielectric permittivity of heterogeneous systems, *Solid State Physics*, 4 [12] (1962) 3496-3511 (in Russian).
[29] Joscher, A. K.: The "universal" dielectric response", *Nature*, 267 (1977) 673-679. http://dx.doi.org/10.1038/267673a0
[30] Brodnikovska, I. V. – Petrovskyi, V. Ya.: Non-destructive monitoring of Si_3N_4 ceramic composites: I. Investigation of phase composition in Si_3N_4-Al_2O_3-TiH_2, Si_3N_4-Al_2O_3-TiO_2, Si_3N_4-Al_2O_3-ZrH_2 composites, obtained with different sintering temperature, *Ceramics: science and life,* 1 (15) / 2 (16) (2012) 39-53 (in Ukrainian).

Ref.:
Brodnikovska, Iryna V. – **Deriy**, Andriy I. – **Petrovsky**, Vitaly Ya.: *Development of AlN ceramic composites for multilayer ceramic devices*
Építőanyag – Journal of Silicate Based and Composite Materials, Vol. 66, No. 3 (2014), 58–63. p.
http://dx.doi.org/10.14382/epitoanyag-jsbcm.2014.12

AlN kerámia kompozit fejlesztése rétegelt kerámia alkatrészekhez

Az AlN kerámia alkatrészek mechanikai és villamos tulajdonságai jelenős mértékben függ a fázis-összetételtől és a szinterelési hőmérséklettől. A HFC mint vezető réteg mellé a szerzők az anyagszerkezet és a mechanikai tulajdonságok módosításához a TiO_2 és TiH_2 adalékanyagokat használtak. Magát az AlN kerámiát, mint a dielektromos és vezető rétegek szátválasztására szolgáló funkcionális anyagot alkalmazták. Az elvégzett vizsgálatok azt mutatták, hogy az (1,5–2)% TiO_2 tartalmú AlN kerámia kompozit kiemelkedő dielektromos tulajdonságokkal rendelkezik, és mintegy (11–17)% HFC hozzáadásával kiváló, hatékony kerámia fűtőelem gyártható belőle. A szerzők a mikroszerkezet roncsolásmentes vizsgálatához szélessávú dielektromos spektroszkópot használtak. A diszperziós frekvencia információt adott a vezetőképes csatornák tényleges vastagságáról; a σ(ω) függvény meredeksége alapján megkülönböztethetők a „rács" és a „szállító" alkotók, ami az adott anyagra jellemző „belső" megváltozhatatlan tulajdonság.
Kulcsszavak: alumínium-nitrid kerámia, szinterelés, dielektromos tulajdonság, funkcionális anyagok

Útpályaszerkezetből vett fúrt magminták szemrevételezése és értékelése CT-vel

LUBLÓY ÉVA ▪ Budapesti Műszaki és Gazdaságtudományi Egyetem, Építőanyagok és Mérnökgeológia Tanszék ▪ lubloy.eva@ epito.bme.hu
FÖLDES TAMÁS ▪ Kaposvári Egyetem Diagnosztikai Intézet
AMBRUS DÁVID ▪ Budapesti Műszaki és Gazdaságtudományi Egyetem, Út és Vasútépítési Tanszék ▪ ambrus.david@epito.bme.hu
KAPITÁNY KRISTÓF ▪ Budapesti Műszaki és Gazdaságtudományi Egyetem, Fotogrammetria és Térinformatika Tanszék
BARSI ÁRPÁD ▪ Budapesti Műszaki és Gazdaságtudományi Egyetem, Fotogrammetria és Térinformatika Tanszék

Érkezett: 2014. 04. 20. ▪ Received: 20. 04. 2014. ▪ http://dx.doi.org/10.14382/epitoanyag-jsbcm.2014.13

Computed tomography analysis and visual inspection of asphalt core samples
The air void and aggregate content of asphalt core samples could be determined by direct and indirect methods. Direct methods are destructive since they determine the air void and aggregate content by decomposing the mix into its individual components. The computed X-ray tomography (CT) makes it possible to create a 3D image of the complete inner structure. This paper demonstrates the CT method for determining the air void content in asphalt. It shows that the proposed method can determine the air void and aggregate content and gives multiple additional information about other features by showing the distribution along the vertical axis of the core sample.
Keywords: computed tomography, CT, asphalt, non-destructive testing, air void content, aggregate content.
Kulcsszavak: computer tomográfia, CT, aszfalt, roncsolásmentes vizsgálat, légzárvány-tartalom, adalékanyag-tartalom

Lublóy Éva
okl. építőmérnök (BME Építőmérnöki Kar 2002), adjunktus a BME Építőanyagok és Mérnökgeológia Tanszékén (2002). Fő érdeklődési területei: vasbetonszerkezetek viselkedése tűz hatására, tűzkárok mérnöki tanulságai. A *fib* Magyar Tagozat tagja.

Földes Tamás
okl geológus (ELTE 1979) 2005-ig a Kőolajkutató vállalatnál majd pedig a MOL Rt-nél dolgozott. 2006-tól a Kaposvári Egyetem Diagnosztikai Intézetének munkatársa. 1999-től végez CT és MR mérési értékeléseket élettelen vizsgálati anyagokon, elsősorban kőzeteken. Fő érdeklődési területe: szénhidrogén rezervoár geológiai modellezés, nagyfelbontású képalkotó roncsolásmentes mérések (CT, microCT, MR) élettelen anyagvizsgálati módszerek kiértékelése. Magyarhoni Földtani Társulat, Geofizikai Társulat és az EAGE tagja.

Ambrus Dávid
okl. építőmérnök (BME Építőmérnöki Kar 2008), mérnök a BME Út és Vasútépítési Tanszéken (2012). Fő érdeklődési terület: aszfalt mechanika, aszfalt technológia, úttervezés.

Kapitány Kristóf
Építőmérnöki (térinformatikus) BSc diplomáját 2009-ben szerezte meg, majd Földmérő- és térinformatikai mérnök MSc diplomáját 2012-ben. Azóta PhD tanulmányait folytatja a Budapesti Műszaki és Gazdaságtudományi Egyetem, Fotogrammetria és Térinformatika Tanszékén, Objektumrekonstrukció orvosi képekből témában, mely keretein belül orvosi felvételsorozatok automatikus kiértékelésével foglalkozik.

Barsi Árpád
a BME Fotogrammetria és Térinformatika Tanszék vezetője, egyetemi tanár. Diplomáját 1994-ben szerezte a BME Építőmérnöki Karán, 1998-ban PhD fokozatot szerzett, 2004-ben habilitált. Tagja az IEEE Computer Society-nek, a német Fotogrammetriai és Távérzékelési Társaságnak (DGPF), az MTA Geodéziai Tudományos Bizottságának, a Nemzetközi Fotogrammetriai és Távérzékelési Társaság (ISPRS) közgyűlési tagja. Érdeklődési területe: digitális képfeldolgozás, mesterséges intelligencia, lézerszkennelés, navigáció, térinformatikai elemzések.

1. Bevezetés

Helyszínen vett minták szemrevételezése elengedhetetlen és nagyon jól kiegészíti a laboratóriumi méréseket. A számítógépes tomográfiás (Computed Tomography – CT) vizsgálatokkal a minták háromdimenziós elemezése válik lehetővé. A különböző hibákra a CT-felvételeken és azok elemzése során előbb felfigyelhetünk, mint a laboratóriumi mérések során, hiszen ha a hiba a réteghatáron belül van, akkor az szabad szemmel nem látható. A CT-vel történő elemzés során viszont ezek a hibahelyek is kimutathatóak.

2. Az útpályaszerkezetek felépítése

Az útpályaszerkezet a következő fő részekből áll *(1. ábra)*:
- burkolat, ami tartalmazza a kopó- és a kötőréteget,
- alap,
- ágyazat,
- javított talajréteg.

Megkülönböztetünk hajlékony, azaz bitumen kötőanyagú, illetve merev, azaz cement kötőanyagú pályaszerkezeteket.

Jelen cikken belül az aszfalt burkolati rétegekkel és azok hibáinak kimutatási lehetőségeivel foglakozunk. Az aszfalt bitumen kötőanyagból és adalékanyagból áll.

A bitumennel szemben támasztott követelmény, hogy ne legyen hőérzékeny, lassan öregedjen és vonja jól körbe az adalékanyagot.

Az aszfaltban alkalmazott ásványi adalékanyagok és azok szemcsenagysága:
- zúzott kövek >20 mm,
- zúzalék 4-20 mm,
- zúzott homok 0,1-4 mm,
- kőliszt <0,1mm.

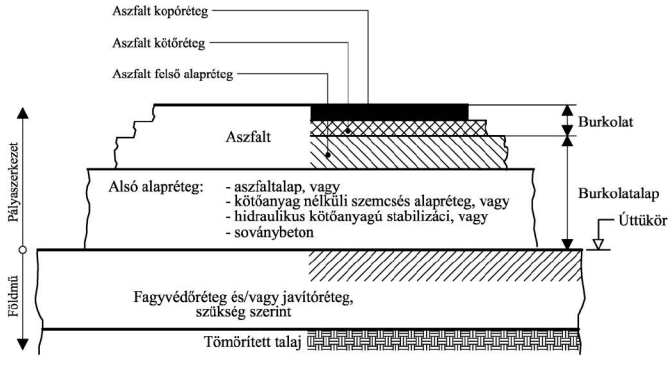

1. ábra Az útpályaszerkezet felépítése
Fig. 1. Structure of pavement

A kopórétegben a zúzott anyagok bazaltból, illetve andezitből készülnek, a kőliszt pedig mészkőből.

Az adalékanyaggal szemben támasztott követelmények:
- megfelelő ütőszilárdság,
- megfelelő kopószilárdság,
- megfelelő időállóság.

3. Miért fontos a hibahelyek kiszűrése?

A burkolat hibái a pályaszerkezet leromlását eredményezik. A burkolatból kifúrt magminták szemrevételezésével megállapítható több, a szállítás és beépítés körülményeire jellemző esemény. Az elvárható beépítési követelmények betartása esetén elsősorban a réteg alsó része a kritikus, mert az találkozik a fogadó réteg hidegebb felületével, és az ott bekövetkező gyors lehűlés hatására a tömörítés hatékonysága csökken. Azonban a belső térbeli struktúráról nem kapunk valós képet; ahhoz háromdimenziós elemzés lenne szükséges, ami a CT felvételek segítségével lehetséges [1].

A hibák többségének okozója a burkolati réteg helytelen kivitelezése, ezért annak vizsgálatát kiemelten fontosnak tartjuk.

A kutatás során aszfaltburkolatú útpályaszerkezetekből fúrt magmintákat szemrevételeztünk és vizsgáltunk CT-vel. A cél az egyes aszfalt pályaszerkezeti rétegek hibáinak és hibahelyeinek meghatározása volt. Kutatásunkkal azt vizsgáltuk, hogy a CT mérések pontosabb eredményt adnak-e és ezeket hol és hogyan tudjuk hasznosítani.

A kutatás során összesen 2 db fúrt magmintát vizsgáltunk meg részletesen. A minták magyarországi aszfalt pályaszerkezetű út teherbírás-növelése érdekében megerősített szakaszairól származnak. Az egyik minta esetében a megerősítés során az eredeti burkolat felső 2 cm-ét marással eltávolították, és erre került rá két rétegben az új aszfalt burkolat. A másik minta esetében pedig teljes elbontás után három új aszfaltréteg került beépítésre. A fúrt magminták az alaprétegig tartalmazzák az új és az eredeti pályaszerkezeti rétegeket.

A CT felvételek segítségével az egyes rétegek szerkezete, hézagtartalma részletesen elemezhető és az esetleges hibahelyek kiszűrhetőek.

4. Vizsgálati eredmények

A CT (Computed Tomography) a szakirodalomban gyakran számítógépes tomográfia néven ismeretes, amely a radiológiai diagnosztika egyik ága.

A CT készülékek röntgensugárzást használnak a felvételek elkészítéséhez, de a sugarak nem filmet exponálnak, hanem detektorok segítségével érzékelik a röntgensugarakat, majd a detektorokból nyert elektromos jelekből készül el számítógép segítségével a rekonstruált keresztmetszeti kép. A tomográfiás felvétel esetében vékony, síkszerű röntgensugár-nyalábbal világítják át a vizsgált objektumot. A modern CT-berendezések két röntgen csövet tartalmaznak és egy körülfordulás alatt egyszerre több szeletet vizsgálnak. A vizsgálat a szükséges számításokkal együtt néhány perc alatt elvégezhető [2]. A teljes kiértékelés további feladatokat jelent.

A mérés az anyagok eltérő sugárgyengítési tulajdonságain alapul. A μ sugárgyengítési együttható az anyagra jellemző tulajdonság, ami az anyag sűrűségétől és a röntgensugárzás spektrumától függ.

A kép minden egyes pixele ekkor egy-egy értékkel rendelkezik, ami az adott térfogatelem relatív lineáris sugárgyengítését mutatja.

A skála fix pontjai a víz ún. Hounsfield értéke (Hounsfield Unit – HU), ami 0, valamint a levegő Hounsfield értéke, ami -1000. A pozitív oldalon általában 3000-ig tart a skála. A modern készülékeken lehetőség van a skála kiterjesztésére, ezáltal részletesebb felosztására is. A digitális képfeldolgozás során az egyes voxelekhez (= volume pixel – három dimenziós képpont) rendelt érték tehát -1000 és +3000 között lehet [2].

4.1 Kopóréteg

A *2. ábrán* 4 cm vastagságban beépített kopóréteg aszfalt magminta darabja látható. Az oldalnézeten nem látunk különösebb problémára utaló jeleket, csupán a réteg alsó harmadában látható néhány kisebb légzárvány.

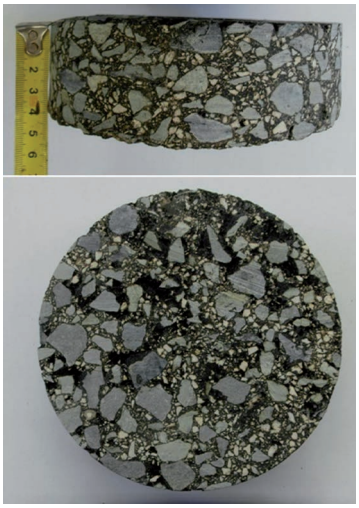

2. ábra Az 1. minta kopóréteg metszete (felül: a furat magminta egy szelete; alul: a furat magminta felülnézete)
Fig. 2. A section of the 1st sample's surface course (above: a section of the asphalt core; below: the top-view of the asphalt core)

A magminta aljáról készült felvételen viszont már több probléma állapítható meg. Láthatóan szétosztályozódott a keverék (ez lehet a hosszabb szállítási út következménye). A fogadó felület alacsony hőmérséklete miatt gyors lehűlés következett be és a réteg alján finom anyaggal kitöltetlen üregek, légzárványok keletkeztek.

A szétosztályozódás miatt a durvább (nagyobb szemnagyságú) zúzalékszemcsék közötti kitöltetlen üregek mérete és mennyisége nagy. Az ilyen összefüggő, nagy hézagok részben lecsökkentik a rétegtapadást, az együttdolgozást, másrészt lehetőséget adnak a bejutó víz felhalmozódására és transzportjára.

A burkolati réteg minőségének megítélése szempontjából – mivel a réteg felületével kapcsolatban lévő üregek a hagyományos aszfaltsűrűség-méréssel nem mutathatók ki – problémát jelent, hogy a ténylegesnél lényegesen kisebb hézagtartalom kerül meghatározásra, tehát egy látszólag jó minőségű réteg mehet idő előtt tönkre.

A *3. ábrán* megadtuk az 1. minta kopóréteg Hounsfield-érték eloszlását és sűrűségeloszlását (*jobb alsó ábrarész*). Jól látható, hogy a kopóréteg alján és tetején nagyobb a hézagtartalom (*bal alsó és középső ábrarész*), amit a tömörítéssel tudunk magyarázni. A réteghatárig nem egyenletes a sűrűség- és a hézagtartalom eloszlása. A mintán belül két metszet mentén vizsgáltuk a hézagtartalmat és a Hounsfield-értéket (*jobb alsó ábrarész*): az 1. metszet esetén kis hézagtartalom és nagy Hounsfield-érték, a 2. metszet esetén nagy hézagtartalom és kis Hounsfield-érték volt megfigyelhető. A hézagtartalom növekedése a szétosztályozódásra utal.

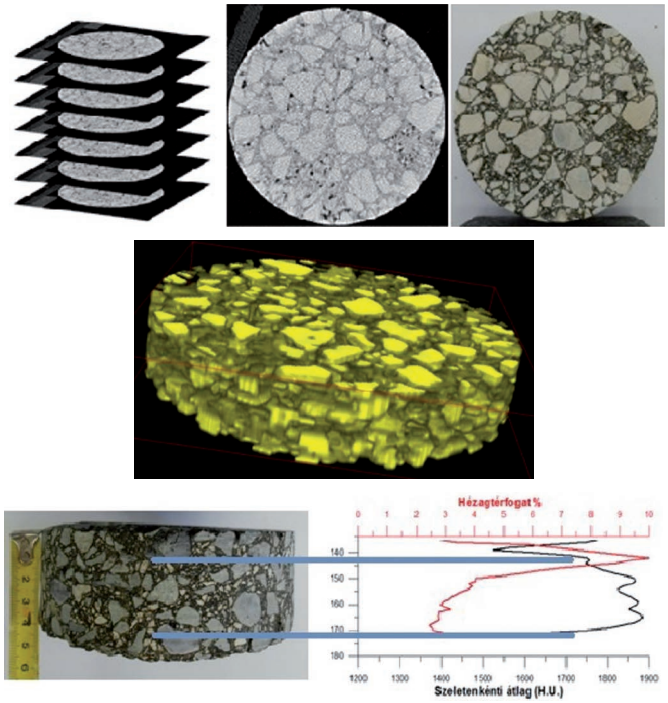

3. ábra Az 1. minta kopórétegének elemzése CT-vel (bal felső: Egy vizsgált mintametszet bal alsó: A szeleten belüli hézagtérfogat és Hounsfield érték eloszlás; jobb felső: CT-s felvételek egymáshelyezésével nyert modell; jobb középső Egy szelet a próbatestből; jobb alsó A szelet 3D-s képe)

Fig. 3. The CT analysis of the 1st sample's surface course (upper left: A section of the sample; lower left: The distribution of air void's volume and Hounsfield units in the section; upper right: sequence of CT images; middle right: A cut face of the sample and the relevant CT slice; lower right: The 3D view of the section.)

A metszetről készült fényképen és a CT-felvételeken is jól látszik, hogy a felszíntől mintegy 4 cm távolságban a szemszerkezet eltér, ami a már korábban említett szétosztályozódással, tömörítéssel magyarázható.

A *4. ábrán* bemutatott kopóréteg az előzővel azonos építéshelyről származik, azonban a mintavétel helyén nem 4 cm, hanem 6 cm vastagságban történt a kopóréteg beépítése. A szállított anyag homogenitása lényegesen jobb, a durva szemek eloszlása egyenletesebb, ezért a réteg aljának lehűlése is kisebb problémát okozott; azt lehet mondani, hogy a szokásos nagyságrendet nem haladja meg a kialakult üregek mérete és mennyisége.

A *5. ábrán* megadtuk a 2. minta kopórétegének Hounsfield-érték eloszlását és sűrűségeloszlását. Jól látható, hogy a kopóréteg alján és tetején nagyobb a hézagtartalom, amit a tömörítéssel tudunk magyarázni. A réteghatárig azonban egyenletes a sűrűség és a hézagtartalom-eloszlás. A mintán belül két metszetet készítettünk, és elemeztük a hézagtartalmat valamint a Hounsfield-értéket: az 1. metszet esetén kis hézagtartalom és nagy Hounsfield-érték; a 2. metszet esetén nagy hézagtartalom és kis Hounsfield-érték volt megfigyelhető.

A metszeteken jól látszik, hogy a szemszerkezet a különböző metszetekben nem tér el egymástól, ez a réteg jól bedolgozottnak, egyenletesnek tekinthető. A 2. rétegben tapasztalható nagy hézagtartalom a két réteg összedolgozásakor keletkezett, amit az eltérő hőmérsékletű aszfaltok összedolgozásával tudunk magyarázni.

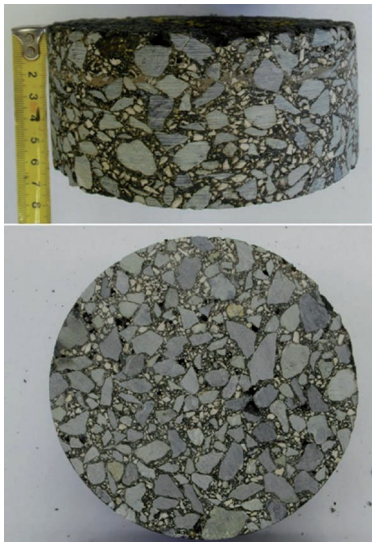

4. ábra A 2. minta kopórétegének metszete (felül: a furat magminta egy szelete; alul: a furat magminta felülnézete)

Fig. 4. A section of the 2nd sample's surface course (above: a section of the asphalt core; below: the top-view of the asphalt core)

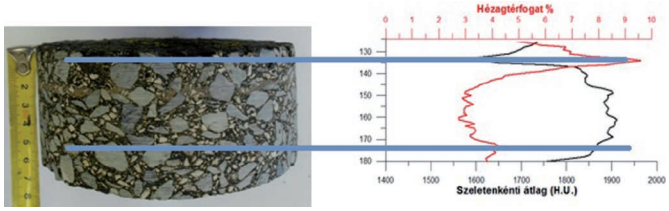

5. ábra A 2. minta kopórétegének elemzése CT-vel

Fig. 5. The CT analysis of the 2nd sample's surface course

Mivel a digitális kiértékelés során nem tudtuk kimutatni a szétosztályozódást, ezért megvizsgáltuk a minták adalékanyag és aszfalttartalom eloszlását is. Mindkét mintában közel azonos adalékanyag- és kötőanyagtartalmat állapítottunk meg. A *6.* és *7. ábrán* a bekeretezett terület a kopórétegben található adalékanyag, kötőanyag és hézagtartalom eloszlását mutatja. Megállapíthatjuk, hogy az adalékanyag tartalom 30-40%, a kötőanyag tartalom 60-70% között változott.

A *6. ábrán* a pirossal bekeretezett terület a kopórétegben található adalékanyag, kötőanyag és hézagtartalom eloszlását ábrázolja. Megállapíthatjuk, hogy az adalékanyag-tartalom kisebb, a kötőanyag-tartalom pedig nagyobb, mint a kopórétegben.

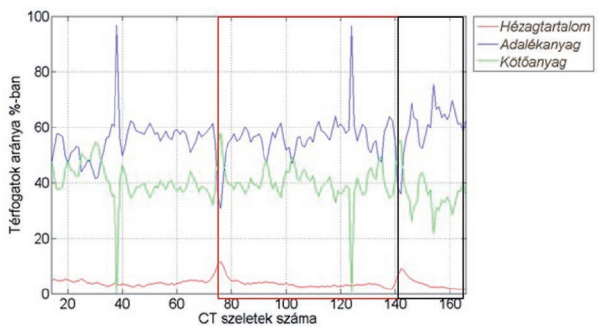

6. ábra Az 1. mintában az adalékanyag-, a hézag- és a kötőanyag-tartalom eloszlása

Fig. 6. The distribution of aggregate-, air void-, and binder content in the 1st sample

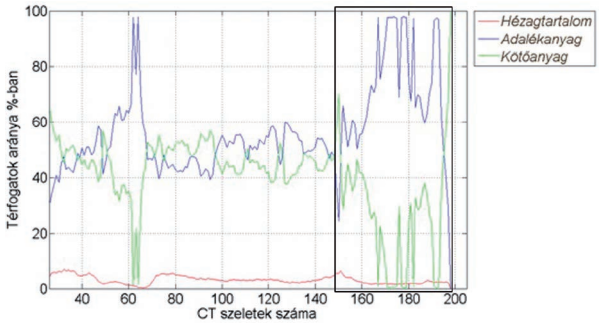

7. ábra A 2. mintában az adalékanyag-, a hézag- és a kötőanyag-tartalom eloszlása

Fig. 7. The distribution of aggregate-, air void-, and binder content in the 2nd sample

4.2 Kötőréteg

Nagyobb, 8 cm vastagságban beépített kötőréteg-aszfaltot mutat a *8. ábra*. A zúzalék eloszlása megfelelő, a réteg alján is csak kis számban figyelhető meg üreg. A fényképek érdekessége, hogy jól látható a kisebb szilárdságú zúzalékszemek törése. A törésvonal mentén szintén hézag keletkezik. Az ilyen törések miatt kialakuló hézagnövekedést, ha az a minta belsejében van, a hagyományos sűrűségmérés nem tudja kimutatni.

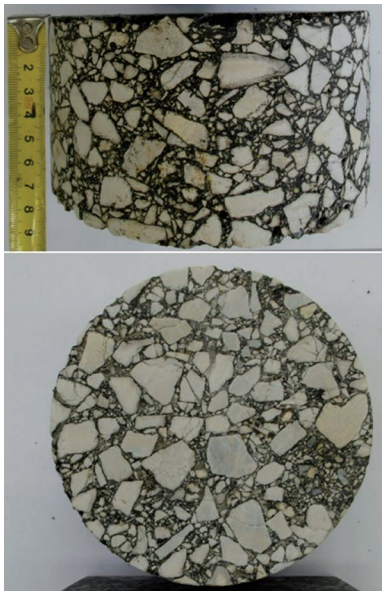

8. ábra Az 1. minta kötőrétegének metszete (felül: a furat magminta egy szelete; alul: a furat magminta felülnézete)

Fig. 8. The section of the 1st sample's binder course (above: a section of the asphalt core; below: the top-view of the asphalt core)

A *9. ábrán* megadtuk az 1. minta kötőrétegének Hounsfield-érték eloszlását és sűrűségeloszlását. A réteghatáron belül a sűrűség és a hézagtartalom eloszlása sem egyenletes. A mintán belül egy metszetet készítettünk, ahol kis hézagtartalmat és nagy Hounsfield-értéket figyeltünk meg.

A sűrűség és a Hounsfield-érték eloszlások alapján megállapítható, hogy a szemszerkezet egyenletes, ez a réteg jól bedolgozottnak, egyenletesnek tekinthető. A Hounsfield-értékek és vele egyidejűleg a sűrűségértékek eloszlásának ingadozása a berepedt adalékanyag szemcsékkel magyarázható, ami a metszeten is jól látszik.

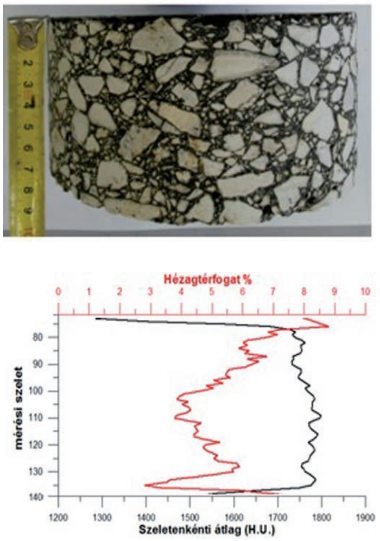

9. ábra Az 1. minta kopórétegének elemzése CT-vel

Fig. 9 The CT analysis of the 1st sample's binder course

5. Összefoglalás

Aszfaltburkolatból kifúrt magminták szemrevételezésével megállapítható több, a szállítás és beépítés körülményeit jellemző esemény. Az elvárható beépítési követelmények betartása esetén elsősorban a réteg alsó része a kritikus, mert az találkozik a fogadó réteg hidegebb felületével, az ott bekövetkező gyors lehűlés hatására a tömörítés hatékonysága csökken. A belső térbeli struktúráról valós képet kaphatunk, ha CT-felvételek háromdimenziós elemzését elvégezzük.

A CT-felvételek alapján megállapítottuk az egyik vizsgált aszfaltminta szétosztályozódását. Megállapítottuk, hogy a kopórétegben az adalékanyag-tartalom 30-40%, a kötőanyag-tartalom 60-70% között változott. Megállapítottuk továbbá, hogy a kötőrétegben az adalékanyag-tartalom kisebb, a kötőanyag-tartalom pedig nagyobb volt, mint a kopórétegben.

Másik aszfalt mintán megállapítottuk, hogy a kopóréteg alján és tetején nagyobb a hézagtartalom, amit a tömörítéssel tudunk magyarázni. A réteghatárig egyenletes sűrűség- és a hézagtartalom-eloszlást találtunk.

Hivatkozások

[1] Kisgyörgy L., Földes T., Lublóy É., Oszkó L., Ambrus D. (2013): Aszfalt próbatestek vizsgálata CT-vel, *Magyar Építőipar*, 2013. év 1. szám, pp. 14-19.

[2] Berényi, E., Bogner, P., Horváth, Gy., Repa, I. (1997): Radiológia, *Springer Hungarica*, Budapest.

[3] Ambrus Kálmán: Közlekedési Pályaszerkezetek, *"Az útpályaszerkezetek felépítési rendje, típusai. Útpályaszerkezeti alapfogalmak, élettartam, főbb tönkremeneteli jelenségek*" előadás

Ref.:
Lublóy É. – **Földes** T. – **Ambrus** D. – **Kapitány** K. – **Barsi** Á.: *Útpályaszerkezetből vett fúrt magminták szemrevételezése és értékelése CT-vel*
Építőanyag – Journal of Silicate Based and Composite Materials, Vol. 66, No. 3 (2014), 64–67. p.
http://dx.doi.org/10.14382/epitoanyag-jsbcm.2014.13

ASPHALT – THE SUSTAINABLE TRANSPORT SOLUTION

Roads are essential to our everyday lives, playing a huge role in the transport of goods and people across Europe. Asphalt surfaces offer comfort, safety and sustainability – both today and into the future.

Within the European road network there are around 6.1 million km of paved roads, linking major conurbations and tiny communities from coast to coast.
Roads are the most regularly used access routes to all parts of Europe. When it comes to inland goods and passenger transport, the figures in recent years speak for themselves showing that; over 72% of our goods and 83% of passengers travel by road, rather than rail, air or water.

Developing and maintaining a road network that provides unobstructed and safe transit in all kinds of weather is a key task; it supports the prosperity, productivity and competitiveness of our communities and commercial activities.
At the same time we need to be aware of the cost and environmental impact of road building and maintenance. ■

eurobitume

Email: info@eurobitume.eu
www.eurobitume.eu

Cement kiln dust/rice husk ash as a low temperature route for wollastonite processing

Emad M. M. EWAIS ▪ Refractory and Ceramic Materials Division(RCMD), Central Metallurgical R&D Institute, Cairo ▪ dr_ewais@hotmail.com
Yasser M. Z. AHMED ▪ Refractory and Ceramic Materials Division(RCMD), Central Metallurgical R&D Institute, Cairo
Ahmed A. M. EL-AMIR ▪ Refractory and Ceramic Materials Division(RCMD), Central Metallurgical R&D Institute, Cairo
Hamdy EL-DIDAMONY ▪ Applied Inorganic Chemistry, Chemistry Dept., Faculty of Science, Zagazig University

Received: 25. 08. 2014. ▪ Érkezett: 2014. 08. 25. ▪ http://dx.doi.org/10.14382/epitoanyag-jsbcm.2014.14

Abstract

Eco-friendly and valuable commercial wollastonite based ceramics have been obtained from the most hazardous industrial and agrowastes (Cement kiln dust and rice husk ash) by reactive crystallization-sintering. Different batch compositions from cement kiln dust (CKD) with varying amounts of rice husk ash (RHA) were wet mixed, dried, grounded and sieved. Then, all batches were uniaxially pressed and fired at different temperatures (1100-1200°C). Phase composition, microstructure, densification parameters, and mechanical properties of the obtained fired specimens were investigated. The results showed that wollastonite based ceramics were synthesized successfully at 1100°C without addition of any mineralizers. On the other hand, a considerable saving in time and heat energy were realized when an amorphous RHA silica was used instead of its other crystalline varieties. This was related to the higher reactivity of the amorphous RHA silica and its high specific surface area. The presented work made possible not only to overcome the environmental pollution ensuing from the accumulation of these industrial and agrowastes but also, to valorize and find added value to these residues. Conversion the latter into useful wollastonite-based ceramics with appropriate technology and environmental properties, allows the potential application in several fields. Hence, economic benefits will accrue to the producers and thus to the national economy.

Keywords: cement kiln dust (CKD), rice husk ash (RHA), batch composition, sintering, wollastonite, microstructure, phase composition, densification parameters, mechanical properties.

Emad Mohamed M. Ewais
earned his BSc in Chemistry (1987) as well as his MSc (1992) and PhD in Inorganic Chemistry (Ceramics) at the Faculty of Science, Cairo University, Egypt. He is a Professor and Head of the Refractory and Ceramic Materials Division (RCMD) of the Central Metallurgical R&D Institute (CMRDI) in Cairo. He is also a member of the Institute of Materials, UK, and of other national Ceramic Societies. His wide-ranging research interests include the processing of ceramics, glass ceramics, refractory cement and castables and, especially, the properties and applications of advanced materials, wastes and refractories in metallurgical processes. Dr Ewais has authored and co-authored numerous international publications and has widely lectured on an international basis.

Yasser Momtaz Z. Ahmed
earned his BSc in Chemistry (1989), his MSc (1994), and his PhD from the Faculty of Science, Ain Shams University, Cairo, Egypt. He is A Professor and Head of the advanced materials Department in the Central Metallurgical R&D Institute (CMRDI) in Cairo. His research interests include the synthesis and characterization of nanostructured ceramic materials and synthesis, as well as the characterization of porous bodies of advanced materials suitable for various applications.

Ahmed A. M. El-Amir
earned his BSc in Chemistry (1989) from the Faculty of Science, Zagazig University, Egypt. He is currently working as a research assistant at Refractory and Ceramic Materials Division in the Central Metallurgical R&D Institute (CMRDI) in Cairo.

Hamdy El-Didamony Ahmed
earned his BSc in Chemistry (1963) and his MSc (1967) at the Faculty of Science, Cairo University, Egypt. He awarded his PhD (1973) from Witterberg University. He got his DSc (1999) from Zagazig University through Royal Society of England. His research interest include cement chemistry and building materials.

1. Introduction

While natural raw materials are becoming scarce and in some cases approach exhaustion, continuous industrial activity generates increasing quantities of wastes and by-products, of which disposal is subject to ever stricter environmental legislation [1]. The expansion in housing that relevant to world population growth in turn leads to the expansion in the cement industry. The total global cement production reached 3.7 billion tons in 2012 (according to the USGS mineral program report 2013) [2]. Depending on the alkalinity and the purity of the raw materials, about 0.17-10% of the produced clinker is bypass (CKD) [3]. This dust is generally grayish in color and consists predominately of silt-sized, non-plastic particles representing a mixture of partially calcined and unreacted raw feed, clinker dust and fuel ash enriched with alkali sulfates and halides and other volatiles [4]. Egypt produces annually about 48 million tons of clinker and according to the high alkalinity of Egyptian raw materials, the amount of CKD reaches ~10% of the clinker produced [3]. Thus, about 5 million tons of CKD is generated annually as a byproduct that can spread over a large area through wind and rain, becoming accumulated in plants, animals, and soils and consequently negatively affecting the environment and human health [5]. Many trials have been made for recycling CKD in various fields. However, the efforts that have been made to recycle/reuse the CKD are still very modest compared with the problem [6]. As a result, the accumulation of CKD in landfills became a progressively significant threat to the environment.

On the other hand, the worldwide production of rice paddy exceeded 730 million tons in 2012 (EG). This paddy consists of 72% rice, 5-8% of bran and 20-22% husk on average. Thus, 730 million tones of paddy will generate about 160 million tones of husk when grinding [7-9]. Husk, also called hulls, consists of the very hard outer shell covering the rice kernel to protect it during its growth [10]. It is the largest milling by-product of the paddy. The husk contains about 75-85% organic volatile matter and ash around 15-25% by weight, depending on the plant variety, climatic conditions and geologic location [8-9]. In Egypt, during May 2012 to April 2013, it is reported that the production of rice paddy amounted to about 6.4 million tons that in turn gives 1.4 million tons of the husk when grinding. The husk in Egypt and most rice producing countries, is either dumped as waste, causing damage to the

land and the surrounding area in which it is dumped or burnt for heat generation in ambient atmosphere leaving a residue, called RHA [7]. This ash is mostly silica (87-97%) with small amounts of alkalies and other trace elements [9,11]. The silica therein is originally present in an active hydrated amorphous opaline state in the cellulose structure of rice husk [12]. Depending on time, rate and temperature of combustion and type of furnace/kiln used as well as the impurities present in the ash, the silica either remains in an amorphous phase or is transformed into its various crystalline polymorphs [12-14]. Agrowastes (like RHA) are suitable materials for a wide range of industrial and research applications due to their low or zero cost, easy availability and their potential properties including higher active silica content, high porosity and low selfweight, very high specific surface area and extremely low thermal conductivity [7,15]. Recently, many efforts have been made to valorize the value of silicon rich rice husk ash and utilize it for the manufacture of a variety of useful products [7,9,12,14,16-26]. Despite having so many well established applications, little portion of rice husk produced is utilized in a meaningful way [10]. A large percentage of available husk is fired in boilers for raising steam for parboiling of paddy. Elsewhere it is piled up in heaps in open fields and periodically set on fire or simply dumped in nearby streams or used as cattle feeding.

Wollastonite ($CaSiO_3$) is a polymorphic substance and its three forms (woolastonite-1A, wollastonite-2M, and pseudowollastonite) can be found in nature [27]. Wollastonite has received much attention due to its potential properties such as acicular (needle-like) structure, high aspect ratio, high brightness and whiteness, low shrinkage, low loss on ignition (0.5-2%), low moisture and oil absorption properties, lack of volatile constituents, high pH, low thermal expansion, low thermal coefficient, non-toxicity, biocompatibility, and largely chemical inertness. It received wide range of applications in different fields such as traditional and advanced ceramics, automobile industry, metallurgy, paints, plastics and polymers.

Generally, natural wollastonite occurs in small amounts and is highly contaminated with other minerals such as diopside, calcite, dolomite, quartz, hedenbergite and granates [27]. Thus, in recent years, many efforts have been made to utilize different mineral resources along with most of industrial wastes for wollastonite synthesis by different methods [28-36]. Conversion CKD and RHA into useful wollastonite based ceramics with appropriate technology and environmental properties, allows their potential application in many industries. Economic benefits will accrue to the producers and thus to the national economy. Recently, Ewais et al prepared wollastonite and its composites successfully using CKD as calcia source and quartz sand as a silica source at 1150 °C (present research). This work targeted the replacement of quartz sand by the agrowastes (RHA) for economical and ecological demands. This work makes it possible not only to overcome the environmental pollution ensuing from the accumulation of these industrial and agrowastes, but also, to valorize and find value added to these residues.

2. Materials and Experimental procedures

2.1. Starting materials

The materials used in these investigations were (1) By-pass cement dust (CKD) provided by the national cement company, Helwan, Egypt. Representative samples of the dust were collected weekly for a period of 2 months and were blended to offer the raw dust. (2) Rice husk ash (RHA) produced by the uncontrolled combustion of RH (from the rice mills in Cairo, Egypt) in air using a laboratory-sintering machine at CMRDI in a manner similar to the production of energy using rice husk. Before designing the batches, mineral composition, chemical, thermal and particle size distribution analyses of these starting materials were made to specify the firing regime.

2.2. Experimental procedures

2.2.1. Batch design

Different batch compositions of CKD with 30-55 m% RHA with an increment of 5 m% were designed to prepare wollastonite and its composites (*Table 1*). The batches were assigned as A_{30}, A_{35}, A_{40}, A_{45}, A_{50}, A_{55} where the index number indicates the mass percent of RHA in the batch composition and the rest represents the weight percent of CKD. To obtain homogeneous mixtures, these batches were mixed thoroughly with distilled water in planetary ball mill for 1 hour.

Batch code		A_{30}	A35	A40	A45	A50	A55
Raw materials (m%)	CKD	70	65	60	55	50	45
	RHA	30	35	40	45	50	55
C/S molar ratio		1.17	0.97	0.81	0.68	0.57	0.48

Table 1. Batch compositions
1. táblázat Keverék összetételek

The powder mixtures (dried at 100 °C for 24 hours in a controlled oven) were passed from standard screen of opening size of 36 μm, then were uniaxially die-pressed at 95 MPa to form *cylindrical shaped specimens*. The obtained specimens were dried, then sintered at 1150 °C, 1200 °C, and 1250 °C for 2 hrs. The heating rate was 5 °C/min. The mineral composition, densification parameters, microstructure, and mechanical properties of the obtained sintered specimens were investigated.

2.2.2. Testing and characterization

Particle size distribution and specific surface area of the starting materials were determined by a laser particle size analyzer Instrument (liquid mode) BT-2001 (China) and by an automated gas sorption system Quantachrome NOVA, (version 1.12, USA). In addition, chemical analyses of the starting materials were determined by Panalytical XRF (Model advanced Axios, Netherlands). Also, thermal analysis of the materials was carried out by TG-DSC NETZSCH STA 409 C/CD through which samples were heated in air from room temperature up to 1400 °C with a heating rate of 10 °C/min using α-Al_2O_3 powder as standard reference.

Mineral compositions of the raw materials and fired batches were identified by an X-ray diffractometer, model: Brukur advanced D8 Kristalloflex (Ni-filtered Cu K_α radiation; λ=1.544 Å).

The microstructure of the fired and polished speciemens was examined by backscattered electron (BSE) in the field emission scanning electron microscopy (FESEM QUANTAFEG 250) connected to an energy dispersive X-ray microanalyzer (EDX).

Densification parameters in terms of apparent porosity and bulk density of sintered materials were determined by Archimedes immersion technique in ethanol by vacuum pressure according to ASTM C 830-00, 2000. The changes in linear shrinkage values of all specimens were calculated using a caliper by determining their diameters before and after sintering.

Mechanical properties in terms of compressive strength and microhardness were determined. The compressive strength of the fired specimens was determined at a rate of 1.3 mm/min by universal testing machine (Shimadzu, UH-F 1000 KN, Japan). Microhardness of the obtained specimens have been determined at room temperature, on the polished surface considering an average of five indentations for each specimen by using Vickers indentation method to load of 100 g for 15 s by Vickers microhardness testing machine (TTSUNLIMITED, HWDM-7, Japan). Vickers hardness was computed by Eq. (1):

$$Hv=0.0018544(p/d^2) \quad (1)$$

Where p is the indentation load (N), d is the average length of the two diagonals of the indentation (mm). Hv is the Vickers hardness in units of (GPa).

3. Results and discussion

3.1. Starting raw materials

Both particle size distribution and specific surface area of the raw materials are given in *Table 2* while *Table 3* shows the chemical composition of both CKD and RHA. XRF of RHA indicates that it consists mainly of SiO_2 (79.84%) and K_2O (5.09%) with small amounts of impurities in the form of calcium, aluminum, magnesium, sodium, and iron oxides along with 1.16% SO_3 and 1.63% Cl. The XRD pattern of RHA revealed that; no peaks can be observed except those for sylvite (KCl, JCPDS# 73-0380) at d-spaces 3.14 and 2.22 *Fig. 1a*. The halo at 2θ = 15-35° is peculiar XRD characteristic of amorphous SiO_2 with silanol (Si-OH) groups [37]. Regarding the thermal behavior, TG and DSC curves (*Fig. 2a*) Show an endothermal event centered around 90 °C due to the removal of physically bound water (i.e. moisture) in the ash. In particular the weight loss associated with this reaction is about 4 m%.

The major mass loss of ~ 20%, exhibited over the temperature range of 283 °C and 600 °C, is attributed to the release of organic volatile matters and burning of combustible material (fixed carbon) present in the ash. The volatiles in the presence of oxygen undergo flamed combustion giving rise to the broad exothermic peak in DSC centered around 450 °C. The inappreciable gradual weight loss that is observed above 600 °C

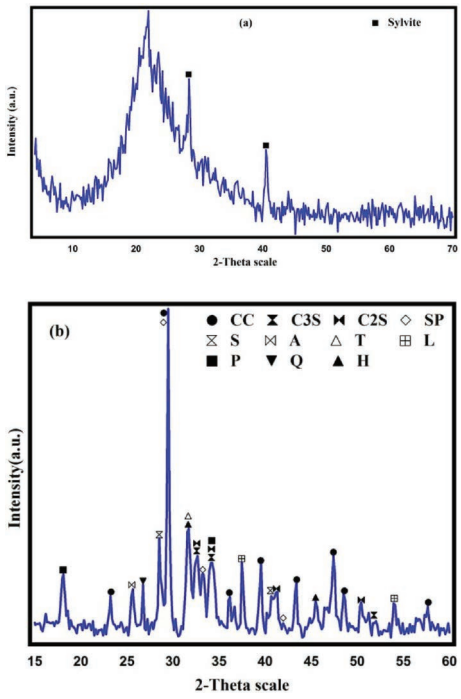

Fig. 1. XRD patterns of (a) rice husk ash RHA and (b) cement kiln dust CKD
1. ábra Röntgendiffraktogramok (a) rizshéj hamu, RHA (b) cement kemencehamu, CKD

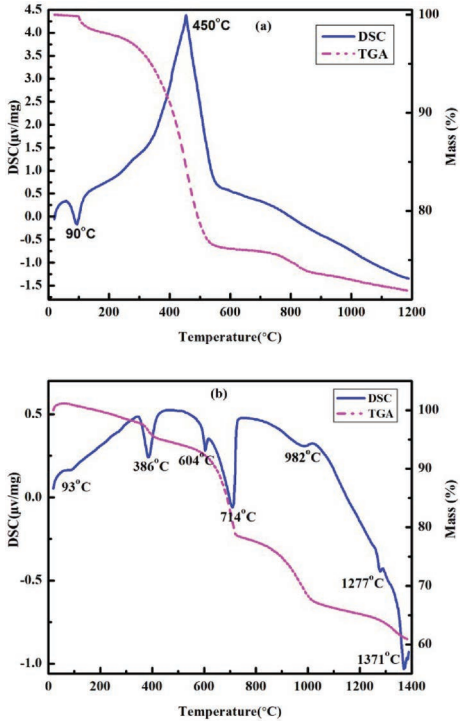

Fig. 2. TG-DSC curves of (a) rice husk ash RHA and (b) cement kiln dust CKD
2. ábra Termogravimetriai vizsgálatok eredményei (a) rizshéj hamu, RHA (b) cement kemencehamu, CKD

Raw materials	D_{10}, μm	D_{50}, μm	D_{90}, μm	Specific surface area, m^2/g
Cement kiln dust	2.419	12.84	42.64	4.541E+01
Rice husk ash	9.693	38.75	82.21	1.171E+02

Table 2. Particle size distribution and surface area of the raw materials.
2. táblázat Kiindulási anyagok szemcseméret-eloszlása és fajlagos felülete

Oxide raw material	Na_2O	MgO	Al_2O_3	SiO_2	P_2O_5	SO_3	K_2O	CaO	TiO_2	Fe_2O_3	F	Cl	L.O.I
Cement kiln dust	3.52	1.33	2.17	7.58	0.12	4.45	3.31	45.06	0.26	2.62	0.11	6.52	22.95
Rice husk ash	0.50	0.75	0.60	79.84	1.58	1.16	5.09	1.34	-	0.33	-	1.63	7.18

Table 3. Chemical analyses of the raw materials
3. táblázat Kiindulási anyagok kémiai összetétele

in the TG is ascribed to the further oxidation of carbon in the residual intermediate to form other volatile species. Also, due to the moisture release during conversion of silanol (Si-OH) group into siloxane (Si-O-Si) group in cristobalite [7]. The DSC records exhibit an exothermic reaction during the course of thermal decomposition and an endothermic peak during the removal of moisture.

CKD is a potential source of oxides. XRF of CKD showed that CaO (45.06%) is the most abundant component. Also, it contains a significant quantity of SiO_2 (7.58%) as well as other oxides such as Na_2O, MgO, Al_2O_3, SO_3, K_2O and Fe_2O_3 that could act as mineralizers and fluxes during firing of the batch compositions. XRD pattern of CKD shown in *Fig. 1a*, revealed that this dust is a very complex material consisted of more than eleven compounds. These compounds are calcite (CaCO3: JCPDS# 01-089-2340), hatrurite (Ca_3SiO_5: JCPDS# 016-0407), portlandite ($Ca(OH)_2$: JCPDS# 01-070-5492), burnt lime (CaO: JCPDS# 004-0777), anhydrite ($CaSO_4$:JCPDS# 01-072-0916), sylvite (KCl: JCPDS# 001-0786) and quartz (SiO_2: JCPDS# 005-0490), larnite (Ca_2SiO_4: JCPDS# 083-0461), halite (NaCl: JCPDS# 005-0628), spurrite ($2(Ca_2SiO_4).CaCO_3$: JCPDS# 004-0640) and ternesite ($2(Ca_2SiO_4).CaSO_4$: JCPDS# 088-0812). The actual mechanism for formation of alkali chlorides, $CaSO_4$, spurrite and sulphospurrite in the kiln is complicated; however, the following reactions and events are possible. During the clinker manufacture, the alkalis are liberated from the clay mineral lattice. They partly dissociate into the gas phase and recombine directly with chlorine or sulfur present in the charge material according to the affinities order [38]. Firstly, the chlorides are liberated during heating of the material and combustion of the fuel, combine with the alkalis forming KCl and NaCl [38]. Sometimes, chlorides are introduced as NaCl or KCl from sea water [38]. According to the priority, the remaining alkalis should react with the produced SO_3 from the oxidation of sulfur in the raw materials and the fuels burned in the kiln, forming Alk_2SO_4. However, in this case all alkalis react with the chlorides. Thus, the formed SO_3 reacts with lime or $CaCO_3$ forming $CaSO_4$ [39-40], Eq. (2). In clinkering zone, beyond 1300 °C, the formed $CaSO_4$ melts and re-decomposes giving SO_2 [40], Eq. (3). The formed elements (NaCl, KCl, SO_2) volatilize in the hot zones of the kiln and condensate at the colder areas [38]. These circulating elements form eutectic melts, which have much lower melting temperatures than the single compounds >)700 °C) [38]. All these melts, when present in sufficient quantity, generate severe encrustations and build-up formation in the preheater and the kiln inlet area [38]. These deposit buildups can lead to blocks that need to be removed, sometimes by a temporary plant shutdown [40]. Spurrite and sulphospurrite are the principal constituents of deposit buildups found in rotary kilns and kiln riser ducts. Spurrite is intensively formed in a small range of temperatures (885-912 °C), due to the accumulation of eutectic chloride melts, either: (1) by direct reaction of $CaCO_3$ and silica, or (2) by the reaction of CaO, Ca_2SiO_4 and gaseous CO_2 [41]. In addition, Increasing amounts of circulating SO_2 in the cement kiln system, promotes the formation of sulphospurrite ($2C_2S.CaSO_4$) at the same temperature range for spurrite formation [40].

$$CaO + SO_2 + 0.5O_2 \xleftrightarrow{500\text{-}1000^oC} CaSO_4 \quad (2)$$

$$CaSO_4 \xleftrightarrow{1280\text{-}1300^oC} CaO + SO_2 + 0.5O_2 \quad (3)$$

As can be seen from TG-DSC curves of CKD (*Fig. 2*), the weight loss variations over the heating range from the room temperature up to 1400 °C was 40.05%. These variations were accompanied by endothermic peaks at different temperature ranges in the following sequence; 93 °C, 386 °C, 604 °C, 714 °C, 982 °C, 1277 °C, and 1371 °C. The first mass loss recorded

Temperature range (°C)	Process	Thermal change	Chemical transformation	Weight loss
25–310	Evaporation of free and physically adsorbed water	Endothermic	$H_2O_{(l)} \longrightarrow H_2O_{(g)}$	3.22%
310–500	Dehydroxylation of portlandite	Endothermic	$Ca(OH)_2 \longrightarrow CaO + H_2O$	4.25%
500–764	Decomposition of $CaCO_3$	Endothermic	$CaCO_3 \longrightarrow CaO + CO_2$	15.24%
764–1200	Dissociation of spurrite and sublimation of alkaline chlorides	Endothermic	$2C_2S.CaCO_3 \longrightarrow 2C_2S + CaO + CO_2$ $NaCl_{(s)} + KCl_{(s)} \longrightarrow NaCl_{(g)} + KCl_{(g)}$	12.87%
1200–1380	Decomposition of both anhydrite and sulphospurrite	Endothermic	$CaSO_4 \longleftrightarrow CaO + SO_2 + 0.5O_2$ $2C_2S.CaSO_4 \longrightarrow 2C_2S + CaO + SO_2 + 0.5O_2$	4.47%
1371	Partial melting of the sample	Endothermic	$Sample(s) \longrightarrow Sample(l)$	-

Table 4. TG-DSC events occurred during firing CKD
4. táblázat Termogravimetriai jelenségek a cement kemencehamu (CKD) vizsgálata során

(3.22%) from ambient temperature to approximately 310 °C was due to the evaporation of free and physically adsorbed water as indicated by the endothermic peak centered around 93 °C in DSC curve. The second mass loss (4.25%) from 310 °C up to approximately 500 °C, can be attributed to the dehydroxylation of portlandite ($Ca(OH)_2$) [42]. This loss is accompanied by an endothermic peak centered around 386 °C in DSC curve. The further mass loss (15.24%) recorded over the temperature range of 500 °C to 764 °C was accompanied by two endothermic peaks at ~604 °C and ~714 °C. The first endothermic peak is due to the loss of CO_2 during decomposition of amorphous $CaCO_3$ or carbonates with finer crystalline structure and the second is attributed to the loss of CO_2 during decomposition of more crystalline $CaCO_3$ [42-43]. Moreover, the weight loss (12.87%) recorded in the temperature range (764 to 1200 °C) is ascribed to the dissociation of spurrite phase and sublimation of alkaline chlorides from a raw mixture. This loss is accompanied by a broad endothermic peak centered at 982 °C in DSC curve. This is compatible with published data; (1) Dissociation of spurrite occurs at a higher temperature than the $CaCO_3$ itself, inasmuch as the greater thermal stability of spurrite than $CaCO_3$ due to the substitution of the dissociable groups into the stable lattice in spurrite [39]. (2) The sublimation of alkaline chlorides begins after the thermal decomposition of calcium carbonate and finishes at 1200 °C [44-45]. With regard to the endothermic peak recorded around 1277 °C, it may be ascribed to the decomposition of both anhydrite ($CaSO_4$) [38,40] and sulphospurrite phase [39]. The latter two decompositions are accompanied by a mass loss of 4.47% in the temperature range (1200 °C to 1380 °C) [46]. As for the last endothermic peak centered at 1371 °C in the DSC curve, it is attributed to the partial melting of the sample [47]. All thermal events occurring during thermal treatment of CKD is summarized in *Table 4*.

3.2. Phase composition of the fired batches

Figs. 3, 4 and *5* show the powder XRD patterns of the fired specimens A_{30} to A_{55} in the temperature range 1100 °C to 1200 °C with 50 °C intervals. The results showed that, the crystalline phases present in these fired specimens are wollastonite-2M, cyclowollastonite, cristobalite and akermanite. At 1100 °C, the specimen A_{30} was found to contain wollastonite-2M with minor amounts of akermanite phase. On the further addition of RHA up to 40 m% in the compositions, wollastonite-2M was recorded without any other phases. Then, cristobalite appeared along with wollastonite-2M, upon addition of< 40 m% RHA in the compositions. At 1150 °C, the same situation was recorded except that the cristobalite phase is detected only in A_{55} rather than its detection in A_{45}, A_{50} and A_{55} specimens at 1200 °C. At 1200 °C, the specimen A_{30} was found to contain mainly the high temperature polymorph (cyclowollastonite) along with minor amounts of akermanite phase. However, in the remaining specimens A_{35}-A_{55}, the low temperature polymorph (wollastonite-2M) was detected as a sole phase except for the specimens A_{35} and A_{55}. Minor amounts of other phases were detected in these two specimens, cyclowollastonite in A_{35} and cristobalite in A_{55}, along with the major wollastonite-2M phase. The results obtained from the XRD patterns are summarized in

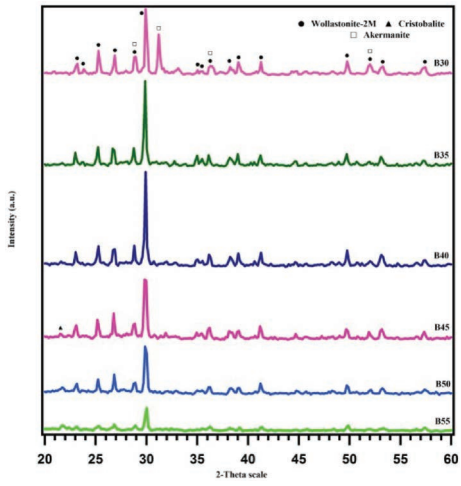

Fig. 3. XRD patterns for all composition batches sintered for 2 hrs at 1100°C
3. ábra A 2 órán át, 1100°C hőmérsékleten szinterelt keverékek röntgendiffraktogramjai

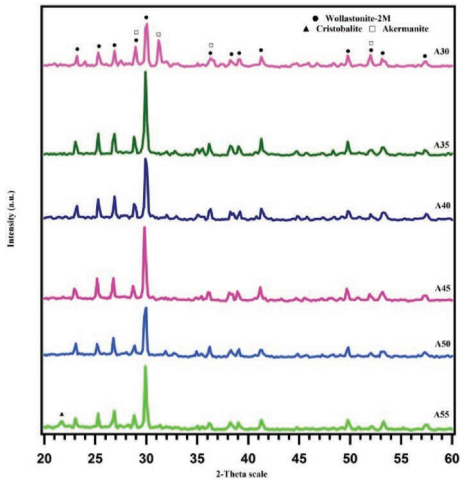

Fig. 4. XRD patterns for all composition batches sintered for 2 hrs at 1150°C
4. ábra A 2 órán át, 1150°C hőmérsékleten szinterelt keverékek röntgendiffraktogramjai

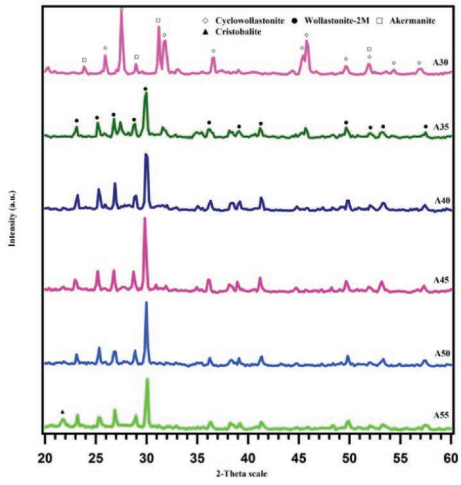

Fig. 5. XRD patterns for all composition batches sintered for 2 hrs at 1200°C
5. ábra A 2 órán át, 1200°C hőmérsékleten szinterelt keverékek röntgendiffraktogramjai

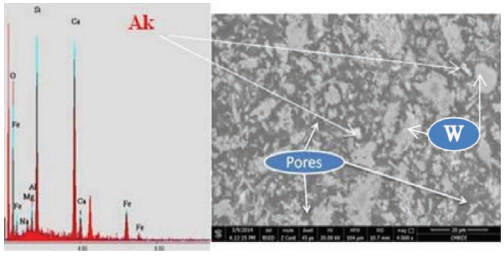

A_{30}

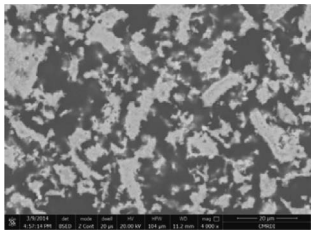

A_{35}

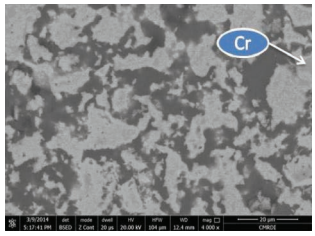

A_{40}

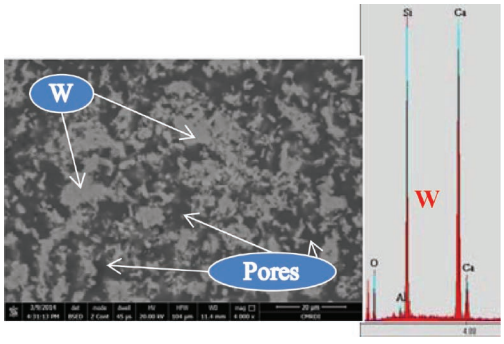

A_{45}

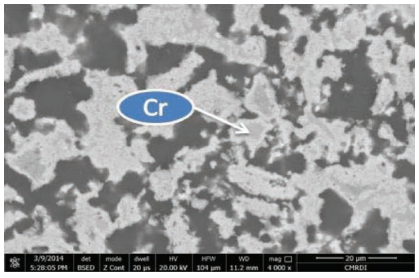

A_{50}

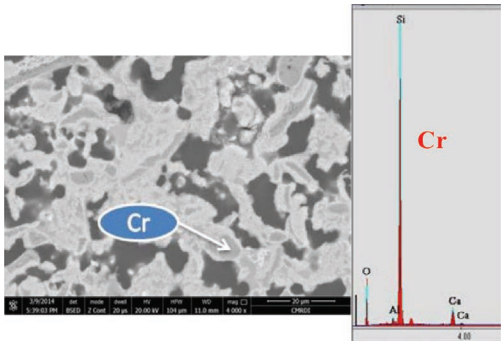

A_{55}

Fig. 6. Microstructure of all batches sintered for 2 hrs at 1100°C, Cr: cristobalite, Ak: akermanite, W: wollastonite.
6. ábra A 2 órán át, 1100°C hőmérsékleten szinterelt keverékek mikroszerkezete; Cr: krisztobalit, Ak: akermanit, W: wollastonit

Table 5. There are some phenomena could be deduced from the XRD patterns. The first phenomenon is the separation of the cristobalite phase in specimens containing high RHA content, whatever is the temperature. This is logic where at higher RHA addition, the excess stoichiometrically amount of RHAS is supposed to be dissolved in the liquid saturating it in silica. Thereafter, the remaining RHAS after complete saturation of liquid in silica was crystallized into cristobalite. From the above findings, it is clear that the transformation sequence of RHAS supports the view of Flörke [48]. According to Flörke, the silica can be transformed into cristobalite without the intermediate stage of tridymite depending on the degree of purity of starting materials. In addition, the presence of tridymite is governed by the kind and amount of impurities. The second phenomenon is the appearance of the high temperature polymorph phase (cyclowollastonite) only in the specimens sintered at 1200 °C (A_{30} and A_{35}). This can be explained in terms of the following two factors: (1) The higher alkali content (70 m% and 65 m%) and the lower quartz content (30 m% and 35 m%) found in these two specimens, compared to other specimens. (2) The high temperature (1200 °C). It is well known that silica is a network former that group to form $(SiO_4)^{4-}$ tetrahedra. These complex ions $(SiO_4)^{4-}$ join together at their vertices forming three dimensional hexagonal networks leading to increasing the viscosity of the liquid phase formed during firing. On the other hand, basic and alkaline basic oxides like CaO, MgO, Fe_2O_3, Na_2O and K_2O present in CKD are called network breakers since they can dissociate giving oxygen ions (O^{2-}) that can react with the hexagonal network of silica and destroy it. Hence, addition of basic oxides decreases the viscosity of the silica liquid phase by breaking its hexagonal network [49-50]. Also, it is well known that the viscosity of the liquid phase formed during firing decreases largely with the increase of firing temperature. Based on the aforementioned, the higher the alkali oxide content and the lower the silica content in these two specimens at higher temperature (1200 °C), the lower the viscosity of the liquid phase formed during firing of these two specimens. The existence of liquid phase of lower viscosity during firing, enhances the reaction kinetics and increases the chemical communication between the reacting phases [51]. This accelerates the diffusion of all the coexisting ions leading on heating and/or cooling to cyclowollastonite crystallization. In addition, the increase of silica content for A_{40}-A_{55} specimens at the expense of CKD leads to the decrease of the alkali amount in the compositions and this in turns leads to the increase of the viscosity of the liquid phase which hinders the diffusion of the coexisting ions during heating and/or cooling. As a result, cyclowollastonite crystallization is prevented. Therefore, the key factor that controls the formation of the cyclowollastonite is the viscosity of the formed liquid that depends on both temperature and mount of alkalis in CKD. Thus, at 1200 °C, the appearance of cyclowollastonite at lower silica content specimen A_{30} is very easy from the presence of high alkali amount and the high temperature of firing. The third phenomenon is the appearance of akermanite phase only in the specimen A_{30} whatever the firing temperature. In nature, akermanite occurs up to 1300 °C in the silica-undersaturated igneous rocks. Claude *et al* [52] also showed that, when a mixture of chalk and

silica is fired at 1150 °C, pseudowollastonite is formed together with approximately 15% by weight akermanite relative to the total product obtained, depending on the impurities present. In addition, ElBatal *et al* [53] detected previously akermanite in the fired mixture of slag and CKD. Based on this, the accompaniment of wollastonite by akermanite phase in the fired CKD-Qtz mixtures at (1100 °C to 1200 °C), is logic. With regard to, the appearance of akermanite only in the specimen A_{30} and the disappearance of its X-Ray lines completely from the specimen A_{35}, upon addition of 5 m% silica at the expense of the dust can be explained in terms of the ratio (Na+K+Mg+Ca/Al+Si) (*Table 1*). Akermanite (one member of the melilite group) is a loosely-defined mineral deficient in silica [54]. It crystallizes from silica and alumina poor, alkali-rich compositions at 700 °C [55]. Among the elements (Na, K, Ca, Mg), Na is the most important element, if not the sole influence on akermanite crystallization [55]. According to (Na+K+Mg+Ca/Al+Si) ratio, the specimen A_{30} is depleted in silica and alkali-rich while in contrast the specimens A_{35}-A_{55} are silica-rich and alkali-poor. Therefore, akermanite is formed in A_{30} due to the silica deficiency and alkali-richness of this specimen. Furthermore, the disappearance of the X-ray lines for akermanite, in the specimen A_{35} is accompanied by the increase of wollastonite. This suggests that, in the presence of excessive silica in oxidative conditions, wollastonite may form at the expense of metastable phase akermanite by its reaction with the excessive silica at higher silica content specimens through the following reversible reaction [41,56]:

melilite + silica + oxygen
⟶ wollastonite + amorphous substances

This assumption is supported by the increase of the amount of glassy phase, which can be seen in FE-SEM *Figs. 6, 7* and *8*. Also, the drastic increase of shrinkage (*Fig. 9*) observed in the temperature range 1100-1200 °C reveal the progressive formation of a melt. This is not unexpected, since the starting material (CKD) is rich in fluxing agents [57].

3.3. Microstructure of the fired batches

The backscattered FE-SEM photomicrographs of the polished surfaces of all specimens containing various CKD and RHA compositions and fired at 1100 °C, 1150 °C and 1200 °C, were shown in *Figs. 6, 7* and *8*, respectively. The general overview for all micrographs confirms the large reduction in both pore size and total porosity with the increase of firing temperature and RHA content, this is congruent with the densification behavior (section 3.4). This can be explained in terms of the enhancing in sinterability that results from the formation of more liquid phase with the increase of the two factors [13,58]. The enhancement in liquid facilitates the grain boundaries to contact on the expense of the entire porosity leading to pore closing and elimination. After complete vitrification of the specimen A_{50} (at 1150 °C) and A_{45} (1200 °C), the higher addition of RHA to these vitrified specimens led to the formation of large pores in the subsequent specimens A_{55} (at 1150 °C) and A_{50} to A_{55} (1200 °C). The reappearance of pores in such specimens can be attributed to the increase of silica content

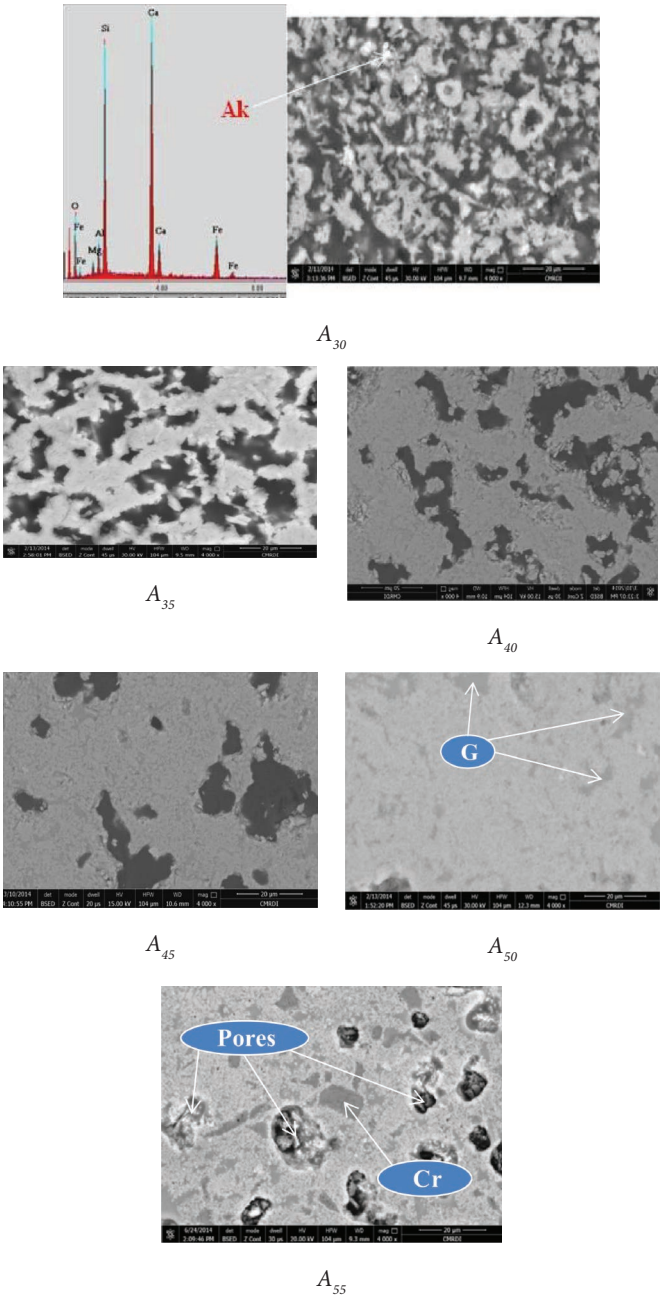

Fig. 7. Microstructure of all batches sintered for 2 hrs at 1150°C, Ak: akermanite, Cr: cristobalite, G: glass.
7. ábra A 2 órán át, 1150°C hőmérsékleten szinterelt keverékek mikroszerkezete; Cr: krisztobalit, Ak: akermanit, G: üveg

in these specimens that leads to: (1) increasing the viscosity and blocking the viscous flow by formation of silica clusters through the interlocking of SiO_4 tetrahedra [50], assuming that they pack together in an irregular way giving increasingly porous microstructure. The increase of the concentration of these clusters in the glass increases with SiO_2 content. (2) The formation of more glassy phase through which some gases can migrate into the matrix creating closed pores and bloating the specimen. Not only the pore size and total porosity are highly affected by increasing both temperature and RHA amounts, but also the pore shape is highly influenced by increasing both the two factors. As shown in micrographs, the shape of the voids in the fired specimens takes one of the following three shapes: (1) Voids are highly connected to each other, forming

a grid like cobweb, displayed by all specimens fired at 1100 °C and specimens A_{30} and A_{35} fired at 1150 °C. Such pores are difficult to be described in terms of their size and shape. (2) Irregular and highly distributed voids, having large size ranges from 2 to 40 μm, displayed by the fired specimens A_{40}, A_{45} and A_{55} (at 1150 °C) and A_{30}, A_{35}, A_{50} and A_{55} (at 1200 °C). (3) Small irregular pores, having size ranges from 0.1 to 6 μm, displayed by some of the following surface vitrified fired specimens A_{50} (at 1150 °C) and A_{40} and A_{45} (at 1200 °C). With regard to the size and shape of the formed crystals, the SEM-EDX results showed that the fired specimens at 1100 °C and 1150 °C displayed a sparse granules of wollastonite-2M of a size 0.5-12 μm, imbedded in glassy phase and distributed in a highly porous texture that is similar to the structure of bacterial colonies in a nutrient medium. The fired specimens at 1200 °C, displayed a compact flat surface of wollastonite crystals, embedded in a glassy matrix. Minor amounts of bright grains were observed along with the wollastonite in the specimen A_{30} through the investigated temperature range (1100-1200 °C). EDX of these bright spots in *Figs. 6, 7* and *8* showed that they consist mainly of Ca, Si with smaller amounts of Mg, Al, and Fe. The presence of Ca, Si as major peaks and a lesser amount of Mg suggests the presence of akermanite. These results confirm the result obtained from XRD [59]. Also, cristobalite grains sub-rounded by worm-like wollastonite-2M were seen in the fired specimens A_{45}, A_{50} and A_{55} (at 1100 °C), and A_{55} (at 1150 °C and 1200 °C). Hence, it is evident that in all the micrographs, the major phase present was the wollastonite, apart from other minor amounts of akermanite, cristobalite and glassy phases.

3.4. Densification parameters

Densification parameters – in terms of diagonal shrinkage, bulk density, and apparent porosity – of all specimens having various compositions A_{30}-A_{55} have been investigated as a function of temperature (1100-1200 °C). *Fig. 9* demonstrates that the diagonal shrinkage of the fired specimens gradually increases with the increase in the addition of RHA in the compositions as well as with the increase of the firing temperature. However, an anomaly was observed, that is, the decrease in the shrinkage at addition higher than 50 m% RHA (at 1150 °C) and 45 m% (at 1200 °C). On the other hand, the bulk density increases and porosity decreases with the increase in firing temperature and RHA content, except for the specimens A_{55} (at 1150 °C) and A_{50} to A_{55} (at 1200 °C); therein the bulk density decreases and porosity slightly increases, similarly to the shrinkage behavior (see *Fig. 10*). There are two conflicting approaches controlling the densification behavior. The first one is the decomposition and volatilization process occurring in the raw feed CKD and RHA during firing. This approach is accompanied by significant weight loss (see TG-DSC in *Fig. 2*) and contributes to the formation of more pores while the other one is the compact sinterability. The reduction in total porosity with the increase in any of the studied parameters suggests that the latter approach is more pronounced and significant [26]. The significant increase in shrinkage and bulk density (rapid densification) occurring upon the increase in RHA content in the compositions can be explained by the higher sinterability of the finer RHA particles [13] and their flabby

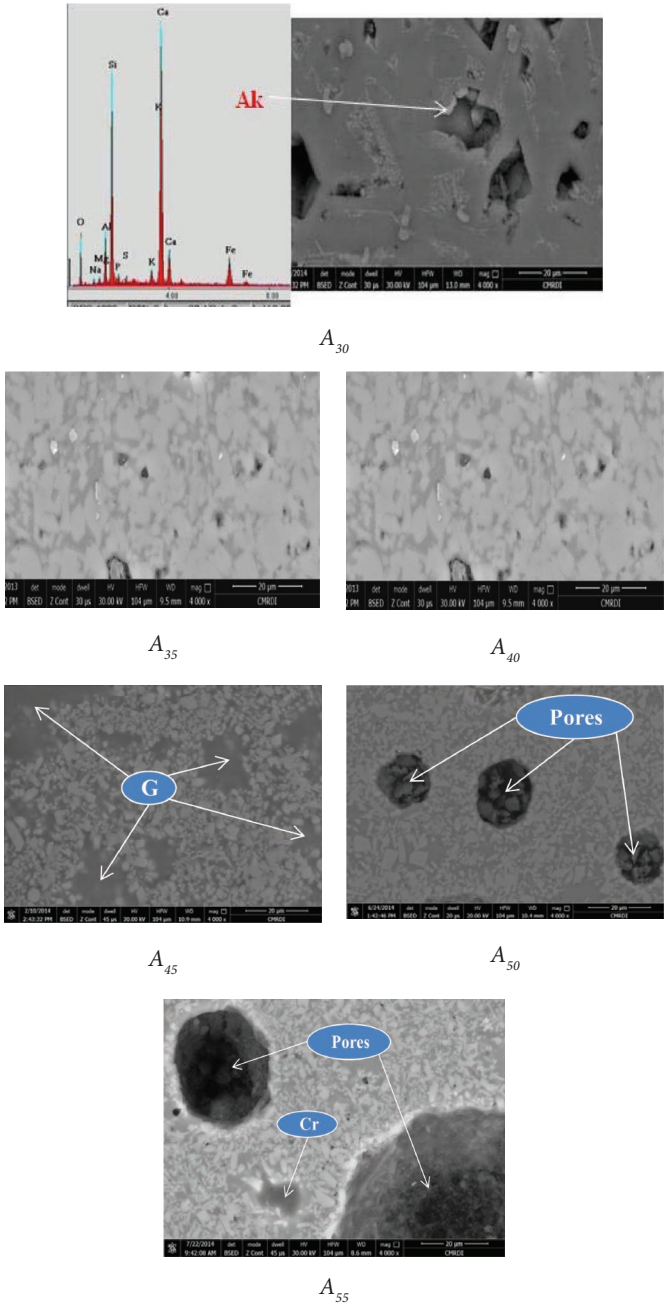

Fig. 8. Microstructure of all batches sintered for 2 hrs at 1200°C, Ak: akermanite, Cr: cristobalite, G: glass.
8. ábra A 2 órán át, 1200°C hőmérsékleten szinterelt keverékek mikroszerkezete; Cr: krisztobalit, Ak: akermanit, G: üveg

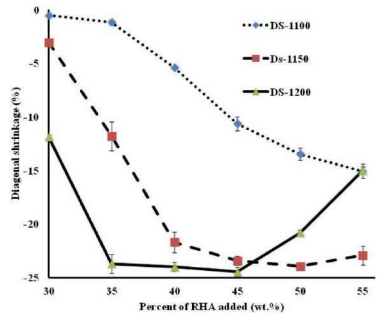

Fig. 9. Diagonal shrinkage of the cement kiln dust pellets containing variable content of RHA and fired at temperatures 1100-1200°C, (DS: diagonal shrinkage)
9. ábra A különböző RHA tartalommal cement kemenceporból 1100-1200°C hőmérsékleten szinterelt próbatestek átmérő irányú zsugorodása

nature that is responsible for the high response of specimens to heat shrinkage [9]. Furthermore, it has been reported that the amount of liquid phase that governs the degree of densification varies with the nature of additives and its amount [60]. In this context, it was found that the addition of more amorphous rice husk ash (RHA) leads to the formation of more viscous glass flow that precipitates in the voids present through the whole specimen, which results in increasing its sinterability (see *Figs. 6, 7* and *8*). On the other hand, the high content of CaO in CKD (see *Table 3*) tends to increase the binary eutectic temperature of the mixture; it prefers to react with other ingredients in the mixure, forming new ceramic phases rather than entering into glassy phase. As a consequence, the specimens containing higher contents of CKD showed higher porosity and lower mass density as well as diagonal shrinkage than those containing lower CKD contents [61]. In addition, the increase in the sintering temperature leads to formation of more liquid phase of lower viscosity that in turns leads to the increase of the sinterability [13]. The enhancement in sinterability facilitates the grain boundaries to contact on the expense of the entire porosity leading to pore closing and elimination [26]. However, what happened on decreasing the densification of the specimens at a higher addition of RHA at 1150 °C and 1200 °C indicated that the third effective parameter vigorously contributes to the sinterability. This parameter is expected to be the silica phase transformation that is noticed during XRD analysis of the fired specimens *Figs. 4* and *5*. These figures indicate that the excessive unreacted amorphous RHA in the anomalous samples is transformed into crystalline cristobalite that affects negatively the densification; crystalline phase has considerably higher viscosity than amorphous phase [13]. This can be explained to some extent by the decrease in the bulk density and the diagonal shrinkage in the specimens. Also, it has been found that the porosity of the specimens A_{55} (at 1150 °C) and A_{45} (at 1200 °C), dropped to zero and their bulk density attained maximum, 2.46 g/cm^3 and 2.45 g/cm^3, respectively. The increase in the addition of RHA in the compositions of such vitrified specimens leads to the formation of more glassy phase and in turns some gases can migrate through the matrix creating closed pores and bloating of the specimen. As a result, their bulk density and shrinkage decrease whilst their porosity increases.

3.5. Mechanical tests

3.5.1 Compressive strength

Fig. 11 shows the compressive strength for all the specimens containing various compositions A_{30} to A_{55} fired in the temperature range 1100-1200 °C. The results show that the compressive strength increases with the increase in the firing temperature and RHA content. This is congruent with the bulk density and apparent porosity results. At 1150 °C and 1200 °C, the specimen A_{45} showed the maximum strength, 177 MPa (at 1150 °C) and 353 MPa (at 1200 °C), then, the strength decreased upon the further addition of RHA in this specimen till reaching 74 MPa (at 1150 °C) and 182 MPa (at 1200 °C) for the specimen A_{55}. The increase in the strength with the sintering temperature and the RHA content can be understood in view of increase of bulk density and decrease of porosity ensuing from sintering phenomena [62] through which particle rearrangement and liquid diffusion to pores takes place. This liquid cements the well developed crystals giving a good compaction and higher compressive strength [63]. The amount of liquid should be such that it just acts as bond between the grains [60]. Too much formation of glassy phase in A_{50} and A_{55} specimens fired above 1100 °C and migration of gases therein caused internal stress and led to lowering their densification and increasing their brittleness and in turns their compressive strength is decreased [9,63].

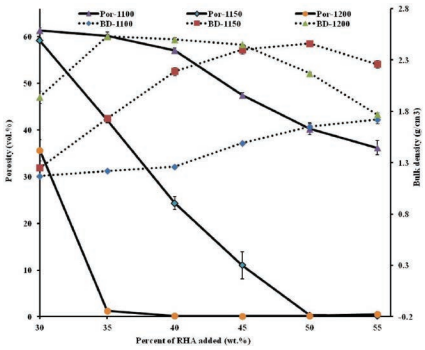

Fig. 10. Porosity and bulk density of the cement kiln dust pellets containing variable content of RHA and fired at temperatures 1100-1200°C, (BD: bulk density, por: porosity)
10. ábra A különböző RHA tartalommal cement kemenceporból 1100-1200°C hőmérsékleten szinterelt próbatestek porozitása és sűrűsége

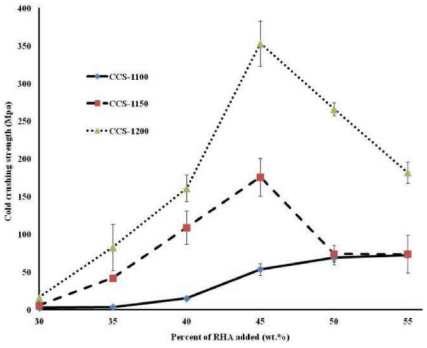

Fig. 11. Compressive strength of the cement kiln dust pellets containing variable content of RHA and fired at temperatures 1100-1200°C (CCS: Cold crushing strength)
11. ábra A különböző RHA tartalommal cement kemenceporból 1100-1200°C hőmérsékleten szinterelt próbatestek nyomószilárdsága

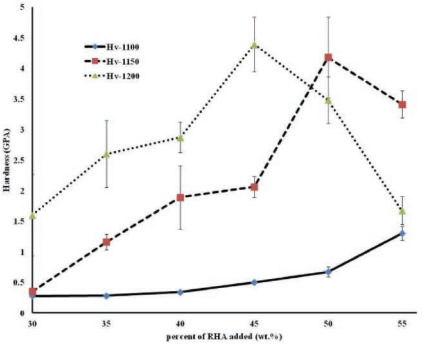

Fig. 12. Hardness of the cement kiln dust pellets containing variable content of RHA and fired at temperatures 1100-1200°C (Hv: hardness vickers)
12. ábra A különböző RHA tartalommal cement kemenceporból 1100-1200°C hőmérsékleten szinterelt próbatestek Vickers keménysége

3.5.2 Vickers micro-hardness

Vickers micro-hardness were found to increase with the increase of the firing temperature and the RHA content (see *Fig. 12*). This can be attributed to the surface vitrification and the formation of well-developed wollastonite crystals (Hv~ 4.1-5.24 GPa) as well as the increase of density and decrease of porosity relevant to the sintering process. However, there was an anomaly, that is the fall in the hardness of the specimens containing RHA more than 50 m% (at 1150 °C) and 45 m% (at 1200 °C), despite the formation of cristobalite that has higher hardness ~ 9.62 GPa in such specimens. This can be explained in terms of the surface softening [37] of such specimens due to formation of glassy phase vigorously, more than necessary, and migration of gases therein results in lowering their densification and in turns their surface hardness is decreased. Accordingly, the specimens A_{50} (at 1150 °C) and A_{45} (at 1200 °C) showed the maximum surface hardness 4.18 GPa and 4.4 GPa, respectively.

4. Concluding remarks

1. Valuable and commercial wollastonite-based ceramics have been successfully synthesized from the most dangerous industrial and agricultural wastes (CKD and RHA) through reactive crystallization sintering at lower temperature (1100-1200 °C) compared to their synthesis from the pure constituents (>1400 °C).
2. No mineralizers have been added to CKD-RHA mixes, where the impurities present in CKD and RHA acted as sinter-improving oxides that formed glassy phase and induced the early vitrification of such mixes.
3. Utilization of the amorphous active RHA in place of crystalline quartz sand resulted in:

   a) A reduction in the sintering temperature of the mixes of about 50 °C to 100 °C and this in turn gives rise to a considerable saving in time and heat energy leading to a significant economical production of wollastonite.

   b) The increase in the strength of the fired specimens due to the increase of the amount of glassy phase in case of RHA addition. This glassy phase cements the well-developed crystals giving a good compaction and higher resistance to compression.
4. The measured densification and mechanical properties of the fired specimens was found to increase with the increase in firing temperature and RHA content. However, there was an anomaly that is the fall in these properties at higher addition of RHA (50-55 m%) at 1150 °C-1200 °C. This was attributed to the formation of more glassy phase over the limit and migration of gases through this liquid creating closed pores and bloating of the specimen result in lowering their densification and mechanical properties.

Firing Temperature	Specimen code	Phases Identified	Distinguished angles			PDF card
			2°θ	2°θ	2°θ	
1100 °C	A_{30}	β-CS	2.98	3.31	3.52	75-1396
		Ak	2.85	3.07	1.75	72-2127
	A_{35}	β-CS				
	A_{40}	β-CS				
	A_{45}	β-CS, S_1				
	A_{50}	β-CS, S_1				
	A_{55}	β-CS, S_1	4.08	2.49		76-0937
1150 °C	A_{30}	β-CS, Ak				
	A_{35}	β-CS				
	A_{40}	β-CS				
	A_{45}	β-CS				
	A_{50}	β-CS				
	A_{55}	β-CS, S_1				
1200 °C	A_{30}	α-CS Ak	3.24	3.22	1.97	19-0248
	A_{35}	α-CS, β-CS				
	A_{40}	β-CS				
	A_{45}	β-CS				
	A_{50}	β-CS				
	A_{55}	β-CS , S_1				

C: CaO, S: SiO_2, (S_1: Cristobalite, β-CS: wollastonite-2M, α-CS: Cyclowollastonite), Ak, Akermanite: $(Ca_{1.53}Na_{0.51})(Mg_{0.39}Al_{0.41}Fe_{0.16})(Si_2O_7)$

Table 5. Crystalline phases identified in the fired specimens.
5. táblázat A szinterelt próbatestekben azonosított krisztallin fázisok

References

[1] Segadães, A. M.: Use of phase diagrams to guide ceramic production from wastes. *Advances in applied ceramics 2006*;105:54-46. http://dx.doi.org/10.1179/174329006X82927

[2] Savender, A.: Top 75 global cement companies. *Global Cem Magazine.*, 9 (2013). http://www.globalcement.com/pdf/eGCDec13ns.pdf

[3] Askar, Y. – Jago, P. – Mourad, M. M. – Huisingh, D.: The cement industry in Egypt: Challenges and innovative cleaner production solutions. In: *Production solutions knowledge Collaboration & Learning for Sustainable Innovation ERSCP-EMSU conference*, Delft, The Netherlands, October 25-29, 2010.

[4] El-Mahllawy, M. S.: An investigation on the effect of cement kiln dust and glauconite on the properties of acid resisting brick. *Int J Sci Tech* 2013;**2**:43-30.

[5] El-Abssawy, A. A. – Hassanien, M. A. – Ibrahim, Y. H. – Abdel Latif, N. M.: Health risk assessment of workers exposed to heavy metals in cement kiln dust (CKD). *J Am Sci* 2011;**7**:316-308.

[6] Ewais, E. M. M. – Ahmed, Y. M. Z. – El-Amir, A. A. M. – El-Didamony, H.: Cement kiln dust–quartz derived wollastonite and its composites (Under Publication).

[7] Kumar, Ajay – Mohanta, Kalyani – Kumar, Devendra – Parkash, Om: Properties and industrial applications of rice husk: A review. *International Journal of Emerging Technology and Advanced Engineering 2012*;2:2250-2259.

[8] Koteswara Rao, D. – Pranav, P. R. T. – Anusha, M.: Stabilization of Expansive Soil With Rice Husk Ash, Lime and Gypsum – An Experimental Study. *Int. J. Eng. Sci. Tech.*, 3, 8085-8076 (2011).

[9] Prasad, C. S. – Maiti, K. N. – Venugopal, R.: Effect of Rice Husk Ash in WhiteWare Compositions. *Ceram. Int.*, 27, 635-629 (2001). http://dx.doi.org/10.1016/S0272-8842(01)00010-4

[10] Gidde, M. R. – Jivani, A. P.: Waste to Wealth – Potential of Rice Husk in India, a Literature Review. *Proceedings of the international conference on cleaner technologies and environmental management PEC*, Pondicherry, India, January 4-6, 2007, pp.586-590.

[11] Rozainee, M. – Ngo, S. P. – Salema, A. A. – Tan, K. G. – Ariffin, M. – Zainura, Z. N.: Effect of fluidising velocity on the combustion of rice husk in a bench-scale fluidised bed combustor for the production of amorphous rice husk ash. *Bioresource Technology 99 (2008) 703–713*.
http://dx.doi.org/10.1016/j.biortech.2007.01.049

[12] Kapur, P. C.: Thermal Insulations From Rice Husk Ash, an Agricultural Waste. *Ceramurgia Int.,* 6, 78-75, (1980).
http://dx.doi.org/10.1016/0390-5519(80)90045-9

[13] Nayak, J. P. – Bera, J.: Effect of Sintering temperature on phase-formation behavior and mechanical properties of silica ceramics prepared from rice husk ash. *Phase Transit.*, 82, 888-879 (2009).
http://dx.doi.org/10.1080/01411590903471564

[14] Chandrasekhar, S. – Satyanarayana, K. G.– Pramada, P. N.– Raghavan, P.: Processing, properties and applications of reactive silica from rice husk-an overview, Review. *Journal of materials science 2003*;38:3159-3168.
http://dx.doi.org/10.1023/A:1025157114800

[15] Ghani, W. A. W. A. K. – Abdullah, M. S. F. – Loung, C. J. – Ho, C. J. – Matori, K. A.: Characterization of Vitrified Malaysian Agrowaste Ashes As Potential Recycling Material. *Int. J. Eng. Tech.*, 6, 72-66 (2009).

[16] Zawrah, M. F. – Zayed, M. A. – Ali, M. R. K.: Synthesis and Characterization of SiC and SiC/Si3N4 Composite Nano Powders from Waste Material. *J. Hazard. Mater.*, 227-228, 256-250 (2012).
http://dx.doi.org/10.1016/j.jhazmat.2012.05.048

[17] Niyomwas, S.: Synthesis and Characterization of Silicon-Silican Carbide Composites from Rice Husk Ash via Self-Propagating High Temperature Synthesis. *J. Met. Mat. Min.*, 19, 25-21 (2009).

[18] Pavarajarn, V. – Precharyutasin, R. – Praserthdam, P.: Synthesis of Silicon Nitride Fibers by the Carbothermal Reduction and Nitridation of Rice Husk Ash. *J. Am. Ceram. Soc.*, 93, 979-973 (2010).
http://dx.doi.org/10.1111/j.1551-2916.2009.03530.x

[19] Onojah – Amah, A. N. – Ayomanor, B. O.: Comparative Studies of Silicon from Rice Husk Ash and Natural Quartz. *Am. J. SCI. Ind. Res.,* 3, 149-146 (2012).

[20] Acharya, H. N. – Dutta, S. K.: Production of Magnesium Silicide and Silane from Rice Husk Ash. *Sol. Energ. Mater.*, 3, 445-441 (1980).
http://dx.doi.org/10.1016/0165-1633(80)90032-5

[21] Ahmed, K. – Nizami, S. S. – Raza, N. Z. – Kamaluddin, S. – Mahmood, K.: An Assessment of Rice Husk Ash Modified, Marble Sludge Loaded Natural Rubber Hybrid Composites. *J. Mater. Environ.* Sci., 4, 216-205 (2013).

[22] Chiang, K. Y. – Chou, P. H. – Hua, C. R. – Chien, K. L. – Cheeseman, C.: Lightweight Bricks Manufctured from Water Treatment Sludge and Rice Husks. *J. Hazard. Mater.*, 171, 82-76 (2009).
http://dx.doi.org/10.1016/j.jhazmat.2009.05.144

[23] Ugheoke, I. – Mamat, O. – Wahjoedi, B. A.: Optimization of Production Process Parameters of Rice Husk Silica (RHS) Refractories. *J. Aust. Ceram. Soc.*, 49, 100-92 (2013).

[24] Ismail, H. – Shamsudin, R. – Abdul Hamid, M. A. – Jalar, A.: Synthesis and Characterization of Nano-Wollastonite from Rice Husk Ash and Limestone. *Mater. Sci. forum.*, 756, 47-43 (2013)
http://dx.doi.org/10.4028/www.scientific.net/MSF.756.43

[25] Yu, Q. – Sawayama, K. – Sugita, S. – Shoya, M. – Isojima, Y.: The Reaction Between Rice Husk Ash and $Ca(OH)_2$ Solution and the Nature of Its Product. *Cem. Concr. Res.*, 29, 43-37 (1999).
http://dx.doi.org/10.1016/S0008-8846(98)00172-0

[26] Ahmed, Y. M. Z. – Ewais, E. M. – Zaki, Z. I.: Production of porous silica by the combustion of rice husk ash for tundish lining. *J Univ Sci Technol B* 15(2008) 307-313.
http://dx.doi.org/10.1016/S1005-8850(08)60058-4

[27] Khater, G. A.: Glass-Ceramics in the CaO-MgO-Al_2O_3-SiO_2 System based on Industrial Waste Materials. *J. Non-Cryst. Solids*, 356, 3070-3066 (2010).
http://dx.doi.org/10.1016/j.jnoncrysol.2010.02.030

[28] Harabi, A. – Chehlatt, S.: Preparation process of a highly resistant wollastonite bioceramics using local raw materials. *J Therm Anal Calorim* 2013;**111**:203-211.
http://dx.doi.org/10.1007/s10973-012-2242-5

[29] Nour, W. M. N. – Mostafa, A. A. – Ibrahim, D. M.: Recycled wastes as precursor for synthesizing wollastonite. *Ceram Int* 2008;**34**:105-101.
http://dx.doi.org/10.1016/j.ceramint.2006.08.019

[30] Nour, W. M. N. – Mostafa, A. A. – Koch, D. 2 Grathwohl. G.: Porous ceramics based on synthetic wollastonite. *Interceram* 2007;**56**: 428-424.

[31] Volochko, A. T. – Podbolotov, K. B. – Zhukova, A. A.: Preparation of porous ceramic materials based on wollastonite using silicon-containing components. *Refract Ind Ceram* 2011;**52**:29-24.
http://dx.doi.org/10.1007/s11148-011-9393-y

[32] Nizami, M. S.: Studies on synthesis of wollastonite from rice husk ash and limestone. *Ph.D, university of the Punjab in Pakistan*. 1993.

[33] Wang, H. – Zhang, Q. – Yang, H. – Sun, H.: Synthesis and microwave dielectric properties of $CaSiO_3$ nanopowder by the sol-gel process. *Ceram Int* 2008;**34**:1408-1405.
http://dx.doi.org/10.1016/j.ceramint.2007.05.001

[34] Pei, L. Z. – Yang, L. J. – Yang, Y. – Fan, C. G. – Yin, W. Y. – Chen, J.: A green and facile route to synthesize calcium silicate nanowires. *Mater Charact* 2010;**61**:1285-1281.
http://dx.doi.org/10.1016/j.matchar.2010.07.002

[35] Grigoryan, G. O. – Arutyunyan, G. A. – Grigoryan, K. G. – Khachatryan A. A.: Synthesis of wollastonite from the carbonate-containing gaize of Lithuania. *Theor Found Chem Eng 2010*;**44**:478-476.
http://dx.doi.org/10.1134/S0040579510040196

[36] Lin, K. – Chang, J. – Lu, J.: Synthesis of wollastonite nanowires via hydrothermal microemulsion methods. *Mater Lett* 2006;**60**:3010-3007.
http://dx.doi.org/10.1016/j.matlet.2006.02.034

[37] Kumagai, S. – Sasaki, J.: Carbon/Silica Composite Fabricated from Rice Husk by Means of Binderless Hot-Pressing. *Bioresour. Technol.*, 100, 3315-3308, (2009).

[38] Circulation phenomena in the clinkerization process, Cement seminar process technology, Holderbank.
http://222.255.19.250/Picture/PRJ-MEC/VAN/Holcim/Circulation%20Phenomena%20in%20the%20Clinkerization%20Process.pdf

[39] AbdEl-Fattah, W. I. – El-Didamony, H.: Thermal investigation on electrostatic precipitator kiln dust, *Thermochim Acta* **51**(1981) 297-306
http://dx.doi.org/10.1016/0040-6031(81)85167-2

[40] Nielsen, A. R. – Larsen, M. B. – Glarborg, P. – Johansen, K. D.: High-temperature release of SO2 from calcined cement raw materials, *Energ Fuel* **25**(2011) 2917-2926.
http://dx.doi.org/10.1021/ef2006222

[41] Glasser, F. P.: The formation and thermal stability of spurrite, $Ca_5(SiO_4)_2CO_3$, *Cem Concr Res* **3** (1973) 23-28.
http://dx.doi.org/10.1016/0008-8846(73)90058-6

[42] Huntzinger, D. N.: Carbon dioxide sequestration in cement kiln dust through mineral carbonation, *Doctor of philosophy, Michigan Technological University*, 2006.
http://services.lib.mtu.edu/etd/DISS/2006/Geological&MiningEng&Sci/huntzingerd/diss.pdf

[43] El-Didamony, H. – Amer, A. A. – Helmy, I. M. – Mostafa, K.: Durability of sulphate resisting slag blended cements and mortars in ea water. *Indian J. Eng. Mater. Sci* **3**(1996) 35-40.

[44] Klassen, V. K. – Ermolenko, E. P. – Michin, D. A. – Novosyolov, A. G.: Problem of impurity of salts of alkali metals in cement raw materials, *Middle East J Sci Res* **17**(2013) 1130-1137.
http://dx.doi.org/10.5829/idosi.mejsr.2013.17.08.7087

[45] Armatys, K. A.: Thermochemical characterisation of the gas circulation in the relevant cement industry processes, Ph.D, Clausthal university of technology in Germany. 2011.

[46] Hofman, H. O. – Mostowitsch, W. : The behavior of calcium sulfate at elevated temperatures with some fluxes, *T. Am. I. Min. Met. Eng.* **39***(* 1909) 653-628.

[47] Perraki, M. – Perraki, T. – Kolovos, K. – Tsivilis, S. – Kakali, G.: Secondary raw materials in cement industry, *J. Therm. Anal. Calorim.***70**(2002) 150-143.
http://dx.doi.org/10.1023/A:1020609801903

[48] Flörke, O. W., Ber. Dtsch. Keram. Ges. 1959;38:89.
http://nptel.ac.in/courses/113104059/lecture_pdf/Lecture%204.pdf

[49] Make, I.: Mechanism of glass formation in Portland cement clinker. *Cem Concr Res 9*(1979) 757-763.
http://dx.doi.org/10.1016/0008-8846(79)90071-1

[50] El-Mahllawy, M. S. – El-Sokkary, T. M.: Recycling of cement kiln dust and water glass sludge in the manufacture of acid resistant masonry units, *HBRC J.* **2**(2006) 35-23.
[51] Jacob, C. J.: Synthesis of wollastonite from natural materials without fusion, united states Patent, 1976.
[52] ElBatal, H. A. – Ghoneim, N. A. – Ouis, M. A.: Preparation and characterization of glass and glass-ceramics from industrial waste materials including iron slag and cement dust.
http://www.iccm-central.org/Proceedings/ICCM17proceedings/Themes/Industry/ADV%20COMP%20MATS%20IN%20CONSTRUCTION/INT%20-%20ADV%20COMP%20MATS%20IN%20CONSTR/IA1.2%20Ouis.pdf
[53] Edgar, A. D.: Chemistry, occurrence and paragenesis of feldspathoids: A review. *In: w. L. Brown, editor, Feldspars and Feldspathoids*, Canada: Springer 137(1984) 501-532.
[54] Lloyd, F. E.: Experimental melting and crystallization of glassy olivine melilitites, *Contrib Mineral Petrol* **90**(1985) 236-243.
http://dx.doi.org/10.1007/BF00378264
[55] Capitaanio, F. – Larocca, F. – Improta, S.: High-temperature rapid pyrometamorphism induced by a charcoal pit burning, *Int J Earth Sci* **93**(2004) 107-118.
http://dx.doi.org/10.1007/s00531-003-0374-3
[56] Kacim, S. – Hajjaji, M.: Firing transformations of a carbonatic clay from the high-atlas, Morocco, *Clay Miner* **38**(2003) 361-365.
http://dx.doi.org/10.1180/0009855033830102
[57] Kuo, Y. M. – Wang, J. W. – Wang, C. T. – Tsai, C. H.: Effect of water quenching and SiO_2 addition during vitrification of fly ash Part 1: On the crystalline characteristics of slags, *J Hazard Mater* **152**(2008) 994-1001.
http://dx.doi.org/10.1016/j.jhazmat.2007.07.081
[58] Rashad, A. M. – Khalil, M. H.: A preliminary study of alkali-activated slag blended with silica fume under the effect of thermal loads and thermal shock cycles, *Constr Build Mater 40*(2013) 522-532.
http://dx.doi.org/10.1016/j.conbuildmat.2012.10.014
[59] Chand, T. K. D. N. – Rohatgi, P. K.: Effect of Glass, Rice-Husk Ash and Wollastonite on Transverse Strength of Porcelain. *J. Mater. Sci. Lett.*, 6, 280-277 (1987).
http://dx.doi.org/10.1007/BF01729324
[60] Osman, R. M. – Abu-El-Naga, H. – El-Alfi, E. A.: Influence of cement dust on ceramic properties of basalt bricks, *Res J Pharm Biol Chem Sci* 4(2013) 1494-1500.
[61] Nayak, J. P. – Bera., J.: Effect of sintering temperature on mechanical behaviour and bioactivity of sol-gel synthesized bioglass-ceramics using rice husk ash as a silica source. *Appl. Surf. Sci.*, 257, 458-462(2010).
http://dx.doi.org/10.1016/j.apsusc.2010.07.011
[62] Darweesh, H. H. M. – Wahsh, M. M. S. – Negim, E. M.: Densification and thermomechanical properties of conventional ceramic composites containing two different industrial byproducts, *Am. Eurasian. J. Sci. Res.***7**(2012) 130-123.
http://dx.doi.org/10.5829/idosi.aejsr.2012.7.3.1104

Ref.:
Ewais, Emad M. M. – **Ahmed,** Yasser M. Z. – **El-Amir,** Ahmed A. M. – **El-Didamony,** Hamdy: *Cement kiln dust/rice husk ash as a low temperature route for wollastonite processing*
Építőanyag – Journal of Silicate Based and Composite Materials, Vol. 66, No. 3 (2014), 69–80. p.
http://dx.doi.org/10.14382/epitoanyag-jsbcm.2014.14

Wollastonit szintézis alacsony hőmérsékleten cement kemencehamu és rizshéj hamu felhasználásával

Veszélyes ipari hulladék (cement kemencehamu, CKD) és veszélyes mezőgazdasági hulladék (rizshéj hamu, RHA) alapanyagok felhasználásával szintetizált, környezetbarát, értékes wollastinit kerámiák tulajdonságait mutatja be a cikk. A vizsgált keverékeken a különböző CKD és RHA adagolás hatását tanulmányozhatjuk. A nedves keveréssel homogenizált, szárított, átszitált keverékek szinterezési hőmérséklete 1100-1200°C volt. A cikk bemutatja a fázisösszetételi, mikroszerkezeti, termogravimetriai, röntgendiffraktometriai és szilárdsági vizsgálatok eredményeit. Az eredmények igazolják, hogy már 1100°C hőmérsékleten is sikeresen szinterelhető wollastonit kerámia, kiegészítő adalékok nélkül is. Az eredmények rámutatnak, hogy jelentős idő és energia megtakarítás érhető el, ha az amorf struktúrájú RHA alapanyagot használják fel a kristályos szerkezetű módosulatok helyett. A kedvező viselkedés oka az amorf struktúrájú RHA nagy fajlagos felülete és jelentős reakcióképessége. A kutatási eredmények jó példát szolgáltatnak arra, hogy hogyan lehet veszélyes ipari és mezőgazdasági hulladékok felhasználásával értékes terméket előállítani. A kifejlesztett wollastonit kerámiák számos területen sikeresen felhasználhatók, jelentős gazdasági előnyt eredményezve.
Kulcsszavak: cement kemencehamu (CKD), rizshéj hamu (RHA), keverék összetétel, szinterezés, wollastonit, mikroszerkezet, fázisösszetétel, tömörödés, mechanikai jellemzők

Thermal expansion of oxide systems on the basis of ZrO_2

Vladimir V. PROMAKHOV ▪ Tomsk State University, Tomsk (Russia)
Svetlana P. BUYAKOVA ▪ Tomsk State University, Tomsk (Russia)
Vanda ILLAVSZKY ▪ University of Miskolc, Miskolc (Hungary)
Sergey N. KULKOV ▪ Tomsk State University, Tomsk (Russia) ▪ Institute of Strength Physics and Materials Science SB RAS, Tomsk (Russia) ▪ kulkov@ispms.tsc.ru
László A. GÖMZE ▪ University of Miskolc, Miskolc (Hungary) ▪ IGREX Engineering Service Ltd, Igrici (Hungary) ▪ igrex2009@yandex.ru

Received: 27. 08. 2014. ▪ Érkezett: 2014. 08. 27. ▪ http://dx.doi.org/10.14382/epitoanyag-jsbcm.2014.15

Abstract

The structure and phase composition of the ceramic-based system ZrO_2–MgO is studied. The dependence between the structural-phase state and the coefficient of thermal expansion of ceramic materials based on solid solutions ZrO_2–MgO is demonstrated. The coefficient of thermal expansion of the system increases proportionally to the increase of the MgO content. The thermal expansion of the ZrO_2–MgO ceramic materials can be described in the framework of the mixture rule taking into account the phase composition of ZrO_2 and the amount of magnesia grains in the matrtix.

Keywords: ZrO_2–MgO solid solutions, coefficient of thermal expansion, mixture rule

Vladimir V. Promakhov, PhD
has finished the Tomsk State University in 2008. He is got scientific degree ''Candidate of Technical Sciences'' at Institute of Strength Physics and Materials Science SB RAS in 2012. Theme of his Ph.D. work was "Structure and phases in ZrO_2-MgO after thermoloading and its mechanical properties" under guidance Prof. Buyakova. V.V. Promakhov is author or co- author of 10 articles and 1 Russian patent.

Prof. Svetlana P. Buyakova
Doctor of Sciences from 2008, full Professor from 2013. She is specialist in material sciencesof ceramic and ceramic matrix composites based on oxides and carbides. She is author and co-author more than 100 papers. Three Ph.D. students and one person makes they dissertations under her guidance in period 2010-2013. Now, she is chief scientist in IS PMS RAS and professor in Tomsk State University and Tomsk Polytechnic University. Her teaching experience: Introduction to Materials Science, Fundamentals of Materials Engineering, Materials and their Applications.

Vanda Illavszky
is a BSc student at the Materials Science and Engineering Faculty in University of Miskolc (Hungary) and under guidance Prof. Gömze she is participating in the research works which are made under collaboration agreement between Tomsk State University (Russia) and University of Miskolc (Hungary).

Prof. Sergey N. Kulkov
Prof. Kulkov is head of Department of Ceramics in the Institute of Strength Physics and Materials Science of the Russian Academy of Science since 1989. He has got scientific degrees „Doctor of Physics and Mathematical Sciences" in 1990. Since 1992 he's working as professor both in Tomsk State University and in Tomsk Polytechnic University. In 1997 he had a Soros Professor grant. His research works are represented in 5 books, more than 150 articles, 18 patents and many International Symposiums and Conferences. At present he is head of department „Theory of Strength and Mechanic of Solids", member of „The American Ceramic Society" of „The APMI - International" and the DYM AT Society (France).

Prof. László A. Gömze
Establisher (in July 1st, 1999) and head of Department of Ceramics and Silicate Engineering in the University of Miskolc, Hungary. Since then 7 students from the department have successfully completed their PhD theses and 4 of them were managed by Prof. Gömze. He is author or co-author of 2 patents, 5 books and more than 250 scientific papers. Recently, he is the chair of the International Organization Board of **ic-cmtp3** the 3rd International Conference on Competitive Materials and Technological Processes (2014) and **ic-rmm2**the 2nd International Conference on Rheology and Modeling of Materials (2015).

1. Introduction

Today's industrial progress leads to the need for materials that retain their functional properties when operating under high temperature conditions [1-6]. Good candidates in this respect are the oxide ceramic materials, particularly the ones on the basis of ZrO_2–MgO solid solutions. Materials of the ZrO_2–MgO system are known to have high melting temperature, chemical resistance, crack resistance and strength, which make possible their operation under high temperature conditions in aggressive media. Of particular importance in such conditions is the thermal expansion of the material. The literature provides the values of the coefficient of thermal expansion for stabilized ZrO_2 [7-10], but neither the qualitative nor the quantitative composition of the materials is considered. It is therefore pertinent to study the thermal expansion of the ZrO_2–MgO systems of variable composition.

The aim of this paper is to study the structure and phase composition and their relation to the coefficient of thermal expansion of the ZrO_2–MgO ceramic materials.

2. Experimental procedure

ZrO_2–MgO ceramics of the following compositions have been studied: ZrO_2 + 8.6 mole% MgO (hypoeutectoid); ZrO_2+13.9 mole% MgO (eutectoid); ZrO_2+25.4 mole% MgO, ZrO_2+35 mole% MgO, ZrO_2+43.3 mole% MgO (hypereutectoid).

Specimens were compacted from powders produced by thermal decomposition of salt solutions in low-temperature plasma. Powder compaction was carried out under a pressure of 70 MPa. The compacts were sintered at 1650°C and then subjected to one hour of isothermal exposure in air.

The structure of the obtained ceramics was analyzed by scanning electron microscopy on a microscope Philips SEM 515. The accelerating voltage was 30 kV. Specimens for SEM examination were mirror polished with diamond pastes of different sizes.

The phase composition and crystal structure parameters were studied by X-ray diffraction patterns obtained using filtered CuK_α radiation. The zirconia phase content was estimated by the ratio of the integral intensities of the tetragonal and cubic diffraction lines I(111), and the monoclinic diffraction lines I(111), I(–111).

Thermal expansion was measured using a mechanical dilatometer in air. The specimen temperature was increased at a rate of 10 °C/min. The specimens were heated up to 1100 °C, which, according to the phase diagram of the ZrO_2–MgO system, corresponds to the temperature of transition from the low-temperature monoclinic ZrO_2 phase to the high-temperature tetragonal modification of ZrO_2.

3. Results and discussion

The SEM images of the ZrO_2–MgO ceramics structure with different magnesia content are given in *Fig. 1*. The structure

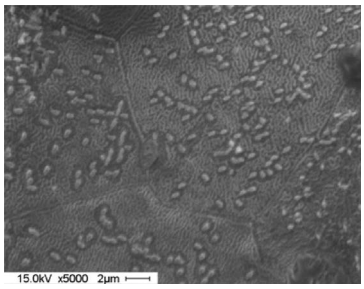

a)

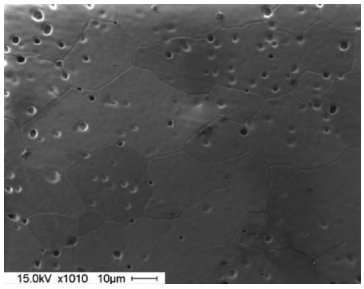

b)

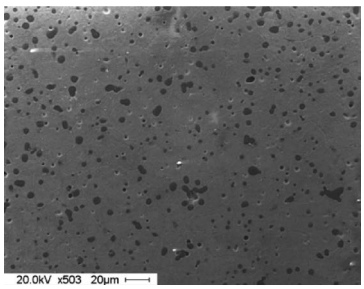

c)

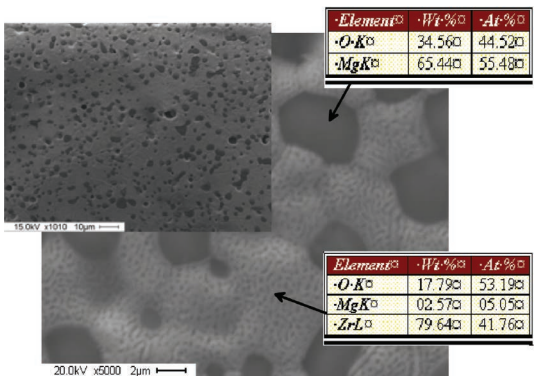

d)

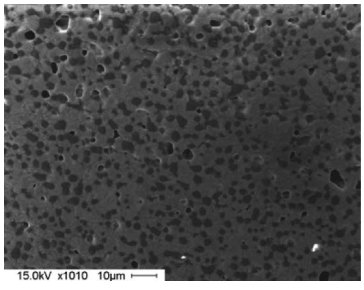

e)

a — ZrO_2 (8.6 mole% MgO), b — ZrO_2 (13.9 mole% MgO); c — ZrO_2 (25.4 mole% MgO), d — ZrO_2 (35 mole% MgO); e — ZrO_2 (43.3 mole% MgO)

Fig. 1. SEM images of the ceramics structure:
1. ábra A vizsgált cirkon-kerámiák anyagszerkezetének SEM felvételei

of the specimens of the hypoeutectoid composition shows lenticular grains of the tetragonal ZrO_2 phase, along with grains of the cubic ZrO_2 solid solution (*Fig. 1a*). The structure of the ZrO_2 (13.9 mole% MgO) ceramics is represented in *Fig. 1b*. This composition is characterized by grains of the cubic modification of ZrO_2 [11, 12]. The specimens of the hypereutectoid compositions have magnesia inclusions in the ZrO_2 matrix. In this case, the content of MgO inclusions increased from 9 to 22% with the magnesia content growth in the ZrO_2–MgO system from 25.4 to 43.3 mole%, respectively.

According to X-ray phase analysis data, the X-ray diffraction patterns of the hypoeutectoid ceramics have reflections from three zirconia phases, namely, cubic (C-ZrO_2), tetragonal (*T*-ZrO_2) and monoclinic (*M*-ZrO_2) (*Fig. 2*), with the monoclinic phase content increasing with the growing magnesia content in the initial mixture.

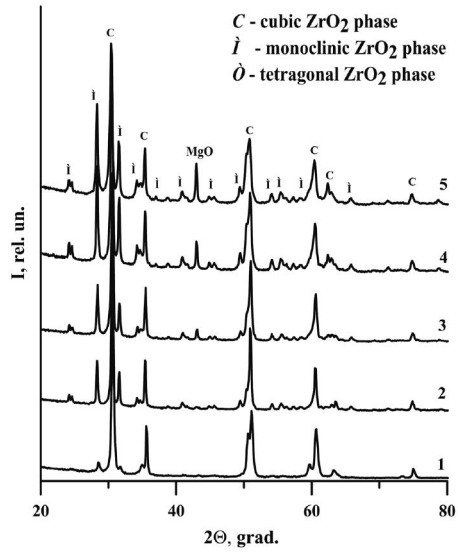

1 — ZrO_2 (8.6 mole% MgO); 2 — ZrO_2 (13.9 mole% MgO); 3 — ZrO_2 (25.4 mole% MgO); 4 — ZrO_2 (35 mole% MgO); 5 — ZrO_2 (43.3 mole% MgO).

Fig. 2. X-ray diffractograms of the ceramics of the ZrO_2–MgO system:
2. ábra A ZrO_2-MgO kerámiák röntgen-diffraktogramjai

The phase composition of the eutectoid ceramics is represented by the high-temperature cubic modification of ZrO_2. The X-ray diffraction patterns of the hypereutectoid ceramics have, along with the ZrO_2 reflections, diffraction maxima corresponding to MgO.

Measurements of the coefficient of thermal expansion of the studied materials (*Fig. 3*) showed that the coefficient of thermal expansion measured in the temperature range 400-1250 K depends linearly on the magnesia content in the initial mixture. The measured thermal expansion coefficients agree well with the values calculated by the mixture rule taking into account the phase composition of the studied materials: the content of the monoclinic ZrO_2 modification for the composition with 8.6 mole% MgO is 15%, which determines low values of the coefficient of thermal expansion equal to $6.7 \cdot 10^{-6}$ K^{-1}, since, according to the literature data, the coefficient of thermal expansion of the monoclinic ZrO_2 phase is $6 \cdot 10^{-6}$ K^{-1} and that of the cubic ZrO_2 phase is $8 \cdot 10^{-6}$ K^{-1}. The coefficient of thermal expansion of the eutectoid specimens is defined by thermal

expansion of the cubic ZrO_2 phase, while the main factor that contributes to the thermal expansion of the hypereutectoid specimens is an increase in the amount of magnesia grains in the zirconia matrix.

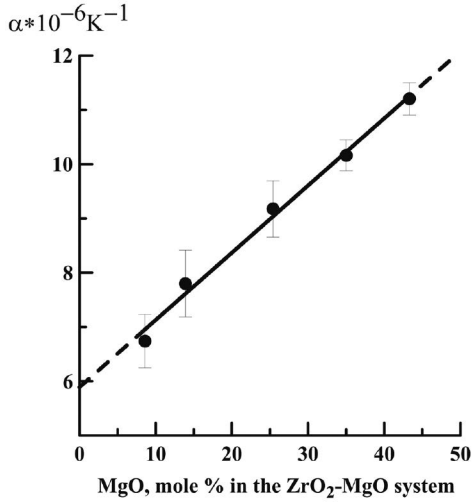

Fig. 3. Coefficient of thermal expansion vs. magnesia content in the ZrO_2–MgO system
3. ábra A ZrO_2-MgO kerámiák hőtágulási együtthatója a MgO tartalom függvényében

In extrapolating the obtained dependence to the zero MgO content, the coefficient of thermal expansion corresponds to the thermal expansion of the monoclinic ZrO_2 modification. In extrapolating the obtained dependence to the 100% magnesia content, the coefficient of thermal expansion is $14.9 \cdot 10^{-6}$ K, which is close to the thermal expansion of magnesia equal to $14.4 \cdot 10^{-6}$ K. So, the coefficient of thermal expansion of the ZrO_2–MgO system is defined by the mixture rule taking into account the phase composition and amount of magnesia inclusions in the ZrO_2 matrix.

4. Conclusions

It is found that the coefficient of thermal expansion is governed by the phase composition of the sintered ceramics, with a ratio of the fractions of the high- and low-temperature ZrO_2 modifications and the amount of magnesia grains in the ZrO_2 matrix. The coefficient of thermal expansion of the system increases proportionally to the increase of the MgO content. The thermal expansion of the ZrO_2–MgO ceramic materials can be described in the framework of the mixture rule taking into account the phase composition of ZrO_2 and the amount of magnesia grains in the matrtix.

5. Acknowledgments

Part of this work has been financially supported by Tomsk State University Competitiveness Improvement Program and RF President Grant MK-5883.2014.8.

References

[1] N. I. Ershova and I. Yu. Kelina: High-temperature wear-resistant materials based on silicon nitride, (2009) Építőanyag, vol. 61, pp. 34–37, http://dx.doi.org/10.14382/epitoanyag-jsbcm.2009.6

[2] L. A. Gömze and L. N. Gömze: Hetero-modulus nanoparticles reinforced corundum matrix CMC with extreme wear and thermal shock resistances, Mat. Sci. Forum, 2010, vol. 659, pp. 165–170, http://dx.doi.org/*10.4028/www.scientific.net/MSF.659.165*

[3] V. Lutsyk and A. Zelenaya: Crystalisation paths in SiO_2-Al_2O_3-CaO system as genotype of silicate materials, (2013) Építőanyag, vol. 65, pp. 34-38, http://dx.doi.org/10.14382/epitoanyag-jsbcm.2013.7

[4] Xiao Lei Lia at all: Study on Heat Treatment of Aluminum Nitride (Y_2O_3) Ceramics Sintered at High Pressure, (2011) Advanced Materials Research, vol. 266, pp. 68-71, http://dx.doi.org/10.4028/www.scientific.net/AMR.266.68

[5] J. Mara: Advanced ceramic materials for next-generation nuclear applications, (2011) IOP Conf. Ser. MSE, vol. 18, http://dx.doi.org/10.1088/1757-899X/18/16/162001

[6] J. Sumita, I. Fujita, T. Shibata, T. Makita, T. Takagi, E. Kunimoto, K. Sawa, W. Kim and J. Park: Study on Fracture Behavior of 2D-C/C Composite for Application to Control Rod of Very High Temperature Reactor, (2011) IOP Conf. Ser. MSE, vol. 18, http://dx.doi.org/10.1088/1757-899X/18/16/162010

[7] A.G., Evans, Perspectives on the development of high-toughness ceramics, J. Am. Ceram. Soc., 1990, vol. 73, no. 2, pp. 187–206

[8] M. Biswas, C. S. Kumbhar, and D. S. Gowtam: Characterization of Nanocrystalline Yttria-Stabilized Zirconia: An In Situ HTXRD Study, (2011) ISRN Nanotechnology, http://dx.doi.org/10.5402/2011/305687

[9] H. Schubert: Anisotropic Thermal Expansion Coefficients of Y_2O_3-Stabilized Tetragonal Zirconia, (1986) Journal of the American Ceramic Society, vol. 69, pp. 270-271

[10] J.R. Kelly and I. Denry: Stabilized zirconia as a structural ceramic: An overview, (2008) Dental Materials, vol. 24, pp. 289-298, http://dx.doi.org/10.1016/j.dental.2007.05.005

[11] Buyakova, S.P., Promakhov, V.V., and Kulkov, S.N., Thermal tests and their effect on micro- and macrostructure of nanocrystalline ZrO_2, Powder Metall. Met. Ceram., 2012, vol. 51, no. 5–6, pp. 267–272.

[12] G. Sedmale, I. Sperberga, A. Hmelov and I. Steins: Characterisation of mullite – ZrO_2 ceramics prepared by various methods, (2011) IOP Conf. Ser. MSE, vol. 18, http://dx.doi.org/10.1088/1757-899X/18/22/222014

Ref.:
Promakhov, Vladimir V. – **Buyakova,** Svetlana P. – **Illavszky,** Vanda – **Kulkov,** Sergey N. – **Gömze,** László A.: *Thermal expansion of oxide systems on the basis of ZrO_2*
Építőanyag – Journal of Silicate Based and Composite Materials, Vol. 66, No. 3 (2014), 81–83. p.
http://dx.doi.org/10.14382/epitoanyag-jsbcm.2014.15

ZrO_2 alapú kerámia rendszerek hőtágulása

Jelen munkában a szerzők a ZrO_2-MgO alapú kerámia rendszerek anyagszerkezete, fázis összetétele és a hőtágulási együttható kapcsolatát vizsgálják. Az elvégzett vizsgálatok azt igazolják, hogy az eltérő kémiai összetételű ZrO_2-MgO szilárd oldatok hőtágulási együtthatója jelentős mértékben függ az anyagszerkezeti szerkezeti fázisoktól. Ugyanakkor az adott vizsgálati hőmérsékleten a MgO tartalom növelésével arányosan növekszik a hőtágulási együttható. A kutatás eredményeként a ZrO_2-MgO kerámia rendszerhez tartozó anyagok hőtágulási együtthatója a keverék szabály figyelembevételével leírható az adott ZrO_2 fázis jelenléte és a MgO szemcsék anyag-matrtixon belüli mennyiségének függvényében.
Kulcsszavak: ZrO_2-MgO szilárd oldatok, hőtágulási együttható, keverék szabály

Eurima is the European Insulation Manufacturers Association and represents the interests of all major mineral wool producers throughout Europe.

Eurima members manufacture a wide range of mineral wool products for the thermal and acoustic insulation and fire protection of domestic and commercial buildings and industrial facilities.

Eurima was established in 1959 to promote improved standards and regulations for the use of insulation materials. More recently, it has developed to reflect the growing environmental concerns of society.

About Mineral Wool

Mineral wool insulation is unique and highly versatile product. Its exceptional thermal properties contribute hugely to European efforts to save energy and combat climate change. Additionally, the structure of mineral wool - a mat of fibres which prevents the movement of air – coupled with its long-term stability, gives it an unique ability to combat noise pollution and promote safety by reducing the risk of fire.

Mineral wool insulation is made from molten glass, stone or slag (industrial waste) that is spun into a fibre-like structure and which creates a combination of properties that no other insulation material can match. There are two types of mineral wool product: glass wool insulation and stone wool insulation.

Inorganic rock or slag are the main components (typically 98%) of stone wool. The remaining 2% organic content is generally a thermosetting resin binder (an adhesive) and a little oil. Glass wool products usually contain 95% to 96% inorganic material.

Stone wool is made from volcanic rock, typically basalt or dolomite, an increasing proportion of which is recycled material in the form of briquettes. Mineral wool made from blast furnace slag (waste) is sometimes known as slag wool.

Glass wool is made from sand or recycled glass, limestone and soda ash; the same ingredients as for familiar glass objects such as window panes or glass bottles.

Mineral wool is a high-quality insulation product for many reasons. From its responsible use of locally-sourced renewable natural resources, to its environmentally sound production process through to its diverse range of applications, mineral wool insulation is a reliable and cost-effective product. As Europe seeks to upgrade the sustainability of its building stock, mineral wool insulation is key to the creation of very low energy buildings.

eurima

European Insulation Manufacturers Association

www.eurima.org

www.mineralwool.eu

Variability case study based on in-situ rebound hardness testing of concrete

Part 1. Statistical analysis of inherent variability parameters

Adorján Borosnyói
Civil engineer (MSc), PhD, Associate Professor at BME Dept. of Construction Materials and Engineering Geology. Main fields of interest: cracking and deflection of reinforced concrete, application of non-metallic (FRP) reinforcements for concrete structures, bond in concrete, nondestructive testing of concrete, supplementary cementing materials for high performance concretes, concrete technology. Secretary of the fib Task Group 4.1 „Serviceability Models", corresponding member of RILEM Technical Committee 249-ISC „Non destructive in situ strength assessment of concrete" and Chairman of the SZTE Concrete Division.

Adorján BOROSNYÓI ▪ Assoc. Prof., BME, Dept. of Construction Materials and Engineering Geology ▪ borosnyoi.adorjan@epito.bme.hu

Received: 28. 08. 2014. ▪ Érkezett: 2014. 08. 28. ▪ http://dx.doi.org/10.14382/epitoanyag-jsbcm.2014.16

Abstract

Statistical analysis has been performed on rebound index data collected in-situ at the bottom surface of a concrete floor over 130 m^2 of testing area. Different measures of inherent variability were calculated. Correlations between inherent variability measures were studied. It has been shown that skewed distributions can be fit with the best goodness of fit for the vast majority of the local statistical parameters studied. Application of the Peirce's criterion filtering was demonstrated. Inferior local normality of the distribution of rebound index was found for the in-situ rebound hardness test results.

Keywords: Structural concrete; Nondestructive testing (NDT); Hardness; Rebound index; Inherent variability

1. Introduction

Numerous non-destructive testing (NDT) methods are available to estimate the strength of structural concrete [1-6]. Surface hardness testing is a long established NDT method for concrete structures [7,8]. Nowadays, the rebound hammer is the surface hardness testing device for concrete of the most widespread use [9-11].

Structural concrete is a multiple-level heterogeneous composite material [12,13]. On a macro-level, its heterogeneity is derived from concrete construction practice, i.e. random differences of compaction and curing at different locations, possible non-uniform supply of material and structural effects (reinforcement, changes in dimension or shape, connecting structural elements). On a meso-level, its heterogeneity is derived from concrete composition, i.e. type and grading of coarse aggregate and the paste content of fresh concrete. On a micro-level, its heterogeneity is derived from hydration performance that is governed by the type, particle size, hydraulic activity and amount of cement as well as that of supplementary cementing materials, the w/c-ratio, the type and amount of admixtures and curing compounds and the method and effectiveness of curing. On a nano-level, its heterogeneity is derived from the petrographic/chemical characteristics of fine aggregate and that of non-hydraulic supplementary materials and the molecular structure of hydrated cement paste.

This multiple-level heterogeneity results both *inherent* (local) variability and *spatial* (regional) variability of the performance properties. Local variability can be analysed by conventional mathematical statistical methods. Analysis of regional variability needs spatial models – that are typically used in geostatistics.

2. Scope of the studies

The present series of papers introduces path finding, comparative statistical analyses for the inherent variability and the spatial variability parameters calculated for in-situ rebound hammer tests performed on structural concrete.

In the first part, inherent variability parameters are analysed corresponding to the independent test areas in terms of statistical *location* parameters (mean, median, mode), statistical *variance* parameters (standard deviation, coefficient of variation), statistical *dispersion* parameters (range, relative range, studentized range) and *normality* parameters (skewness, excess kurtosis, W-statistic by Shapiro and Wilk, extreme studentized deviate by Peirce's criterion).

Aim of the present studies is to demonstrate the statistical performance of rebound hardness for in-situ testing of concrete and to add to the better understanding of sampling and modelling by rebound hardness testing.

3. Experimental

The bottom surface of the top concrete slab of a framed, monolithic, subsoil concrete tunnel was studied, with dimensions of 25.0 m × 7.5 m and a thickness of 0.48 m [14]. The measuring region on the bottom surface was 22.0 m × 6.0 m. A total number of 42 test areas were selected for Schmidt rebound hammer testing. N-type original Schmidt rebound hammer was used. Eleven individual rebound index readings were recorded at each test area. The measurements were performed by the same operator.

4. Robustness of data for test areas

Random occurrence of outliers is expected in the test area recordings of in-situ rebound hammer tests due to the uneven surface texture and local, near-surface heterogeneity of structural concrete. If the operator uses mechanical rebound hammer for the measurements (as was the case for the present studies), any common rule of thumb may be applied for the immediate rejection of extreme outlier values from the data recorded. The filtering may be automatic or can be carried out during data analysis for rebound hammers recording digitally. Technical literature does not confirm, but as well, does not reject the hypothesis of normality for the probability distribution of individual rebound index readings

for a test area. Therefore, it may be reasonable to select and run an appropriate extreme studentized deviate (ESD) test for normality to identify any (single or multiple) outlier in the data set of test areas [15]. Peirce's criterion is a rigorous method based on probability theory that can be used to identify outliers in a sample. Details of the method are given in [16]. By Peirce's criterion the maximum deviation from the mean is calculated and compared with tabulated values. The process is relatively simple and can be converted easily into an algorithm. If the maximum deviation of interest is greater than the tabulated value, then the suspicious value is removed as outlier. If no observation exceeds the tabulated value, then it cannot be claimed that there is a statistical outlier. The method assumes normal probability distribution of the data.

The extreme studentized deviate test by Peirce's criterion was run for the 42 independent test areas. It resulted that at 11 test areas a total number of 14 individual rebound index readings can be considered as statistical outlier. It means 3% of the total number of 462 individual rebound index readings. It can be concluded that the data set is robust enough and the recording of the rebound indices by the operator was effective in rejecting the extreme outliers.

5. Normality of data for test areas

The overall empirical frequency histogram of the individual rebound indices (no separation by location) is indicated in *Fig. 1* together with the best goodness of fit Fisher-Tippett (Generalized extreme value, GEV) probability density function. Considering the rebound hammer test, it can be assumed that the rebound index reading sets of separate test areas are independent and identically distributed (i.i.d.) random variables since it can be supposed that the probability distribution of the rebound index does not change by location within the same structure and the separate test areas can be considered to be mutually independent [17]. Based on these assumptions, the central limit theorem applies for the rebound hammer test; i.e. the probability distribution of the resultant of the rebound index reading sets of separate test areas (each with finite mean and finite variance) approaches the normal distribution if sufficiently large number of the i.i.d. random variables is available. *Fig. 1* also indicates fitted normal distribution for comparison. It can be realised by a simple visual inspection that the resultant of the 42 independent test areas apparently approaches rather well to the normal distribution. For the 462 individual rebound indices, the global mean value is 52.6, the global median value is 53, the global mode value is 53, the global skewness is 0.11 and the global excess kurtosis is –0.11. It should be noted, however, that the statistical goodness of fit for the normal distribution is fairly less than that of the Fisher-Tippett (Generalized extreme value, GEV) distribution. It was shown by Kolmogorov-Smirnov, Anderson-Darling and Chi-Squared goodness of fit tests that at least twenty different types of probability distributions (e.g. Pearson V, Gamma, Beta, Lognormal, Fréchet and even uniform distributions) provide *better* goodness of fit than the normal distribution, apart from the overall best fit Fisher-Tippett distribution. Therefore, it can not be concluded that statistically the normal probability distribution applies for the present population of rebound index readings. From an engineering point of view, however, the normal probability seems to be suitable as a rough estimate.

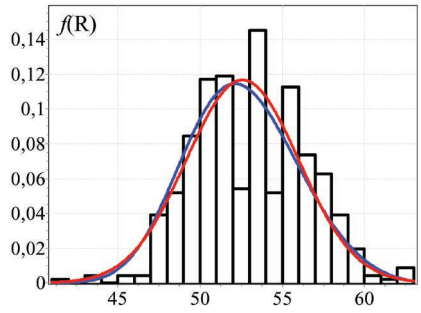

Fig. 1. Frequency histogram together with the best goodness of fit Fisher-Tippett (Generalized extreme value, GEV) probability density function (blue curve) for the individual rebound indices (no separation by location, n = 462); normal distribution is also indicated for comparison (red curve), after [14]

1. ábra Gyakorisági hisztogram és a legjobban illeszkedő Fisher-Tippett eloszlás sűrűségfüggvénye (kék színű görbe) az összes mérési helyen rögzített visszapattanási értékre vonatkozóan (n = 462); a normális eloszlás sűrűségfüggvénye [14] alapján piros színű görbével megjelenítve

If the 42 independent test areas are analysed separately then a suitable normality test can be selected and run to check the extent of deviation from normality. The normality tests are used in statistics to study if a data set has normal distribution or not. The 11-bin frequency histograms corresponding to the 42 independent test areas are indicated in *Fig. 2*. On a simple visual inspection it can be postulated that the normality of the observations is expected to be weak. Majority of the observations suggest platykurtic, almost uniform distribution.

There are about 40 normality tests available in the technical literature [18], however, the most common normality test procedures of statistical analyses are the Shapiro-Wilk test, the Kolmogorov-Smirnov test, the Anderson-Darling test and the Lilliefors test. It is demonstrated in the technical literature [19] that the Shapiro-Wilk test is the most powerful normality test from the above four, therefore, the Shapiro-Wilk normality test was run for the present analysis. Details of the method can be found in [20,21].

According to the null hypothesis of the Shapiro-Wilk normality test, the population has normal probability distribution. The calculation of the so called W-statistic by the method results the probability (p-value) that corresponds to the null hypothesis and one can see at which significance level the assumption that the population has normal probability distribution can be accepted. If the p-value is smaller than a preliminarily chosen significance level, then the null hypothesis is rejected; otherwise the null hypothesis is accepted at the chosen significance level.

It was realized during the present study that the hypothesis of normality can be generally accepted at a *very low* significance level for the 42 independent test areas analysed separately. The mean for the p-value is 40.0%. The p-value is smaller than 60.5% for 75% of the test areas. The p-value is smaller than 76.2% for 95% of the test areas. The p-value is smaller than 85.0% for 99% of the test areas. The maximum p-value is found to be 90.2%. Frequency histograms for the p-value and the W-statistic are shown in *Fig. 3*.

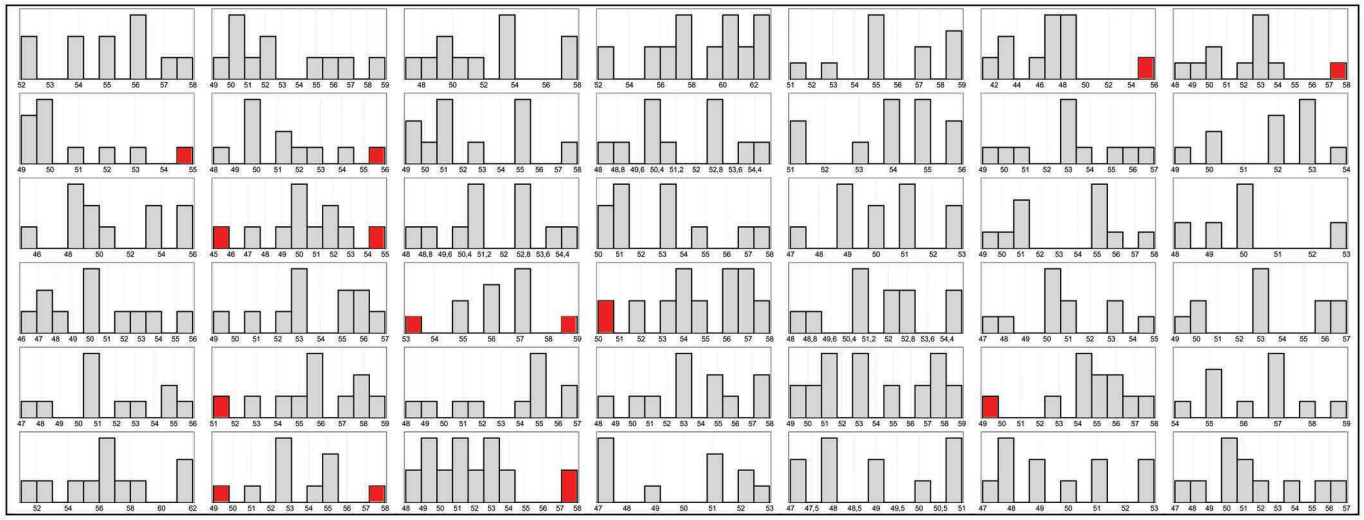

Fig. 2. 11-bin frequency histograms for the individual rebound index readings corresponding to the 42 independent test areas (red colour markings indicate the suspected outliers by Peirce's criterion)
2. ábra Egyedi visszapattanási értékek gyakorisági hisztogramjai 11 osztásközzel, a megvizsgált 42 mérési helyre vonatkozóan (a Peirce kritérium alapján adódó kiugró értékek piros színnel jelölve)

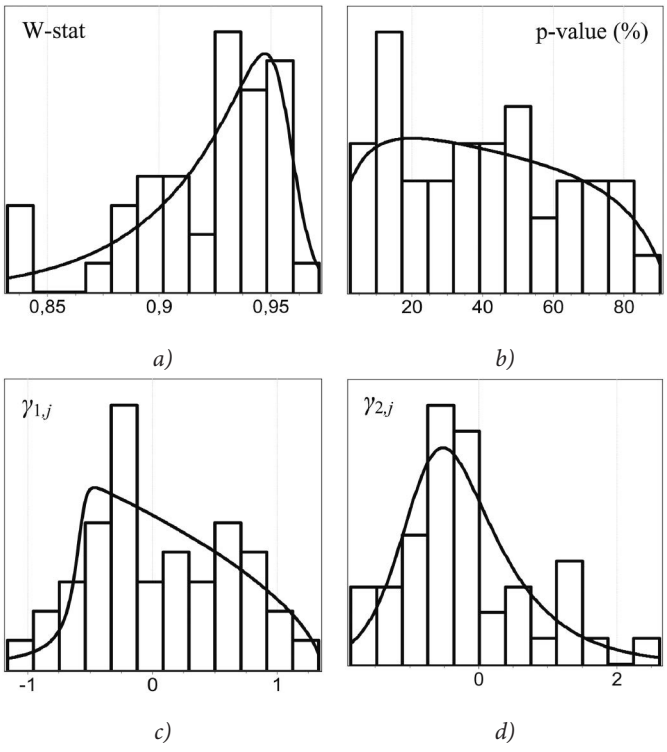

Fig. 3. Statistical analysis of the normality parameters
a) W-statistic for test areas b) p-value (%) for test areas
c) skewness ($\gamma_{1,j}$) for test areas d) excess kurtosis ($\gamma_{2,j}$) for test areas
3. ábra Normalitási paraméterek statisztikai vizsgálata
a) W-statisztika hisztogramja b) p-érték (%) hisztogramja
c) ferdeség ($\gamma_{1,j}$) hisztogramja d) csúcsosság ($\gamma_{2,j}$) hisztogramja

Further statistical information is obtained from the calculation of the skewness and excess kurtosis. Frequency histograms are shown in *Fig. 3*. The mean for the skewness is 0.068 that would not indicate pronounced deviation from normality on its own, however, a definite bimodality is visible on the frequency histogram that needs further considerations. An apparent mode at about –0.4 and at about 0.5 is seen. The sum of the 42 individual skewness values may indicate, if any, positive or negative skewness tendencies. The sum is 2.87 that reveals a stronger positive skewness tendency. The mean for the excess kurtosis is –0.19, but the median is more meaningful for the presented positively skewed frequency histogram, being –0.38. The sum of the 42 individual excess kurtosis values is –8.28. The findings confirm that platykurtic distribution governs the observations.

It may be assumed that removal of the 14 statistical outlier individual rebound index values that were determined with the extreme studentized deviate test by Peirce's criterion would help reducing the deviation from normality. Therefore, skewness and excess kurtosis values were calculated for the 42 independent test areas after the removal of the suspected outliers (indicated in red colour in *Fig. 2*). The removal resulted improvement in skewness performance: the mean is shifted closer to zero, to the value of 0.006 and the sum of the skewness values is reduced to 0.272. Surprisingly, the excess kurtosis performance became worse: the mean is shifted farer from zero, to the value of –0.59 and the sum of the excess kurtosis values is increased to –25.01.

6. Statistical location parameters at test areas

The mean, the median and the mode values were calculated for the 42 independent test areas and were published earlier [14]. Rather close correlation of the mean, median and mode values can be supposed for the present observations. The influence of the removal of the 14 outlier individual rebound indices selected by Peirce's criterion was also tested during the present analyses. It was realized that the application of Peirce's criterion does not result considerable change in the frequency histograms of the mean, median or mode values.

7. Statistical variance parameters at test areas

The standard deviation and the coefficient of variation values were calculated for the 42 independent test areas. Frequency histograms are shown in *Fig. 4* together with the best goodness of fit Fisher-Tippett (Generalized extreme value, GEV) probability

density functions. Positive skewness is observable for both parameters, in accordance with literature data [17]. The influence of the removal of the 14 outlier individual rebound indices selected by Peirce's criterion was again tested. Outlier removal was resulted in considerable loss in the peakedness of both histograms, becoming more uniform, however, the mean of the two statistical variance parameters did not change considerably.

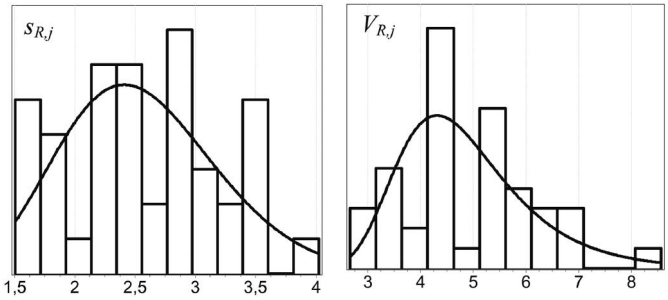

Fig. 4. Statistical analysis of the statistical variance parameters
a) standard deviation ($s_{R,j}$) for test areas
b) coefficient of variation ($V_{R,j}$) for test areas
4. ábra Variancia paraméterek statisztikai vizsgálata
a) szórás ($s_{R,j}$) hisztogramja
b) relatív szórás ($V_{R,j}$) hisztogramja

8. Statistical dispersion parameters at test areas

The range, the relative range and the studentized range values were calculated for the 42 independent test areas. Frequency histograms are shown in *Fig. 5* together with the best goodness of fit probability density functions. Best goodness of fit of Dagum distribution was found for the range values and Wakeby distribution for the relative range and the studentized range values. The observed positive skewness in the distribution of the range values is in accordance with literature data [17]. The influence of the removal of the 14 outlier individual rebound indices selected by Peirce's criterion was also tested. Outlier removal was resulted in a shift toward smaller values of the mean for the range, the relative range and the studentized range and the skewness and peakedness of the frequency histograms have been changed as well. It seems that the extreme studentized deviate test by Peirce's criterion has the strongest influence on the statistical dispersion parameters, as it was expected.

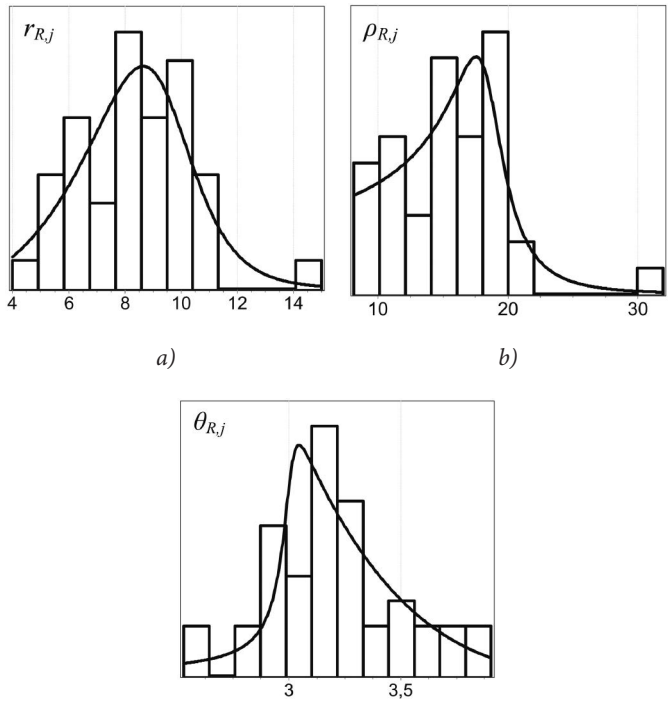

Fig. 5. Statistical analysis of the statistical dispersion parameters
a) range ($r_{R,j}$)for test areas b) relative range ($\rho_{R,j}$) for test areas
c) studentized range ($\theta_{R,j}$) for test areas
5. ábra Terjedelem paraméterek statisztikai vizsgálata
a) terjedelem ($r_{R,j}$) hisztogramja b) relatív terjedelem ($\rho_{R,j}$) hisztogramja
c) studentizált terjedelem ($\theta_{R,j}$) hisztogramja

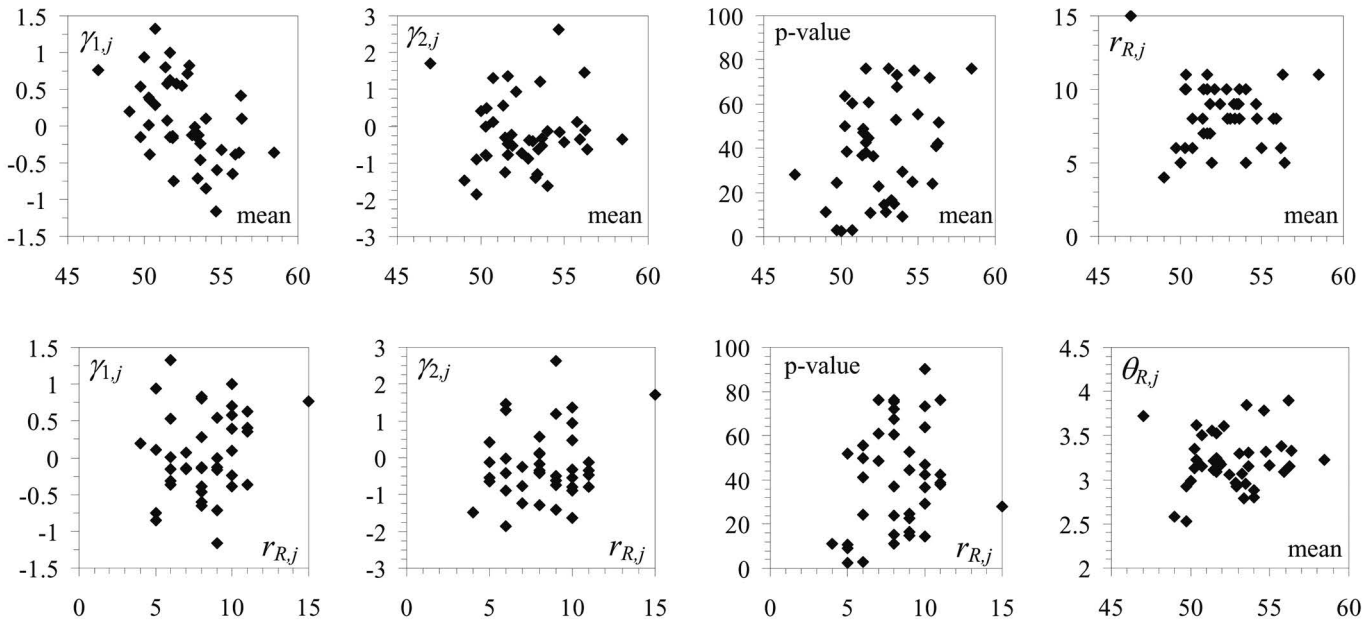

Fig. 6. Correlations between the mean, the range and the normality parameters
6. ábra Várhatóérték, terjedelem és normalitási paraméterek korrelációi

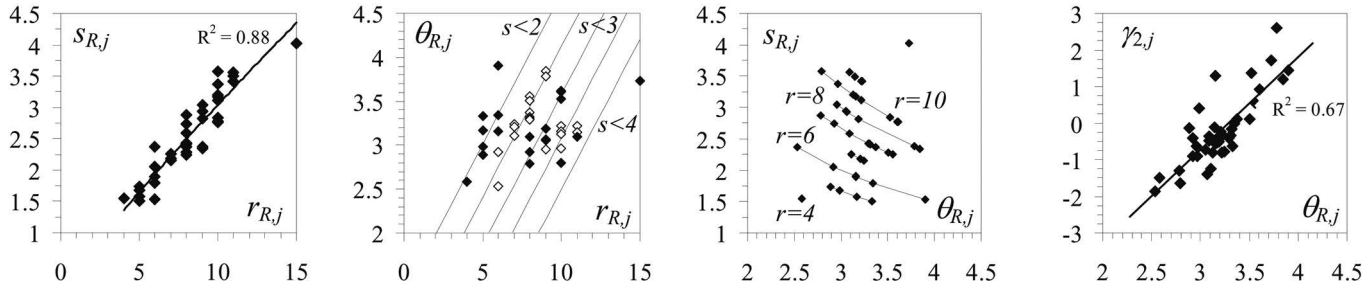

Fig. 7. Correlations between the range, the studentized range and the standard deviation; and correlation between the studentized range and the excess kurtosis
7. ábra Terjedelem, studentizált terjedelem és szórás korrelációi; valamint a studentizált terjedelem és a csúcsosság korrelációja

9. Discussion

The strength estimation of concrete by rebound hammer testing usually applies empirical relationships between statistical location parameters (mostly the mean and the median) and the compressive strength. It can be realized that the three statistical location parameters are interrelated and a rather strong correlation is found between the mean and median values for the concrete floor in the present study [14]. Frequency histograms for the mean and median values are rather similar and can be modelled by the same type of probability distribution. The mode values, however, indicate weaker correlation with the other two statistical location parameters and the peakedness of the corresponding frequency histogram is more pronounced [14].

Frequency histograms of statistical location parameters and statistical distribution parameters were found to be well fit by the Wakeby distribution for the concrete floor in the present study. Wakeby distribution is typically used for flood frequency analysis and for other extreme events in hydrology [22]. Wakeby distribution has five parameters, therefore, it can mimic the shapes of many commonly used skewed distributions. Wakeby distribution is very flexible; this is the reason why it can be well fit to observed rainfall data, or flood peaks and other extreme events in hydrology [23].

Control parameters for the data of test areas can be the range and the standard deviation according to ASTM C805 International Standard [24].

It can be realized for the present study that no correlation is found between the statistical location parameters and the statistical dispersion parameters (mean vs. range and mean vs. studentized range is indicated in *Fig. 6*). It can be also seen that no correlation is found between the statistical location parameters and normality parameters as well as no correlation is found between the statistical dispersion parameters and normality parameters (particular plots are indicated in *Fig. 6*). Normality parameters (p-value, skewness, excess kurtosis) show no correlation with each other either.

It can be realized by studying the correlation (*Fig. 7*) between the statistical dispersion parameters and the statistical variance parameters that the range and the standard deviation are interrelated and a rather strong correlation is found between them for the concrete floor in the present study. Frequency histograms also confirm the observation. Studentized range – by definition – is determined by the ratio of the range and the standard deviation, therefore, the isoquant range and isoquant standard deviation responses are clearly visible in the studentized range vs. standard deviation and the range vs. studentized range representations, respectively (*Fig. 7*). It can be also demonstrated for the concrete floor in the present study that the studentized range indicates a value that is connected to the peakedness of the frequency histogram of rebound indices at the test areas; a visible, rather good correlation is demonstrated between studentized range and excess kurtosis (*Fig. 7*).

The statistical variance parameters determine each other by their nature (*Fig. 4*) and are expected to show positive skewness in their probability distributions according to the technical literature [17] that is visible in the frequency histograms (*Fig. 4*). The mean values for the recorded rebound indices are found to be relatively high. A comparison with literature data for the recorded mean rebound index vs. standard deviation as well as mean rebound index vs. coefficient of variation responses corresponding to the test areas is shown in *Fig. 8*.

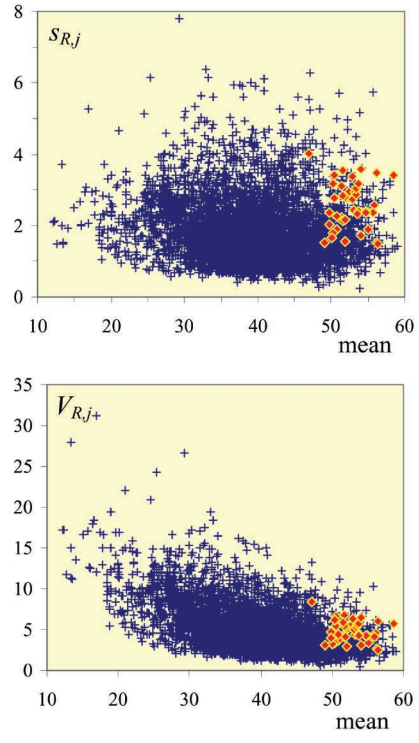

Fig. 8. Representation of the statistical variance parameters over the mean in comparison with literature data [17]; results for the present studies are indicated in red colour
8. ábra A szórás és a relatív szórás kapcsolata a várhatóértékkel [17] alapján; a jelen vizsgálati eredmények piros színnel jelölve

10. Conclusions

Inherent variability analyses were carried out on in-situ rebound hammer test results collected at the bottom surface of a concrete floor over 130 m² of area tested. The following observations can be highlighted:

1. Robust data set of rebound indices is possible to be recorded by the subjective rejection of the suspected outliers by the operator during testing. Application of the extreme studentized deviate test by Peirce's criterion resulted only 3% suspected outliers in the complete data set of 462 rebound index readings recorded at 42 individual test areas for the present tests. It was found that statistical dispersion parameters are the most sensitive to the Peirce's criterion filtering and statistical location parameters are the least sensitive to the Peirce's criterion filtering.
2. From an engineering point of view, normal probability distribution may be suggested only as a rough estimate for the frequency histogram of rebound indices collected at the 42 individual test areas if no separation of data by location is applied. It should be noted, however, that the goodness of fit of normal distribution was found to be inferior to skewed (or even uniform) distributions; best goodness of fit was found for the Fisher-Tippett (Generalized extreme value, GEV) distribution.
3. The hypothesis of normality (tested by Shapiro-Wilk test) can be generally accepted at a very low significance level for the 42 independent test areas analysed separately. Platykurtic behaviour governs the observations. Application of the Peirce's criterion filtering decreases the deviation from normality in skewness, but can not improve excess kurtosis performance.
4. Skewed distributions can be fit with the best goodness of fit for the vast majority of frequency histograms of the local statistical parameters studied.

11. Acknowledgement

Author gratefully acknowledges the support of the Hungarian Scientific Research Fund project "Durability and performance characteristics of concretes with novel type supplementary materials" (OTKA K 109233).

References

[1] ACI (2003) In-Place Methods to Estimate Concrete Strength - ACI 228.1R-03. *American Concrete Institute*, Farmington Hills, Michigan

[2] Bungey J. H., Millard J. H., Grantham, M. G. (2006) Testing of Concrete in Structures. *Taylor and Francis*, New York, 352 p.

[3] Carino N. J. (1994) Nondestructive Testing of Concrete: History and Challenges, ACI SP-44, Concrete Technology – Past, Present and Future, Ed. Mehta, P. K. *American Concrete Institute*, 1994, pp. 623-678.

[4] Malhotra, V. M., Carino, N. J. (2004) Handbook on nondestructive testing of concrete. Second edition, *CRC Press LLC*, 384 p.

[5] Long A. E., Henderson G. D., Montgomery FR (2001) Why assess the properties of near-surface concrete? *Construction and Building Materials* Vol. 15, pp. 65–79. http://dx.doi.org/10.1016/S0950-0618(00)00056-8

[6] Tay D. C. K., Tam C. T. (1996) In situ investigation of the strength of deteriorated concrete. *Construction and Building Materials* Vol. 10, pp. 17–26. http://dx.doi.org/10.1016/0950-0618(95)00057-7

[7] Schmidt E. (1950) Rebound hammer for concrete testing (Der Beton-Prüfhammer). *Schweizerische Bauzeitung*, 15. Juli 1950, 68. Jahrgang, Nr. 28, pp. 378-379. (in German)

[8] Kolek J. (1958) An Appreciation of the Schmidt Rebound Hammer. *Magazine of Concrete Research*, Vol. 10, No. 28, March 1958, pp. 27-36.

[9] Szilágyi K., Borosnyói A., Zsigovics I. (2011) Rebound surface hardness of concrete: Introduction of an empirical constitutive model. *Construction and Building Materials*, Vol. 25, Issue 5, May 2011, pp. 2480-2487. http://dx.doi.org/10.1016/j.conbuildmat.2010.11.070

[10] Breysse D (2012) Nondestructive evaluation of concrete strength: an historical review and a new perspective by combining NDT methods. *Construction and Building Materials* Vol. 33, pp.139–63. http://dx.doi.org/10.1016/j.conbuildmat.2011.12.103

[11] Breysse D., Fernández J. L. M. (2013) Assessing concrete strength with rebound hammer: review of key issues and ideas for more reliable conclusions. *Materials and Structures*, July 2013, online article, http://dx.doi.org/10.1617/s11527-013-0139-9

[12] Pekár G. (2013) Simple basic model for concrete and its application. Part 2 - Factors that influence compressive strength and drying shrinkage. *Építőanyag-JSBCM* Vol. 65, pp. 76–84. http://dx.doi.org/10.14382/epitoanyag-jsbcm.2013.15

[13] Pekár G. (2013) Simple basic model for concrete and its application. Part 3 - Factors affecting consistency, material balance equations and mix design. *Építőanyag-JSBCM* Vol. 65, pp. 118–126. http://dx.doi.org/10.14382/epitoanyag-jsbcm.2013.22

[14] Borosnyói A., Szilágyi K. (2013) Studies on the spatial variability of rebound hammer test results recorded at in-situ testing. *Építőanyag-JSBCM* Vol. 65, pp. 102–106. http://dx.doi.org/10.14382/epitoanyag-jsbcm.2013.19

[15] Szilágyi K., Borosnyói A., Mikó T. (2013) Comparison of the inherent variability in rebound hammer tests performed with different testing instruments. *Építőanyag-JSBCM* Vol. 65, pp. 68–75. http://dx.doi.org/10.14382/epitoanyag-jsbcm.2013.14

[16] Ross S. M. (2003) Peirce's criterion for the elimination of suspect experimental data. *Journal of Engineering Technology* Vol. 2, pp. 1–12. ISSN 0747-9664

[17] Szilágyi K., Borosnyói A., Zsigovics I. (2014) Extensive statistical analysis of the variability of concrete rebound hardness based on a large database of 60 years experience. *Construction and Building Materials* Vol. 53, pp. 333–347. http://dx.doi.org/10.1016/j.conbuildmat.2013.11.113

[18] Dufour J. M., Farhat A., Gardiol L., Khalaf L. (1998) Simulation-based finite sample normality tests in linear regressions. *The Econometrics Journal* Vol. 1, pp. 154–173 http://dx.doi.org/10.1111/1368-423X.11009

[19] Razali N. M., Wah Y. B. (2011) Power comparisons of Shapiro–Wilk, Kolmogorov–Smirnov, Lilliefors and Anderson–Darling tests. *Journal of Statistical Modeling and Analytics* Vol. 2, pp. 21–33. ISSN 2180-3102

[20] Shapiro S. S., Wilk M. B. (1965) An analysis of variance test for normality (complete samples). *Biometrika* Vol. 52, pp. 591–611. http://dx.doi.org/10.1093/biomet/52.3-4.591

[21] Shapiro S. S., Wilk M. B. (1968) Approximations for the Null Distribution of the W Statistic. *Technometrics* Vol. 10, pp. 861–866. http://dx.doi.org/10.1080/00401706.1968.10490638

[22] Griffiths G. A. (1989) A theoretically based Wakeby distribution for annual flood series. *Hydrological Sciences Journal* Vol. 34, No. 3., pp. 231–248. http://dx.doi.org/10.1080/02626668909491332

[23] Öztekin T. (2007) Wakeby distribution for representing annual extreme and partial duration rainfall series. *Meteorological Applications* Vol. 14, No. 4., pp. 381–387. http://dx.doi.org/10.1002/met.37

[24] ASTM (2013) Test method for rebound number of hardened concrete ASTM C 805/C 805M–13. ASTM International http://dx.doi.org/10.1520/C0805_C0805M

Appendix. Formulae

The following local statistical measures were calculated for the inherent variability during the present analyses (in the formulae R_i accounts for the individual rebound index readings and index j denotes the j^{th} test area):

mean value (=arithmetic mean): $$R_{m,j} = \frac{1}{n}\sum_{i=1}^{n} R_i$$

standard deviation: $$s_{R,j} = \left(\frac{1}{n-1}\sum_{i=1}^{n}\left(R_i - R_{m,j}\right)^2\right)^{1/2}$$

coefficient of variation: $$V_{R,j} = \frac{s_{R,j}}{R_{m,j}} \cdot 100$$

range: $$r_{R,j} = R_{i,max} - R_{i,min}$$

relative range: $$\rho_{R,j} = \frac{r_{R,j}}{R_{m,j}} \cdot 100$$

studentized range: $$\theta_{R,j} = \frac{r_{R,j}}{s_{R,j}}$$

extreme studentized deviate: $$\zeta_{i,j} = \frac{\left|R_i - R_{m,j}\right|}{s_{R,j}}$$

skewness: $$\gamma_{1,j} = \frac{n}{(n-1)(n-2)}\sum_{i=1}^{n}\left(\frac{R_i - R_{m,j}}{s_{R,j}}\right)^3$$

excess kurtosis: $$\gamma_{2,j} = \frac{n(n+1)}{(n-1)(n-2)(n-3)}\sum_{i=1}^{n}\left(\frac{R_i - R_{m,j}}{s_{R,j}}\right)^4 - \frac{3(n-1)^2}{(n-2)(n-3)}$$

Ref.:

Borosnyói, Adorján: *Variability case study based on in-situ rebound hardness testing of concrete. Part 1.*
Építőanyag – Journal of Silicate Based and Composite Materials, Vol. 66, No. 3 (2014), 85–91. p.
http://dx.doi.org/10.14382/epitoanyag-jsbcm.2014.16

Esettanulmány betonszerkezet helyszíni keménységméréséről
1. rész. A mérőhelyen belüli változékonyság statisztikai elemzése

A cikk egy vasbeton födém alsó felületének 130 m²-es szakaszán végzett, helyszíni Schmidt-kalapácsos vizsgálatok eredményeinek statisztikai elemzését mutatja be. A mérőhelyen belüli változékonyság statisztikai paramétereinek elemzése és az egyes paraméterek közötti korreláció vizsgálata történik meg. A cikk feltárja, hogy a vizsgálat alá vont statisztikai paraméterek nagy részének eloszlása jelentős ferdeséggel rendelkezik. A cikk bemutatja a Peirce-féle studentizált szélsőérték kritérium alkalmazási lehetőségét a helyi kiugró mérési eredmények kiszűrésére. Az eredmények rávilágítanak arra, hogy a helyszíni Schmidt-kalapácsos vizsgálatok során a mérőhelyeken megfigyelhető visszapattanási értékek eloszlásának normalitása gyenge.
Kulcsszavak: betonszerkezet; roncsolásmentes vizsgálat; keménység; visszapattanási érték; mérőhelyen belüli változékonyság

GUIDELINE FOR AUTHORS

The manuscript must contain the followings: title; author's name, workplace, e-mail address; abstract, keywords; main text; acknowledgement (optional)**; references; figures, photos with notes; tables with notes; short biography** (information on the scientific works of the authors).

The full manuscript should not be more than 6 pages including figures, photos and tables. Settings of the word document are: 3 cm margin up and down, 2,5 cm margin left and right. Paper size: A4. Letter size 10 pt, type: Times New Roman. Lines: simple, justified.

TITLE, AUTHOR

The title of the article should be short and objective.
Under the title the name of the author(s), workplace, e-mail address.
If the text originally was a presentation or poster at a conference, it should be marked.

ABSTRACT, KEYWORDS

The abstract is a short summary of the manuscript, about a half page size. The author should give keywords to the text, which are the most important elements of the article.

MAIN TEXT

Contains: materials and experimental procedure (or something similar), results and discussion (or something similar), conclusions.

REFERENCES

References are marked with numbers, e.g. [6], and a bibliography is made by the reference's order. References should be provided together with the DOI if available.
Examples:
Journals:
[6] Mohamed, K. R. – El-Rashidy, Z. M. – Salama, A. A.: In vitro properties of nano-hydroxyapatite/chitosan biocomposites. *Ceramics International.* 37(8), December 2011, pp. 3265–3271, http://dx.doi.org/10.1016/j.ceramint.2011.05.121
Books:
[6] Mehta, P. K. – Monteiro, P. J. M.: Concrete. Microstructure, properties, and materials. *McGraw-Hill*, 2006, 659 p.

FIGURES, TABLES

All drawings, diagrams and photos are figures. The **text should contain references to all figures and tables**. This shows the place of the figure in the text. Please send all the figures in attached files, and not as a part of the text. **All figures and tables should have a title**.
Authors are asked to submit color figures by submission. Black and white figures are suggested to be avoided, however, acceptable.
The figures should be: tiff, jpg or eps files, 300 dpi at least, photos are 600 dpi at least.

BIOGRAPHY

Max. 500 character size professional biography of the author(s).

CHECKING

The editing board checks the articles and informs the authors about suggested modifications. Since the author is responsible for the content of the article, the author is not liable to accept them.

CONTACT

Please send the manuscript in electronic format to the following e-mail address: femgomze@uni-miskolc.hu and epitoanyag@szte.org.hu or by post: Scientific Society of the Silicate Industry, Budapest, Bécsi út 122–124., H-1034, HUNGARY

We kindly ask the authors to give their e-mail address and phone number on behalf of the quick conciliation.

Építőanyag – *Journal of Silicate Based and Composite Materials*, Quarterly peer-reviewed periodical of the Hungarian Scientific Society of the Silicate Industry, SZTE.
http://epitoanyag.org.hu

The Concrete Network is all about concrete

The Concrete Network's purpose is to educate homeowners, contractors, builders, and designers on popular concrete techniques and applications. With thousands of articles, photographs, and a comprehensive directory of concrete contractors and product suppliers, The Concrete Network offers the most comprehensive online resource for independent, authoritative information about concrete construction:

- decorative concrete
- cleaning, repair and maintenance
- general concrete construction
- home building with concrete
- green building with concrete
- and more

The Concrete Network is independent and not related (or beholden) to any contractor, manufacturer, or supplier and thus has become "the independent voice of concrete".

Philosophy of The Concrete Network:

The Concrete Network strives to be the highest quality online resource of accurate, independent, and balanced editorial content- all about concrete.

Our information sources are concrete contractors and decorative concrete artisans who are on the front line of the business and whose livelihood is concrete construction 2 they know what works and what doesn't.

Other sources of information are proven building industry professionals and subject-matter experts, such as trainers. Their information is rooted in real-world experience designing, producing, or installing concrete.

The Concrete Network is truly ***the independent voice of concrete***. We do not endorse any specific products. We do give appropriate credits to the building project team, concrete contractors, and manufacturers, whether they are a client of The Concrete Network or not.

The Concrete Network also encourages training and supports various professional groups and associations working in the building industry to promote best practices, standards and quality workmanship.


Furniture


Fireplace surrounds


Walkways


Countertops


Sinks

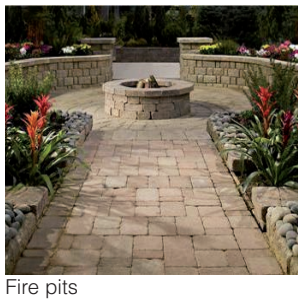
Fire pits

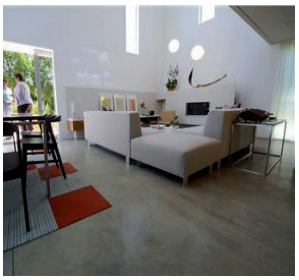
Floors

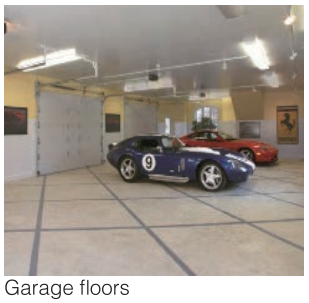
Garage floors


Water features

For more information visit:
www.concretenetwork.com

ConcreteNetwork.com

European Ceramic Society
Ave. Gouverneur Cornez 4, B-7000 Mons, Belgium
ecers@bcrc.be
www.ecers.org

Who We Are

The European Ceramic Society (ECerS) is a non-governmental, nonprofit federation of national ceramic societies each representing the ceramists of a member country.

The ECerS was established in 1987 in order to co-ordinate and promote the study of ceramics and in particular:

- To encourage education, training and research.
- To consult with and bring together individuals and representatives of members, research establishments, academic bodies and institutions of governments and other bodies including the Commission of the European Community.
- To collect, disseminate and exchange information with other organizations
- To promote planning, promotion and organization of conferences and meetings
- To procure planning, printing, publication and circulation of technical papers,

The Council of the ECerS consists of the Presidents of the Member organizations and one more member of each national organization.

The President is elected by the Council for a period of two years. The President is assisted by the Executive Committee and an Advisory Group. Six Working Groups have been established for specific objectives: Education, R&D, Communication, Editorial, Industrial and Art, Design & Tradition .

Every two years the ECerS organizes a general Conference in one of the member countries.

Journal

The Journal of the ECerS publishes the results of original research relating to the structure, properties and processing of ceramic materials. Papers of either an experimental or theoretical character will be welcomed on a fully international basis. Papers may cover any of the branches of ceramic science and technology and may relate to any of the so called categories, structural, functional and traditional ceramics. The central objective will be to sustain a high standard of research quality by means of appropriate reviewing procedures. The Journal is published for the ECerS by Elsevier Science Publishers Ltd.

Awards

The Richard Brook Award:

This award is given to a ceramist belonging to a country outside Europe for outstanding contribution to ceramic science or technology and for enhancing understanding and collaboration within the international ceramic community.

The Stuijts Award:

In memory of Prof. A. Leo Stuijts (1922-1982), who contributed considerably to the development of the science and technology of magneto- and electro-ceramic materials. This award is given to ceramists belonging to a member country of the Society for outstanding contributions to ceramic science, technology and educational activities or production.